THE UNIVERSITY OF TULSA

THE GRADUATE SCHOOL

DEVELOPMENT OF EROSION EQUATIONS

FOR SOLID PARTICLE AND LIQUID DROPLET IMPACT

by
Hadi Arabnejad Khanouki

A dissertation submitted in partial fulfillment of

the requirements for the degree of Doctor of Philosophy

in the Discipline of Mechanical Engineering

The Graduate School

The University of Tulsa

2015

THE UNIVERSITY OF TULSA

THE GRADUATE SCHOOL

DEVELOPMENT OF EROSION EQUATIONS

FOR SOLID PARTICLE AND LIQUID DROPLET IMPACT

by
Hadi Arabnejad Khanouki

A DISSERTATION

APPROVED FOR THE DISCIPLINE OF

MECHANICAL ENGINEERING

By Dissertation Committee

_____, Chair
Siamack Shirazi

_____,Co-Chair
Brenton McLaury

_____
Michael Keller

_____
Kenneth Roberts

_____
Selen Cremaschi

COPYRIGHT STATEMENT

Copyright © 2015 by Hadi Arabnejad Khanouki

ABSTRACT

Hadi Arabnejad Khanouki (Doctor of Philosophy in Mechanical Engineering)

Development of Erosion Equations for Solid Particle and Liquid Droplet Impact

Directed by Drs. Siamack Shirazi and Brenton McLaury

146 pp., Chapter 8: Recommendations

(475 words)

In the oil and gas industry, there are many particles that may cause erosion. These particles are of various sizes, shapes and hardnesses. Liquid droplets are also another source of concern, especially in high velocity gas streams. Currently, solid particle erosion prediction models such as Computational Fluid Dynamics (CFD) based erosion models and Sand Production Pipe Saver (SPPS) program developed by the Erosion/Corrosion Research Center (E/CRC) rely on empirical erosion equations. These equations do not account for the erodent particle and target material properties accurately.

In this work, different materials have been tested in direct impingement configuration, and particle velocity has been measured with particle image velocimetry (PIV). A new semi-mechanistic erosion equation has been developed by assuming that erosion caused by particle impacts is due to two mechanisms, cutting and deformation. Empirical constants have been obtained for the tested materials, and the model has been verified with experimental data for different particles. In contrast to the angle functions that are currently being used for all particles and impact velocities, angle dependence in the new model changes with the particle shape and velocity and showed fair agreement

with experimental data.

The effect of particle hardness on the erosion of stainless steel has been studied with fine particles at low impacting velocities with two experimental apparatuses, submerged configuration with slurry mix and mist flow test with solid particles entrained in the droplets. The testing particles are iron powder, calcite, barite, apatite, hematite, magnetite, silica flour, alumina and silicon carbide. Droplet size and velocity for air/water tests have been measured by PIV for air/water tests, and particle impact velocity for both tests is estimated from CFD simulation with particle tracking scheme. It was observed that erosion ratio increases with increasing particle hardness when the target material is harder than the particle and does not change considerably after the point where the particle is hard enough to keep its integrity during impact.

A new erosion equation has been developed to calculate erosion resulting from liquid impacts for pipeline materials based on experimental data that was collected previously at E/CRC and American Society for Testing and Materials (ASTM) G73 guideline. Based on the new erosion model, a procedure has been developed to predict erosional velocity due to liquid droplet impact (with or without small particles entrained) utilizing the entrainment fraction and droplet size calculated from two-phase flow correlations and the impact velocity of the droplets within a pipe elbow or a tee that is estimated using stagnation length model. The erosional velocities computed using this model are compared with the erosional velocities computed using API RP 14E. It is shown that the trend of the erosional velocity calculated by the API guideline is extremely conservative as compared to the new model predictions for erosion due to liquid impacts and does not correlate with erosion due to small entrained particles.

ACKNOWLEDGEMENTS

TABLE OF CONTENTS

LIST OF FIGURES

LIST OF TABLES

CHAPTER 1

INTRODUCTION

1.1 Overview

In the oil and gas industry, erosion/corrosion may be a major problem in production and transportation facilities including but not limited to pipelines, valves, chokes, production manifolds and process headers. Erosion is the physical removal of material by solid particles or liquid droplets, and corrosion is another form of material degradation that occurs through chemical reaction. So, production and transportation facilities are designed so that the flow velocity is below the erosional velocity, presumably a flow velocity at which it is safe to operate but beyond that erosion damage may occur. This threshold velocity depends on many factors such as fluid properties, operating condition, entrained particles and geometry type and size, and its prediction is important from both economical and safety aspects. Furthermore, erosion/corrosion of materials due to the impingement of solid particles or liquid droplets is also important in power plant and aerospace industries.

Depending on the oil and gas production condition, solid particles may be present in the flow. The particles that may cause erosion are of various sizes, shapes and hardnesses, and the effects of these parameters are properly understood. In clean service or corrosive flow, liquid droplets are another source of concern especially in high velocity gas streams. Moreover, the liquid droplets that are entrained in the produced gas from the reservoir may be corrosive or contain very small particles that are hardly

separable by physical means.

1.2 Research Goals

The main goals of this work are to predict erosion failure in production and transportation facilities in oil and gas industry and their components due to the impingement of different particles and liquid droplets. Being able to predict erosion resulting from various particles and droplets, would lead to lower costs of erosion inspection and maintenance and also, the risk of component failure would be reduced by improving geometry and utilizing more appropriate materials.

1.3 Research Approach

A comprehensive approach to erosion modeling consists of flow modeling, particle tracking and erosion equations. So, the first step is to model the flow either by computational fluid dynamics (CFD) or use approximations for flow near the wall. Then, particles are tracked as they move toward the wall, and the impact velocity and angle is estimated. The final step is to apply the erosion equation for the estimated impact velocity and angle and calculate the erosion ratio which is the ratio of target mass loss to the mass of erodent particle. The erosion ratio equation plays a major role in this calculation and depends on many parameters including but not limited to erodent particle characteristics, target material properties and speed and angle of impact. Thus, in the present work, erosion models are investigated including erosion resulting from sand, other particles and liquid droplets.

The approach of this work is first to search the literature for erosion equations for solid particles. Then, conduct erosion tests in a direct impingement configuration for different materials and develop a mechanistic model for erosion prediction which accounts for the speed and angle of impact, particle characteristics and target material properties. Particle hardness will be also correlated to erosion based on the experimental data obtained in a separate experimental facility. After completion and verification, this model will be implemented in SPPS (Sand Production Pipe Saver program developed at E/CRC) as well as commercial CFD software such as ANSYS Fluent to predict erosion caused by different particles in the oil and gas industry.

For calculation of erosion due to liquid droplets, the literature is surveyed for erosion models and experimental data. Experimental data that are obtained at E/CRC are used to develop a new erosion ratio equation for liquid droplets. Multiphase flow equations and models are implemented to determine impact conditions of droplets and particles to be substituted in the erosion equations to predict erosion ratio, and a calculation methodology is presented to calculate threshold erosional velocity or penetration rate due to liquid droplet impingement with or without small particles at very low solid concentrations.

CHAPTER 2

BACKGROUND AND LITERATURE REVIEW

2.1 Introduction

In order to prevent severe erosive/corrosive damage to different components in oil and gas production and transportation facilities, extensive theoretical and empirical studies have been carried out by the researchers from around the world. The emerging guidelines and erosion/corrosion prediction tools may be classified into categories based on the mechanism of degradation: erosion, corrosion or erosion/corrosion. Solid particles that may be present in the liquid or gas produced from the reservoir can cause erosion damage, and the transporting fluid may cause corrosion. The synergistic effect of these two mechanisms is called erosion/corrosion. Liquid droplets can also cause erosion if they have enough energy to degrade the target material mechanically. The main focus of this work is on erosion caused by solid particle and liquid droplet impacts.

2.2 Solid Particle Impact Erosion

2.2.1 Background

The approach to predict erosion damage for a desired geometry and flow condition has three major steps: flow modeling, particle tracking, and erosion calculation. The flow solution and particle impact speed and angle may be approximated from

simplified models or obtained more accurately from Computational Fluid Dynamics (CFD) simulations. Generally in a CFD simulation of particle erosion, an Eulerian-Lagrangian model is employed. In other words, the fluid flow solution is obtained from Navier-Stokes equations (Eulerian approach), and then particle traces are determined using a Lagrangian particle tracking scheme. The CFD and particle tracking are done to determine particle impact speed and angle that affect erosion of materials. The next step is to substitute the impact speed and angle in an appropriate erosion equation and find the erosion. The erosion equation, which is a function of target material specifications, particle properties and particle impact condition, is very important in this calculation procedure.

The parameters that erosion depends on may be classified into three categories: impact condition (impact speed and angle), erodent particle characteristics and target material properties. The most important particle parameters are hardness, shape and size. The effects of particle size and shape are now currently expressed as explicit sharpness and size functions, but experimental data revealed that there are some inter-relations between some of these parameters, and the angle function may depend on impact velocity and shape of the particle. Properties of the eroding surface that are important in erosion are ductility, hardness and density. Erosional behavior of ductile materials is different than brittle materials. Figure 2.1 shows typical erosional behavior of ductile and brittle materials as a function of particle impact angle. For ductile materials, erosion increases with the impact angle up to a maximum point (approximately between 15-30 degrees) and then coasts down to a certain value at 90 degree impact, but for brittle materials, erosion increases with impact angle and the maximum erosion is obtained at normal

impact.
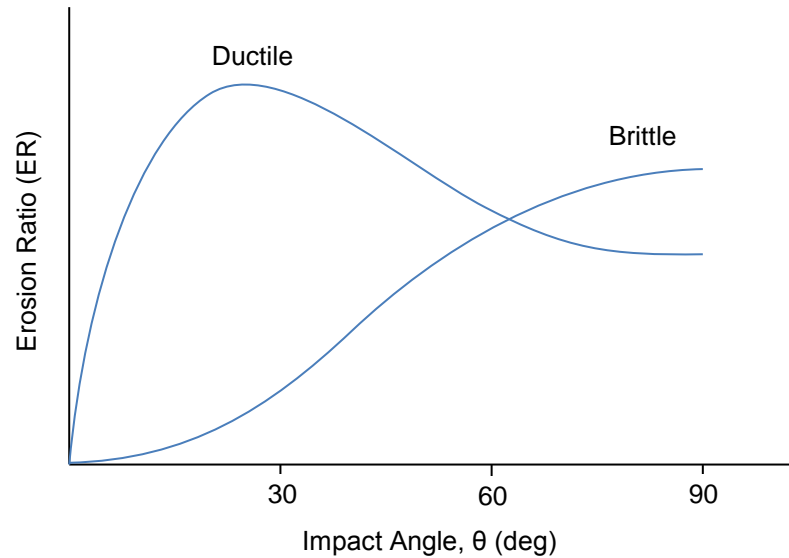
Figure 2.1 Typical erosion behavior of ductile and brittle materials

versus impact angle

Material hardness is another important parameter, and density of the material is used when we need to convert removed mass to removed volume. So, the erosion ratio (ER) which is the ratio of target mass loss to the mass of impinged particle is

$$ER = \frac{\text{Mass of Removed Material}}{\text{Mass of Erodent}} = f(V, \theta, Hv, \rho, D, F_s) \tag{2.1}$$

here V and θ are speed and angle of impact, Hv and ρ are target material hardness and density, D and F_s are particle size and sharpness factor, respectively.

2.2.2 Literature Review

Solid particle erosion has been studied extensively in the literature for aerospace industry applications and oil and gas production and slurry transport systems. In early studies, most of the attention was paid to the material-related aspects of erosion

6

(Humphrey 1990). The researchers (Finnie 1960, Sheldon et al. 1966, Goodwin et al. 1969, Head et al. 1970, Sheldon 1970, Grant et al. 1973, Williams et al. 1974 and Sundararajan et al. 1983) proposed equations generally in the form of

$$ER = K \, V^n \, f(\theta) \tag{2.2}$$

where K is the erosion constant, V is the particle velocity and $f(\theta)$ is the impact angle function. The erosion constant, K, velocity exponent, n, and the angle function have been determined from experimental data or theoretical analysis of material behavior under particle impacts.

The particle impact velocity and angle in the erosion equation are unknown and their value depends on the environment surrounding the particle. Laitone (1979), Chein et al. (1988), Clark (1992) and Nguyen et al. (1999) proposed analytical quantification methods to estimate the particle-wall collision information in particle-laden flows.

Assisted by the advancement of computational resources, Dosanjh et al. (1985) and Schuh et al. (1989) accounted for the influence of turbulence in predicting motion of the particle and used CFD simulations in their studies, but comprehensive CFD simulations along with particle tracking have been done in more recent studies by Edwards (2000), Niu et al. (2000, 2001), Chen (2004) and Zhang (2006).

Specific to oil and gas industry, there are some calculation guidelines and methodologies proposed in the literature. American Petroleum Institute Recommended Practice 14E (API RP 14E) proposed a correlation for erosional velocity, V_e (in ft/s) for gas-liquid mixtures as follows,

$$V_e = \frac{c}{\sqrt{\rho_m}} \tag{2.3}$$

where c is an empirical constant and ρ_m is the gas/liquid mixture density in lb/ft^3. The

basis for development API correlation is not clear, but it should not be applied to sand erosion conditions as it does not account for many parameters in erosion calculation such as particle and wall properties and geometry specifications. Salama and Venkatesh (1983) and Salama (2000) proposed alternate correlations to API RP 14E in which they assumed that the velocity of particles is similar to fluid velocity. Bourgoyne (1989) developed another empirical correlation and Svedeman and Arnold (1993) calculated threshold velocities from Bourgoyne's correlation. These empirical correlations highly depend on the experimental conditions and most of them do not account for the particle size, shape and fluid physical properties.

Shirazi, et al. (1995a, 1995b) and McLaury, et al. (1995) presented a comprehensive mechanistic model to predict erosion in elbows and tees in single and multiphase flows using a stagnation length concept. The stagnation length was determined from experiments or CFD simulations. The proposed method predicts a representative particle impact velocity to be used in the erosion equation.

Currently, erosion prediction models including CFD-based erosion models or a simplified version such as the Sand Production Pipe Saver (SPPS) program (Shirazi et al. 2000) which is developed at the Erosion/Corrosion Research Center (E/CRC) rely on empirical erosion equations. These equations do not account for the particle size and shape accurately, and they have been developed for each erodent particle and target material separately. Zhang et al. (2007) implemented an empirical erosion equation which had been obtained from gas testing into a CFD code to predict the erosion ratio occurring on a flat specimen and bend for air and water flows. Also, Wong et al. (2013) utilized an empirical erosion equation originally proposed by Chen et al. (2004) to predict

the erosion ratio in a pipe annular cavity via CFD simulation. In addition, many other works are conducted to predict the erosion rate in various geometries by coupling the CFD simulation and an erosion equation (Njobuenwu et al. 2012, Pereira et al. 2014, Mansouri et al. 2014).

Mechanistic erosion equations that are available in the literature are developed based on the calculation of the displaced volume by a single particle or energy dissipation during particle impact. Finnie et al. (1978) developed an erosion equation for ductile materials based on the material cutting volume by a single particle. Bitter (1963a, 1963b) used an energy balance and proposed that erosion is proportional to the part of the particle kinetic energy that is absorbed by the target material and caused plastic deformation. Sheldon et al. (1972) developed an equation based on single particle indentations for spherical and angular particles for normal impacts and at low velocity. Two erosion models developed by Hutching (1981, 1993) are based on the deformed volume by spherical particles at normal incidence and cutting action of a particle at oblique impacts. Sundararajan (1991) proposed an erosion model by assuming that deformation beyond the critical strain and energy dissipation of the particle, caused by friction force between the particle and the eroding material, are responsible for the erosion at normal and oblique impacts. Bingley et al. (2005) implemented the equations of Hutching and Sundararajan for nine heat treated steels, and Harsha et al. (2008) used Hutching's equations for some ferrous and non-ferrous metals. In their work, the constants in the erosion equations were calculated from experimental data, and a relation was found between the empirical constants and the mechanical properties of the eroding material including hardness. However, the effect of impact angle was not properly

investigated. A relation was found by Levin et al. (1999) between the mechanical properties of some ductile alloys and the volumetric erosion obtained from experiments, but the relation was developed for normal impact only. In a recent study, a mechanistic erosion equation has been developed by Huang et al. (2008) using approximations for removed material by a spherical particle. They calculated the volume removed by the vertical and tangential components of particle velocity separately. Generally in these equations, many assumptions have been made to find a closed form solution of the problem and find the relation between the properties of target materials and erosion. They compared the results mostly to experimental data for pure materials such as iron, aluminum, and copper, not alloy metals that are being used in industry.

Feng et al. (1999) empirically studied the dependency of erosion of ductile and brittle materials on impact velocity and particle size for different erodent particles but did not report an equation to be used for erosion prediction. Oka et al. (2005a, 2005b) developed empirical correlations of erosion for many particles and materials, but his equation only has been validated at impact velocities more than 50 m/s which are rarely applicable to the oil and gas industry. Experiments in a slurry pot tester for two ductile materials and three erodent particles by Desale et al. (2006) implied that the material removal mechanism is a function of particle shape and density, but no equation was proposed.

There are also some studies in the literature on numerical modeling of erosion using finite element (FE) methods (Molinari et al. 2002, ElTobgy et al. 2005, Wang et al. 2008) or micro-scale dynamic models (MSDM) (Chen et al. 2003, Li et al. 20011), but generally good agreement between the experimental data and numerical modeling results

10

were not obtained. Currently, these studies are more useful to understand the behavior of material during impact and characterize the mechanisms of erosion rather than calculating erosion for a given condition.

2.3 Liquid Droplet Impact Erosion

2.3.1 Background

In the API correlation (Equation 2.2), c = 100 for continuous service and c = 125 for intermittent service for solid-free fluids and when corrosion is not anticipated, but the constant could rise to c = 250 for other conditions. Some authors believe that the basis for API RP 14E may be due to liquid impact erosion (Salama and Venkatesh 1983). However, there is no experimental or theoretical evidence supporting this idea. The erosional velocity calculated from this equation seems to be very conservative as compared to the experimental data from literature (Thiruvengadam et al. 1969, Baker et al. 1966).

Salama and Venkatesh (1983) proposed an equation for sand erosion and concluded that erosional velocity due to liquid droplet impingement in clean service is as high as values corresponding to c = 300 in the API RP 14E correlation, and this velocity limitation is not allowed because of severe pressure drop in the pipe. Svedeman (1995) concluded that flow velocity does not require being limited in sand-free and corrosion-free service. Castle, et al. (1991) reported operational velocity up to three times the calculated value from the API formula (3×API) for various materials. Some authors developed analytical or empirical formulae to predict erosion due to liquid impact

(Nokleberg et al. 1995, Springer 1976). These formulae are applicable to a certain range of flow conditions especially for extremely high velocity gas streams which are rarely achievable in the petroleum industry.

Some experimental studies related to liquid droplet erosion have been conducted in other fields such as in aerospace engineering where rain erosion is a similar phenomenon. Also in power plant industries, turbine blades and steam pipelines are exposed to liquid droplet impingement erosion. The impingement velocity for these applications is much higher than the operational velocities in the oil and gas industry not only because of erosion risk but also due to pressure drop and other production limitations. So, the threshold velocities of these studies could not be applied to the oil and gas industry without further investigation. However, their methodology could be implemented to develop models and calculation procedures to predict erosion failures of production and transportation facilities in the oil and gas industry due to liquid impacts.

CHAPTER 3

**EXPERIMENTAL SETUP AND MEASUREMENTS
FOR SOLID PARTICLE EROSION**

3.1 Introduction

Experimental setup and measurement are of great importance in the empirical

studies. The data provided by the experiments will be used later to derive models, and a

proper experimental and measuring system is required to study the effect of different

parameters. As mentioned in the previous chapter, erosion is influenced by many factors

including particle impact speed and angle, particle shape and hardness and target material

properties. Levy (1995) reviewed some of the experimental apparatuses used in solid

particle erosion studies. The slinger system which uses centrifugal force to accelerate the

particles in a vacuum chamber, and the particle velocity is controlled by the rotational

speed. The nozzle tester is the most common erosion test equipment and uses pressurized

gas to accelerate the particles in the nozzle tube. In this system, it is essential to

determine the particle velocity especially at high gas velocities where the slippage

between the particle and the carrier fluid is considerable. Before the advancement of

electronic velocity measurement systems, two co-rotating disks were placed in front of

the nozzle. The particles pass through the hole on the first disk and cause erosion on the

second disk periodically. The particle velocity was determined based on the rotational

speed of the disks and erosion mark on the second disk.

In this work, three different nozzle erosion test equipment are used to study the

effect of different parameters on erosion, and particle velocity is measured by laser velocity measurement system, namely particle image velocimeter (PIV).

3.2 Experimental Setup

3.2.1 Direct Impingement Tests in Gas

In order to develop erosion equations, direct impingement testing has been performed on different materials to provide the experimental database. Figure 3.1 shows a schematic of the test apparatus, and the configuration of the nozzle and specimen holder is shown in Figure 3.2. Pressurized air that is supplied to the nozzle takes in particles from the sand feeder at a constant particle flow rate. These particles are accelerated by the gas flow to impact the target material and cause material loss of the coupon. These tests have been performed at different impact velocities (9, 18 and 28 m/s) and angles (15, 30, 45, 60, 75 and 90 degrees) to determine the speed and angle dependence of the erosion equation for each material. A sample of the erosion testing experimental results is shown in Figure 3.3. At each impact angle, the mass loss of the specimen is measured at three intervals after blasting with a specific amount of sand which is 300 grams in most of the cases considered here. More particles were required to get measurable mass losses at low impact velocities. A linear trendline is fit through these three points which are cumulative mass loss versus sand mass throughput. The slope of this line is the steady-state erosion ratio which is dimensionless and plotted for all impact angles on the right of Figure 3.3. In the right hand side of Figure 3.3, vertical axis is the erosion ratio and corresponding impact angle is shown on the horizontal axis. Erosion equation is the

14

dashed line that passes through these points. Most of the erosion tests have been repeated

at the same condition to confirm the repeatability of the experiments.
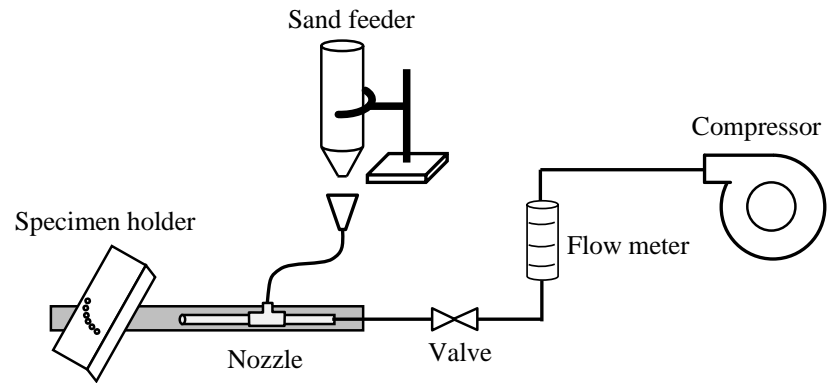
Figure 3.1 Schematics of experimental test facility

Figure 3.2 Configuration of nozzle and specimen holder
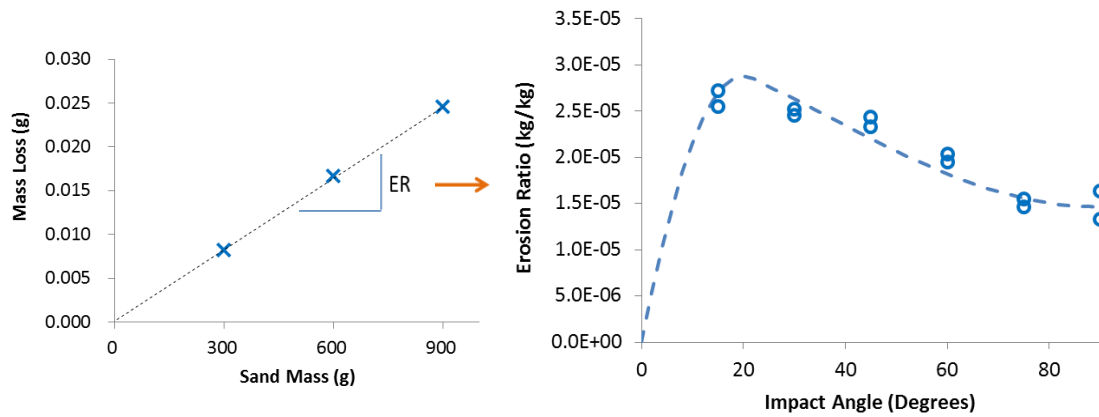
Figure 3.3. Calculation of erosion ratio from experimental data

3.2.2 Liquid Submerged Tests

In order to characterize erosive behavior of various small particles entrained in liquids, a submerged apparatus was designed and constructed. In this apparatus, particles are suspended in the slurry tank by means of a stirrer. As sketched in Figure 3.4, the slurry mixture is deducted from the bottom of the tank and pumped through a nozzle to impact the specimen. It should be noted that the particle impact velocities are not the same as the liquid velocities as significant drag is expected as particles interact with the flowing submerged jet impacting a target. This is similar to what happens in the slurry flow through an elbow.

Water with density of 1000 kg/m^3 and viscosity of 1 cP was used in these tests, and the liquid velocity of the submerged jet was kept constant at 16.8 m/s. The orientation angle between the nozzle and specimen (which is SS-316) was 90° and the distance from nozzle to specimen was 0.5 inches (12.7 mm). Particle concentration in the slurry mix flowing through the nozzle was assumed to be consistent with the particle

concentration in the slurry tank as particles are so small (2 – 40 μm) that they will be easily transported by the liquid. A stirrer was also used to keep homogeneity of the slurry mixture in the tank. Figure 3.5 shows a picture of the submerged experimental apparatus.
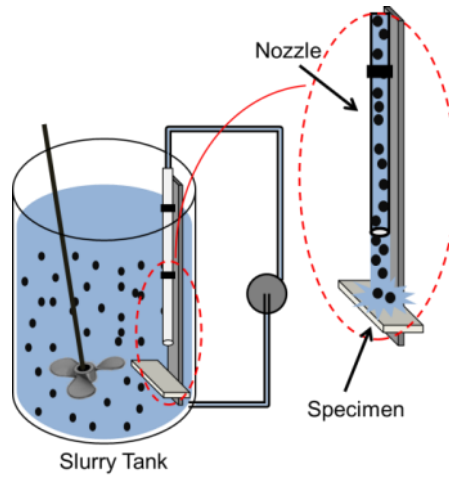
Figure 3.4 Schematics of submerged experimental apparatus
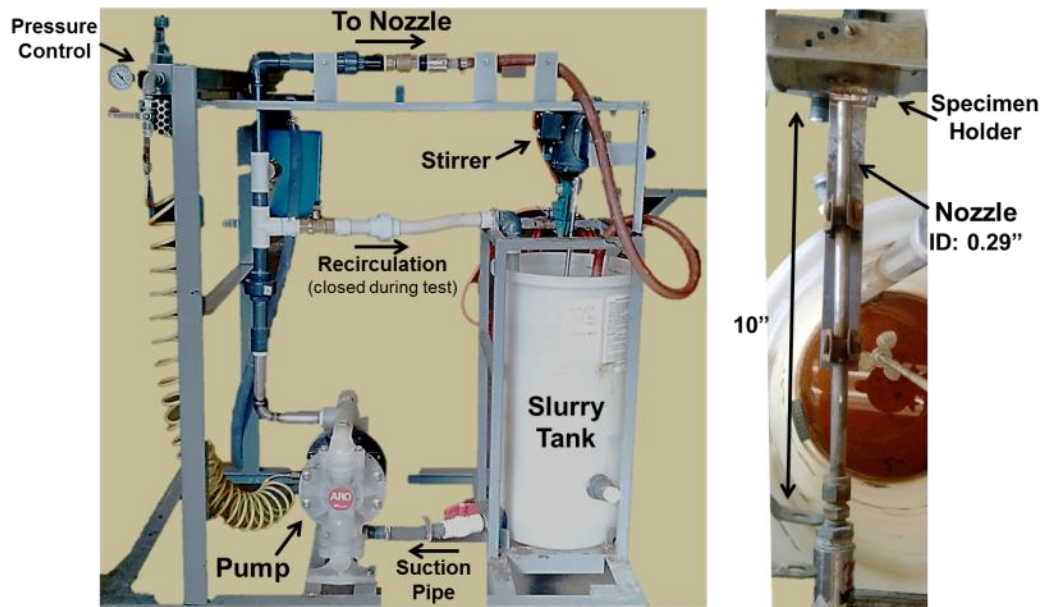
Figure 3.5 Submerged experimental apparatus

3.2.3 Air/Water Mist Flow Tests

The air/water mist flow testing apparatus is designed and constructed to replicate the condition of gas-liquid mixture flow in pipe with low liquid loading where droplets are entrained in the gas core. In these tests, particles are entrained in the liquid droplet, and it is a form of gas testing with liquid droplets containing particles. This experimental apparatus consists of a slurry mixer container, stirrer and nozzle (Figure 3.6). A picture of the experimental setup is shown in Figure 3.7. In addition to what described before, the recirculation pump circulates the slurry to prevent sedimentation of the particles in the mist catching tube. Pressurized air is supplied to the nozzle to deduct the slurry mixture from the container which leads to formation of droplets containing particles. The gas velocity in the mist flow tests were 45.7 m/s. Table 3.1 shows flow parameters and testing conditions of these loops.
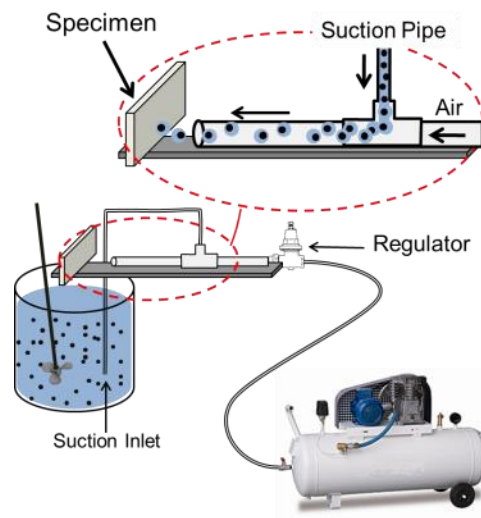
Figure 3.6 Schematics of air/water mist experimental apparatus
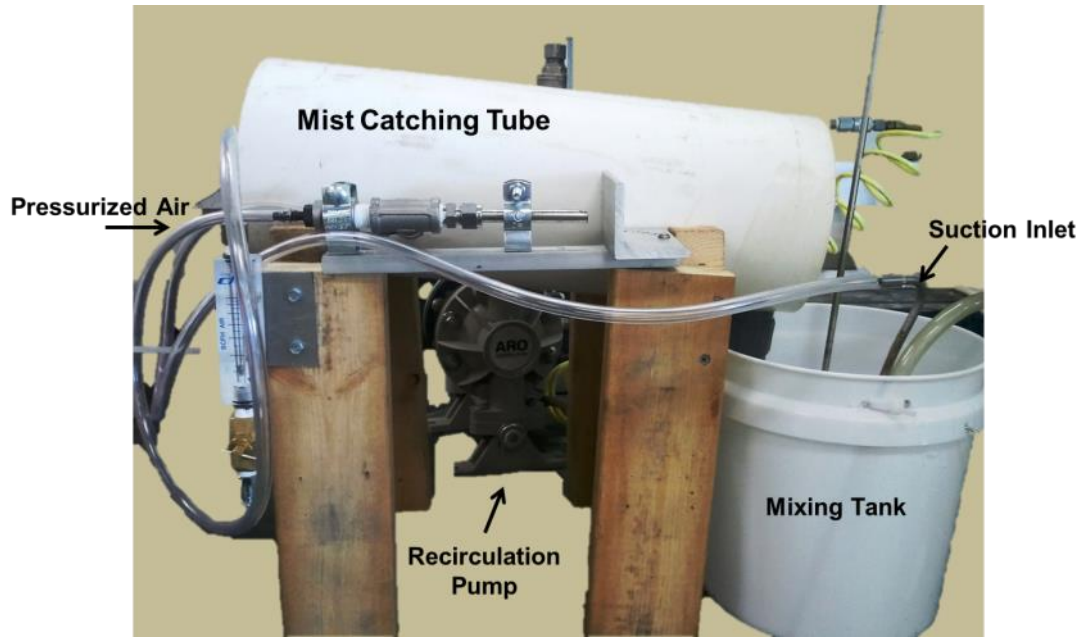
Figure 3.7 Air/water mist flow experimental apparatus

Table 3.1 Summary of testing conditions in two experimental apparatuses

Parameter	submerged	air/water mist
Jet velocity (m/s)	16.8 (liquid)	45.7 (gas)
Particle concentration (kg/kg)	1%	1%
Liquid flow rate (L/s)	0.715	0.013

3.3 Velocity Measurements

3.3.1 Gas Velocity Measurement

In this work, the gas velocity has been measured by means of a Pitot tube and manometer. The Pitot tube consists of a tube with a hole at the tip of the tube exposed directly to the fluid flow to measure the stagnation pressure and another tube on the side which measures the static pressure. The sensed stagnation pressure cannot itself be used to determine the fluid flow velocity. However, the manometer measures the difference between the pressures of these tubes which is dynamic pressure.

$$\text{stagnation pressure} = \text{static pressure} + \text{dynamic pressure} \qquad (3.1)$$

or

$$p_t = p_s + \frac{1}{2}\rho u^2 \qquad (3.2)$$

where p_t is the total or stagnation pressure, p_s is the static pressure, ρ is the fluid density and u is the fluid velocity. Solving for the fluid velocity yields the following equation.

$$u = \sqrt{\frac{2\,(p_t - p_s)}{\rho}} \qquad (3.3)$$

3.3.2 Particle Velocimetry Measurement

Particle impact velocity is an important parameter in the erosion test, and it needs to be measured accurately. Two of the most accurate methods of measuring particle velocity are laser Doppler velocimetry (LDV) and particle image velocimetry (PIV). The LDV, also called laser Doppler anemometry (LDA), is the technique of measuring the

velocity of a moving object from the Doppler shift of the light that it scatters. This technique can be used to measure the velocity of fluid, particles or bubbles. In the case of fluid velocity measurement, seeding particles/bubbles are required and it is assumed that they are moving at the same velocity with the fluid. This non-invasive method is used extensively in the literature for the measurement of turbulent flows, flows around solid objects and in other environments (Johnson 1998), but there are some limitations in measuring the velocity near the wall or when the particle is not a good light reflector.

In this work, the particle velocity is measured using PIV at different gas velocities at the exit of the nozzle to correlate the particle velocity to the gas velocity. This correlation is used to estimate the particle impact velocity in the erosion experiments. The PIV system (TSI Inc.) utilizes a double-pulsed Nd:YAG laser, CCD camera, synchronizer and processor. Figure 3.8 shows a schematic of the PIV system, and Figures 3.9 and 3.10 show the whole velocity measurement system and details of the location of measurement box and the camera, respectively. The light sheet is provided by a double-pulsed laser to illuminate the particles, and the camera is synchronized with the laser pulses. The camera captures two consecutive images of the field. The images are then transferred to the processor to correlate between the two images and track particle movement and finally produce the measured flow/particle velocity field.

Samples of tracked particles and measured particle velocity distribution (for 150 μm sand) at different gas velocities are shown in Figures 3.11 to 3.22. The circle is size proportional to the particle size and the arrow shows the direction of movement and its size and color shows velocity magnitude.

The wide particle velocity distribution may be due to the particle size distribution

21

or turbulent flow fluctuations. Figure 3.23 shows the particle size distribution detected from PIV captured images. The calibration curve shows the average particle velocity versus gas velocity (Figure 3.24). In direct impingement tests, there is always slippage between the entrained particles and gas. So, gas velocity is measured by the Pitot tube and the corresponding particle velocity is extracted from the calibration curve.
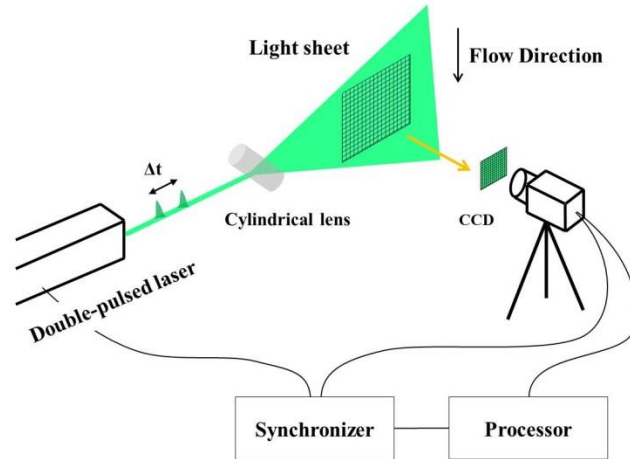
Figure 3.8 Schematics of particle image velocimeter
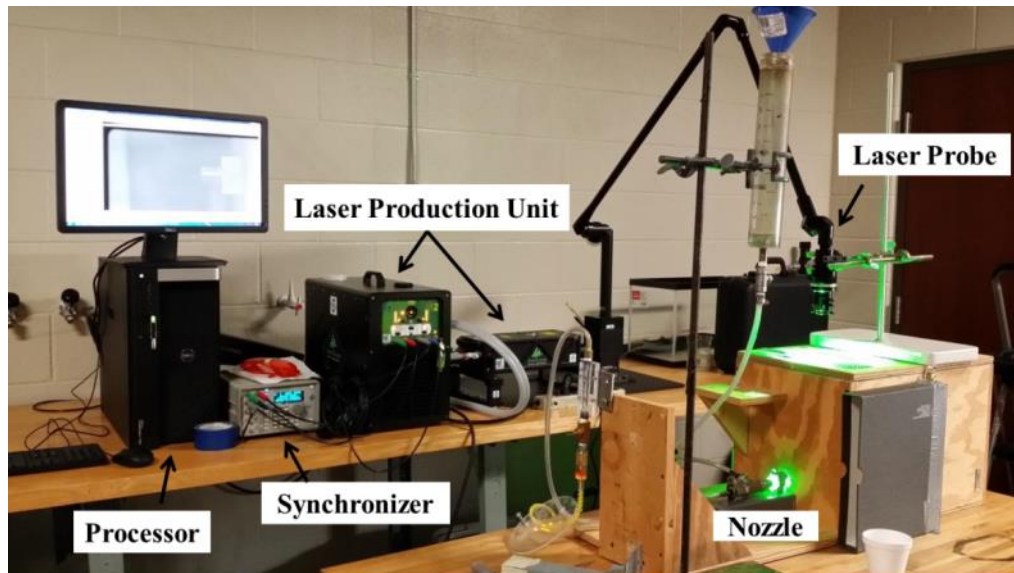
Figure 3.9 Particle velocity measurement setup
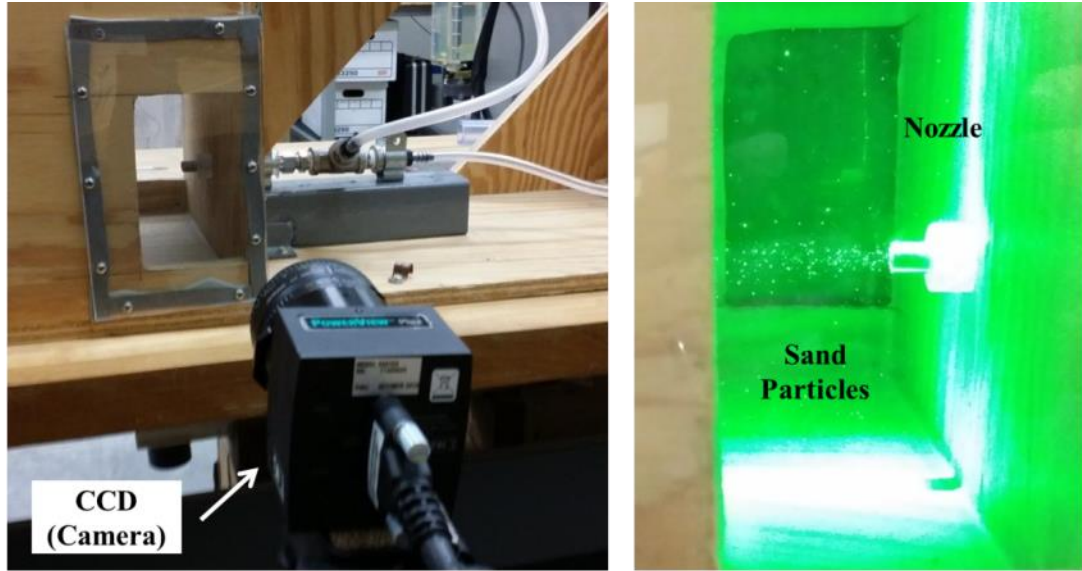
Figure 3.10 Details of the position of camera and velocity measurement box
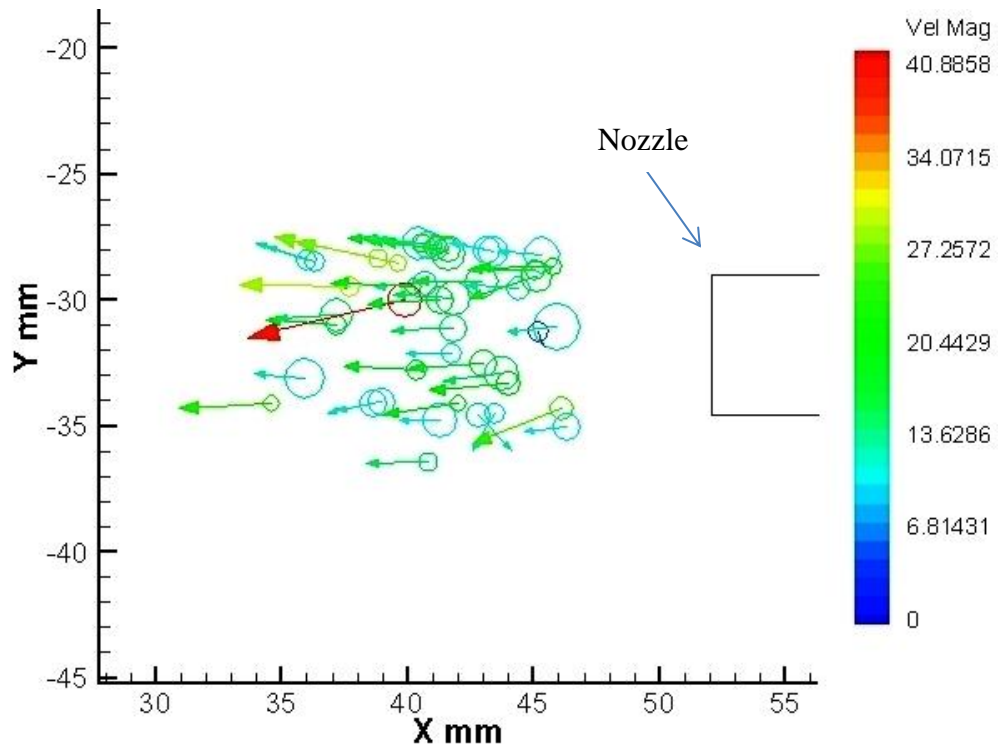
Figure 3.11 Tracked particle sample (for 150 μm sand)

at gas velocity of 46 m/s (5 inches H₂O)
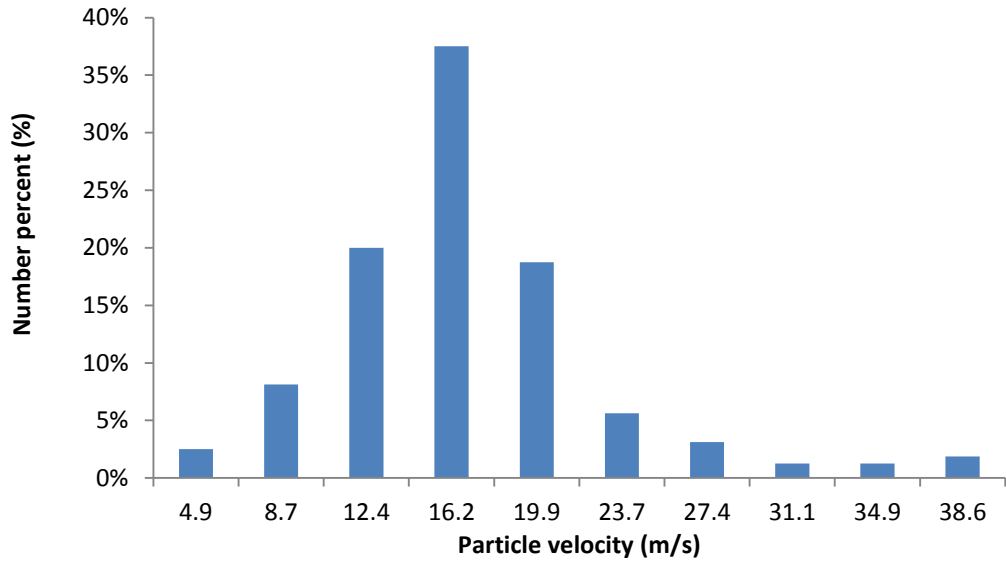
Figure 3.12 Particle velocity distribution (for 150 μm sand)

at gas velocity of 46 m/s (5 inches H₂O)
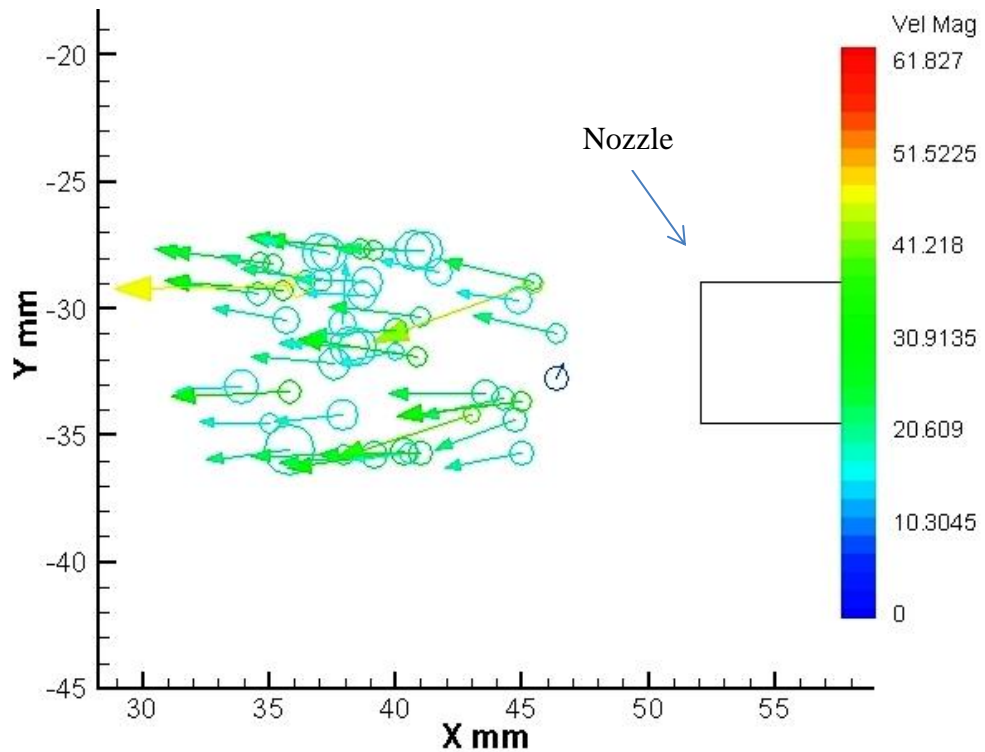
Figure 3.13 Tracked particle sample (for 150 μm sand)

at gas velocity of 65 m/s (10 inches H₂O)
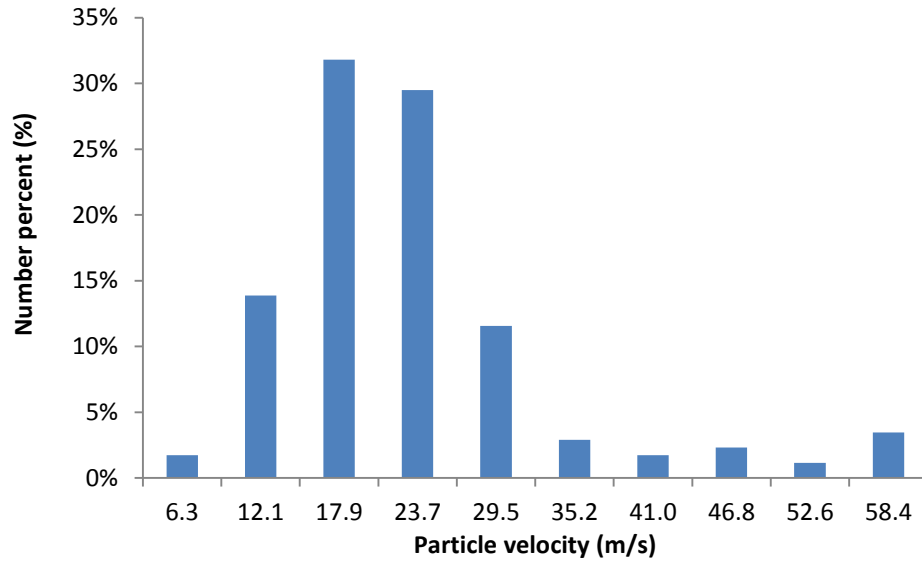
Figure 3.14 Particle velocity distribution (for 150 μm sand)

at gas velocity of 65 m/s (10 inches H$_2$O)
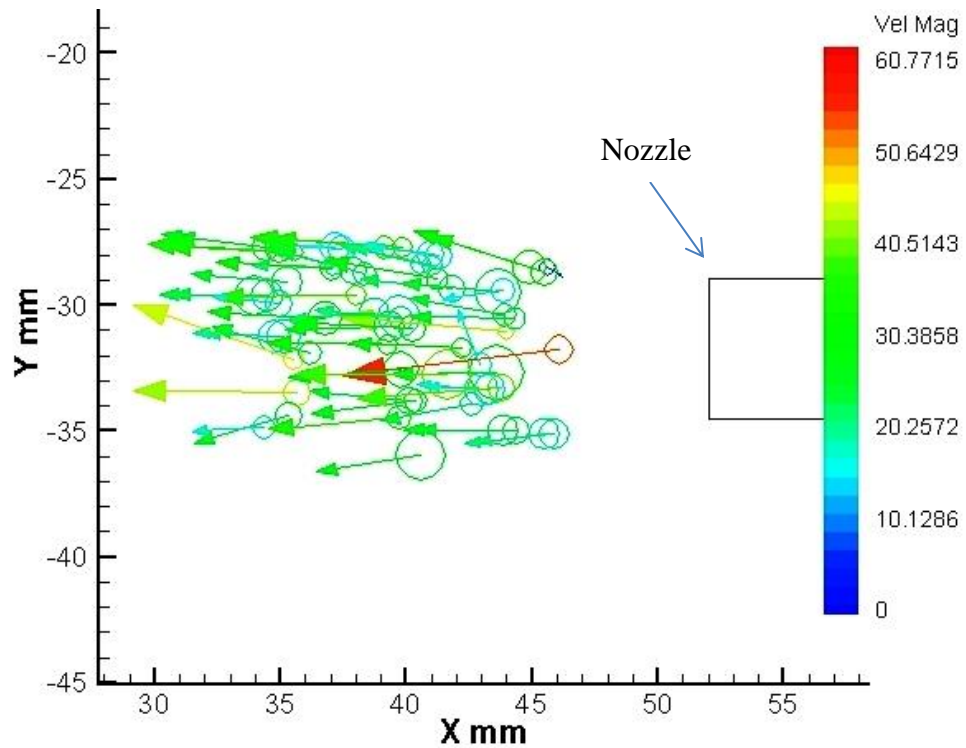
Figure 3.15 Tracked particle sample (for 150 μm sand)

at gas velocity of 80 m/s (15 inches H$_2$O)
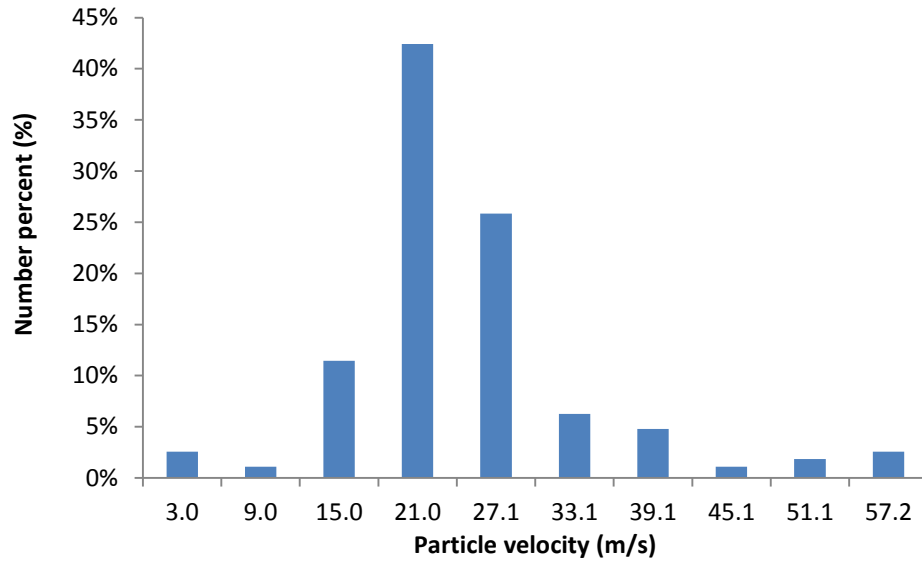
Figure 3.16 Particle velocity distribution (for 150 μm sand)

at gas velocity of 80 m/s (15 inches H$_2$O)
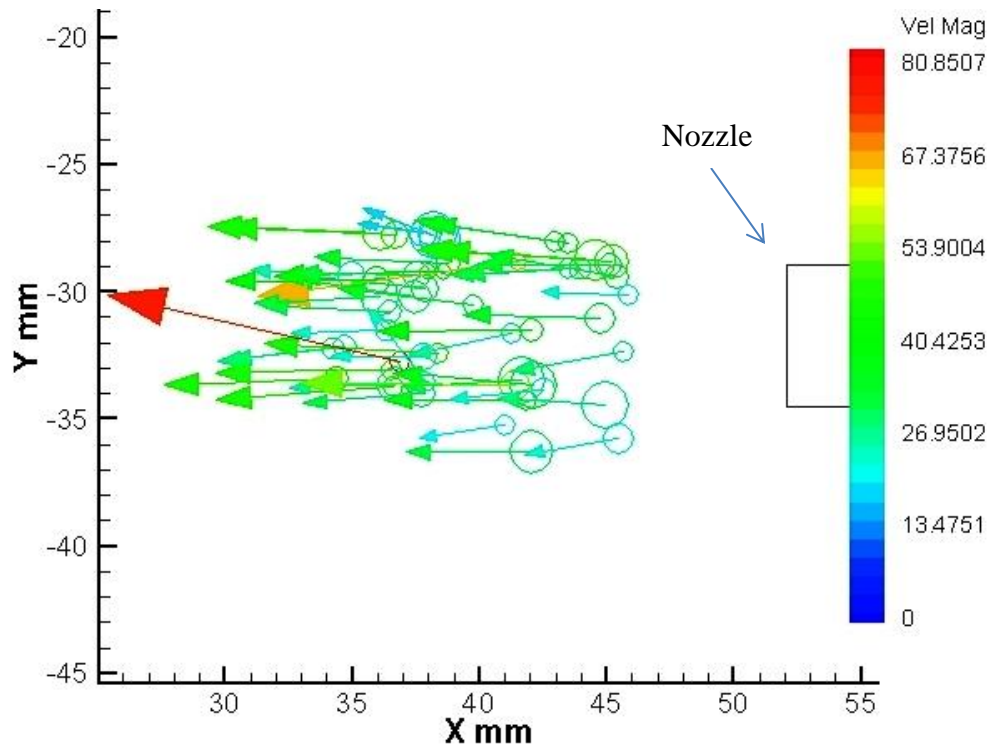
Figure 3.17 Tracked particle sample (for 150 μm sand)

at gas velocity of 92 m/s (20 inches H$_2$O)
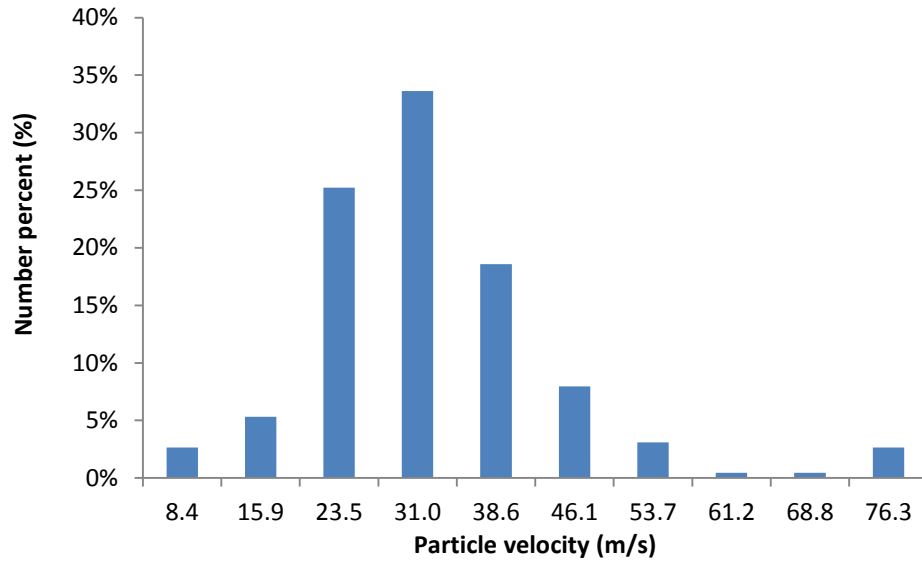
Figure 3.18 Particle velocity distribution (for 150 μm sand)

at gas velocity of 92 m/s (20 inches H₂O)
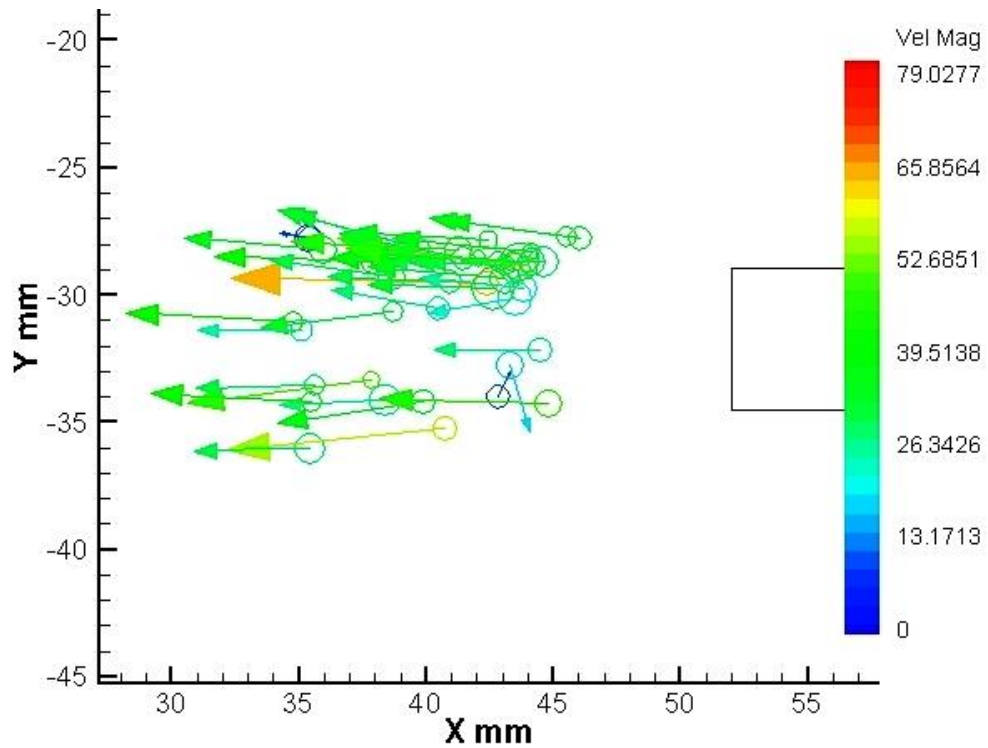
Figure 3.19 Tracked particle sample (for 150 μm sand)

at gas velocity of 103 m/s (25 inches H₂O)
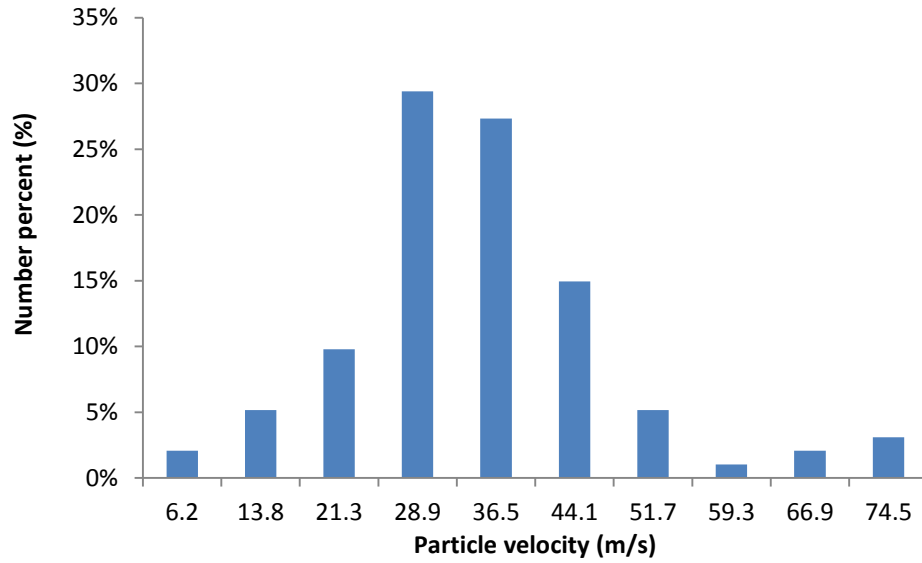
Figure 3.20 Particle velocity distribution (for 150 μm sand)

at gas velocity of 103 m/s (25 inches H₂O)
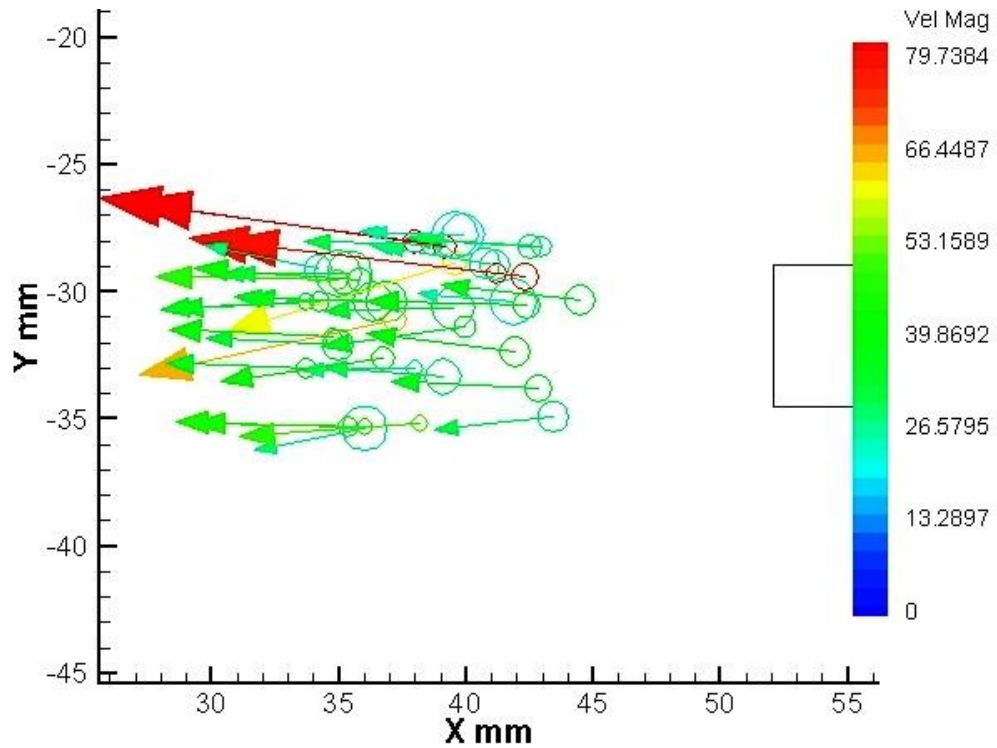
Figure 3.21 Tracked particle sample (for 150 μm sand)

at gas velocity of 113 m/s (30 inches H₂O)
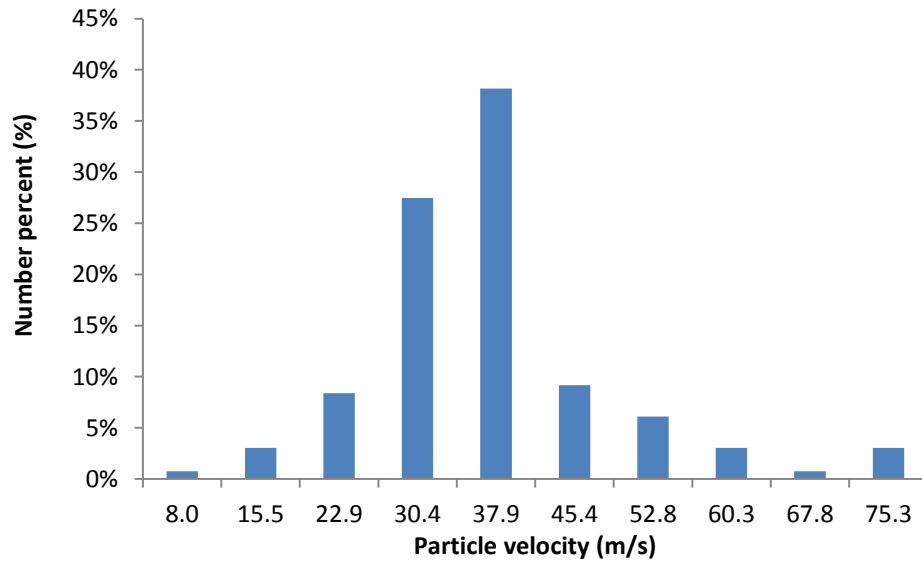
Figure 3.22 Particle velocity distribution (for 150 μm sand)

at gas velocity of 113 m/s (30 inches H$_2$O)
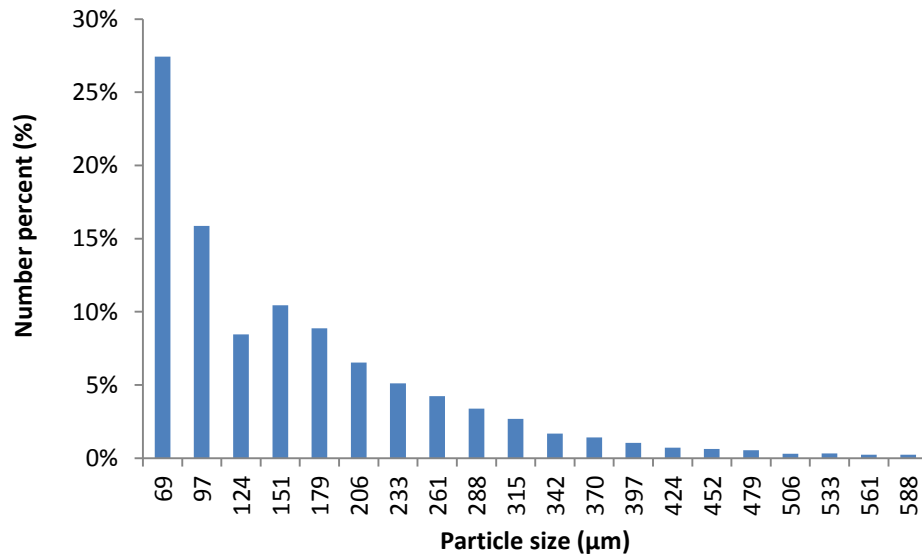
Figure 3.23 Particle size distribution for 150 μm sand
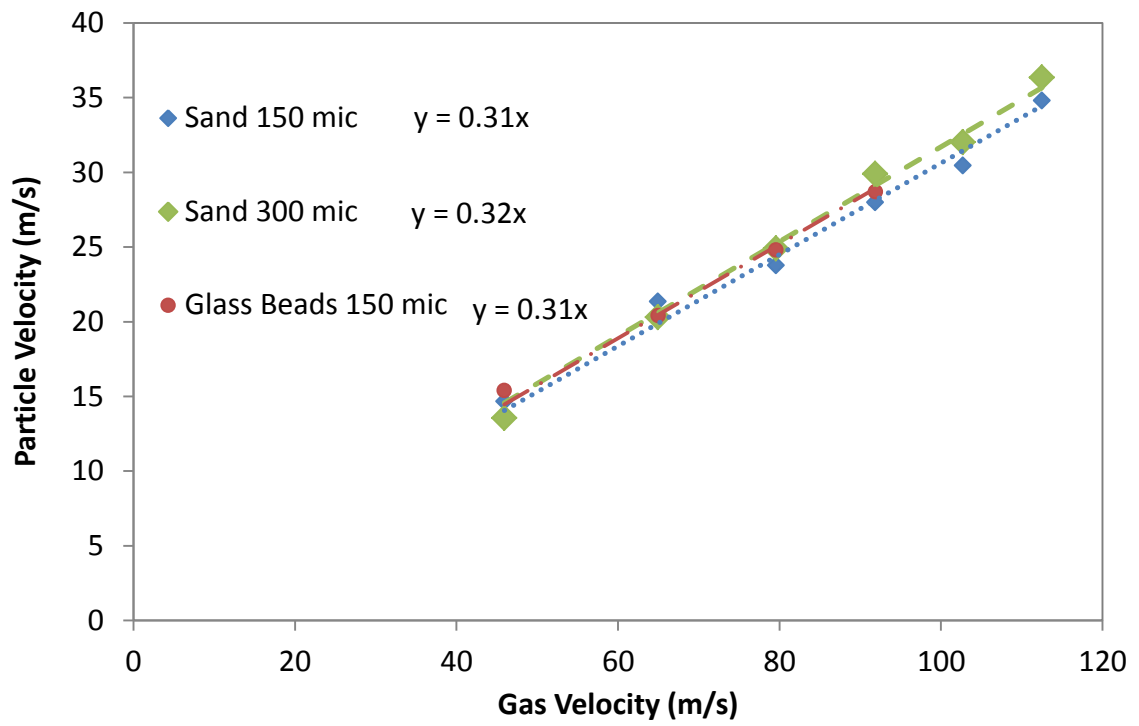
Figure 3.24 Velocity calibration curve for 150μm, 300μm sand and 150μm glass beads

CHAPTER 4

SAND PARTICLE EROSION MODELING

4.1 Introduction

There are lots of studies in the literature conducted on erosion to develop an erosion equation theoretically or empirically. The application of empirical correlations is limited to the materials used in the experiments with specific particles and impact conditions, and theoretical formulations may not be in agreement with experimental data as they have been developed with many simplifying assumptions. The approach in this study is to combine the mechanistic and empirical methods to come up with an erosion equation that can capture the erosion mechanisms while providing agreement with experimental data.

4.2 Experimental Materials

4.2.1 Erodent Particles

In this work, 150 μm semi-rounded sand is used as the main erodent particle, but the effect of particle size and shape is studied with other particles including 300 μm sharp sand and 150 μm glass beads. Figure 4.1 shows SEM micrographs of these particles.

| 150 µm semi-rounded sand | 300 µm sharp sand | 150 µm glass beads |
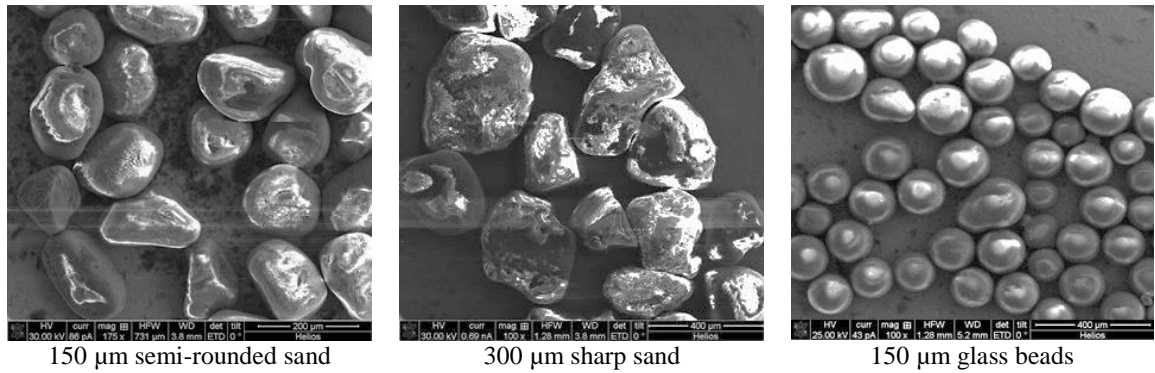
Figure 4.1 SEM micrographs of three erodent particles

4.2.2 Erosion testing materials

Seven target materials were selected for testing including two carbon steels (1018 and 4130), stainless steel 2205, 13 chrome duplex, Inconel 625 and aluminum alloy 6061. Some of these materials are very common in many industries including oil and gas, and their mechanical properties are distributed over a wide range to demonstrate the capability of the erosion equation. Table 4.1 shows the properties of these materials. The hardness of these materials is reported as the annealing Vickers hardness (for some materials it is converted from Brinell hardness) because it will be shown that work or thermal hardening processes have negligible effect on the erosion characteristics.

Table 4.1 Target materials properties

Material	Density (kg/m^3)	Hardness (VHN)
Carbon steel 1018	7870	131
Carbon steel 4130	7850	162
Stainless steel 316	8000	224
Stainless steel 2205	7820	305
13 chrome duplex	7720	268
Inconel 625	8440	252
Aluminum alloy 6061	2700	31

4.3 Mechanistic Modeling

Meng et al. (1995) divided wear into three categories: mechanical, chemical and thermal action. Chemical reaction of the material is classified as corrosion, and removal of the material due to melting occurs at relatively high impact velocities which are out the scope of this context. The mechanical removal of the material may be due to two mechanisms: cutting and deformation (Bitter 1963a, 1963b). When a particle impacts a surface at grazing angles, shearing tension is applied to the material at the contact area, and plastic deformation is caused when kinetic energy of the particle is sufficiently high. This process is repeated for subsequent particle impacts until a piece of material is removed from the surface. At normal impacts, the repeated collisions of many particles cause plastic deformation on the surface if they exceed the elastic limit and form platelets on the surface that may lead to material failure. The erosion scar and SEM micrographs of eroded areas of the stainless steel 316 samples with 150 μm sand particles with impact angles of 30° and 90° are shown in Figure 4.2. The mechanism of erosion varies from

scouring erosion at grazing impact angles where long craters are formed to platelet formation erosion at normal or near normal impact angles. So, the erosive damage by solid particles is caused by two mechanisms namely cutting and deformation. Cutting wear is the process of displacing a piece of material by a particle which will be removed totally or partially by subsequent impacts. Deformation wear is the removal of the material by repeated impact of the particle in the normal direction which results in material plastic deformation, hardening, sub-surface cracking and finally a piece of material will break off. The total wear is the summation of the two terms, cutting plus deformation:

$$ER = ER_C + ER_D \qquad (4.1)$$

The new model will consider both of the erosion mechanisms for ductile materials based on these experimental observations. The volumetric loss of the material due to a particle impact can be estimated from the volume of the material that is swept by a single rigid particle as it cuts into a ductile surface. The forces that resist the motion of the particle are shown in Figure 4.3. The equations of motion of the particle in horizontal and vertical directions originally developed by Finnie et al. (1978) are as follows,
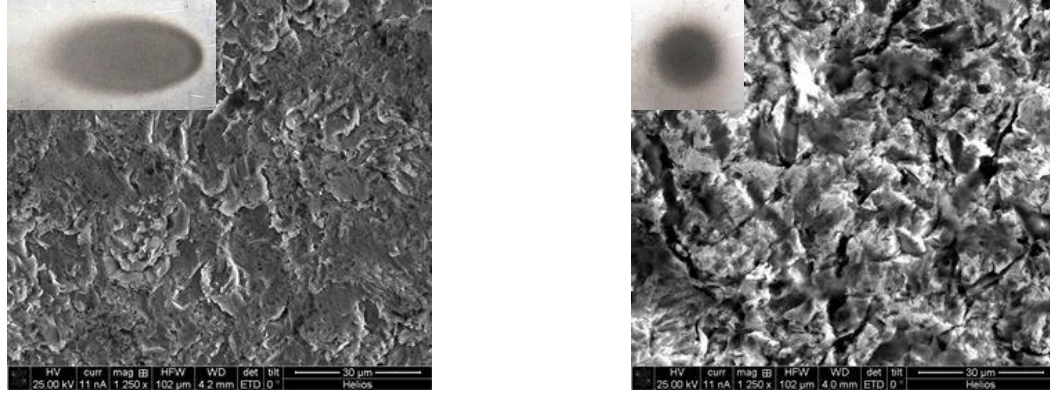
(a) **(b)**

Figure 4.2 Erosion scar and SEM micrographs of SS-316 surface eroded with 150 μm sand at two impact angles: a) 30° and b) 90°

$$K = \frac{A_y}{A_x}$$

$$F_x = P.A_x = P.\frac{n\,R\,y}{K}$$

$$F_y = P.A_y = P.(n\,R\,y)$$
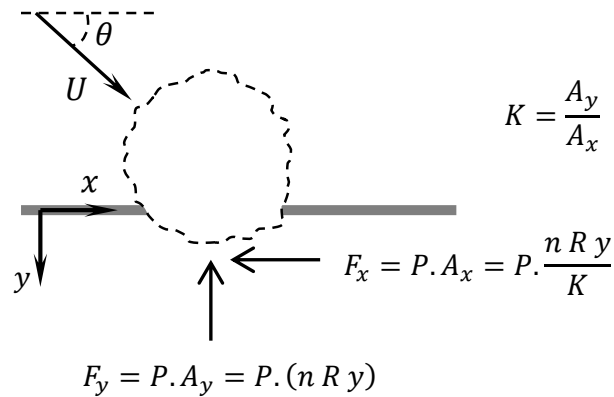
Figure 4.3 Force balance of the particle cutting into the surface

$$m\frac{d^2y}{dt^2} + P\,n\,R\,y = 0 \qquad (4.2)$$

$$m\frac{d^2x}{dt^2} + \frac{P\,n\,R\,y}{K} = 0 \qquad (4.3)$$

in which m is mass of the particle, P is the flow pressure for annealed material which is assumed to be the Vickers hardness of the material, n is the ratio of contact area to the

35

removed area and R is the particle size so that (according to the Hertz contact stress (Andrews 1930))

$$A_y = n.R.y \tag{4.4}$$

It is assumed that contact area in the x-direction is a fraction of contact area in the y-direction as a particle is arbitrary in shape and K depends on shape of the particle and material deformation behavior. In contrast to the constant value that is assigned by Finnie et al. (1978), the value of K will be determined from experimental data for each material. Integration of Eqs. (4.2) and (4.3) and using initial velocity and location of the particle yields,

$$y = \frac{U \sin(\theta)}{\beta} \sin(\beta t) \tag{4.5}$$

$$x = tU \cos(\theta) - \frac{U \sin(\theta)[t\beta - \sin(\beta t)]}{K\beta} \tag{4.6}$$

where

$$\beta = \sqrt{\frac{P\, n\, R}{m}} \tag{4.7}$$

The swept volume is

$$Vol_C = \int A_x.dx = \begin{cases} \dfrac{m\, U^2 \sin(\theta)[2K \cos(\theta) - \sin(\theta)]}{2K^2 P} & for \;\; \theta \le tan^{-1}K \\[4mm] \dfrac{m\, U^2 \cos(\theta)^2}{2P} & for \;\; \theta \ge tan^{-1}K \end{cases} \tag{4.8}$$

If the impact angle is greater than $tan^{-1}K$, the particle will have a velocity component in the x-direction when it leaves the surface and the first equation applies. Otherwise, the x-component of velocity will be zero earlier and the second equation is obtained.

Bitter (1963a) proposed the following equation for deformation erosion,

$$Vol_D = \frac{1}{2} \frac{m \ (U \sin \theta - U_{tsh})^2}{\varepsilon}$$

(4.9)

in which U is the particle initial velocity, U_{tsh} is the threshold velocity below which the deformation erosion is negligible and ε is the deformation wear factor.

The final form of erosion equation with incorporated empirical factors is

$$ER \left[\frac{kg}{kg} \right] = F_s . \rho \frac{C.Vol_C + Vol_D}{m}$$

(4.10)

where F_s is the sharpness factor of the particle, ρ is the material density to convert volumetric loss to mass loss and C is the cutting erosion coefficient that is multiplied by the calculated displaced volume above as every impact is not as ideal as what is assumed here and multiple particle impacts are required to remove a piece of material. Experimental data implied that

$$Vol_C \propto U^{2.41}$$

(4.11)

This may be due to the efficiency of cutting during impact or the effect of velocity on the material resistant forces, and the velocity exponent in cutting erosion need to be updated according to the experimental data.

Many studies in the literature (Tilly 1973, Misra et al. 1981, Bahadur et al. 1990, Liebhard et al. 1991) showed that the effect of particle size on erosion is not considerable for particles larger than 100 μm. This is observed in the derivation of the cutting erosion equation (Eq. 4.8) which is not a function of particle size, although the particle size, R, is considered in the equations of motion (Eqs. 4.2, 4.3). But in the deformation erosion equation (Eq. 4.10) which is based on the kinetic energy of the particle, the value of threshold velocity needs to be a function of particle size. The ratio of the kinetic energy

of a particle with average size of R_2 to that of the reference particle with average size of R_1 with the same velocity is

$$\frac{KE_2}{KE_1} = \frac{m_2}{m_1} = \left(\frac{R_2}{R_1}\right)^3 \tag{4.12}$$

So, the ratio of the threshold velocity that the particle with size of R_2 may cause deformation erosion to the corresponding value for the reference particle (R_1) is

$$\frac{(U_{tsh})_2}{(U_{tsh})_1} = \sqrt{\frac{KE_1}{KE_2}} = \sqrt{\left(\frac{R_1}{R_2}\right)^3} \tag{4.13}$$

Particle shape has an influence on two things: first, the dependency of erosion on the impact angle and second, on particle erosion effectiveness. Rickerby and Macmillan (1980) derived an equation for the volume of the crater caused by a spherical particle, but their equation needs to be solved numerically. The experimental study by Hutchings (1977) on the deformation caused by square plates did not result in an equation. Explanation of erosion mechanisms of material removal by an angular particle is presented by Papini et al. (2006) and Dhar et al. (2005). According to Figure 4.3 and Eqs. (4.2, 4.3), K is the ratio of the contact area in the y-direction to the contact area in the x-direction. Simple geometrical relations for a sharp particle represented by a square impacting the surface by one of its vertices and a rounded particle represented by a circle imply that

$$\frac{K_{sphere}}{K_{square}} \approx 2.5 \tag{4.14}$$

So, the value of K (which is 0.4 for most of the materials eroded with sand) needs to be multiplied by the factor obtained above for round particles, and this increase in the value of K will change the angle dependency in Eq. (4.8). Particle sharpness changes the

erosion effectiveness through stress concentration and changes the contribution of ploughing and microcutting contributions in erosion (Bahadur et al. 1990). Liebhard et al. (1991) determined that angular particles can cause four times more erosion than spherical particles. So, the sharpness factor (F_s) introduced above (Eq. 4.10) varies between 0.25 for fully rounded particles up to 1 for fully sharp particles.

4.4 Experimental Validation

The target materials introduced earlier have been tested at different impact velocities and angles with 150 μm sand (for which the sharpness factor is 0.5) to find the empirical constants in the erosion equation. The empirical constants are provided in Figures 4.4 and 4.6. The cutting erosion constant, C, is observed to be a function of material annealing hardness for these materials, and it follows a trend for these metals. This factor correlates with the square root of the target material hardness. So, the cutting erosion will be proportional to the inverse square root of Vickers hardness. A similar trend has been observed in another study in the literature. Finnie (1967) conducted erosion experiments on some pure materials as well as some alloys with silicon carbide at 20 degrees and impact velocity of 250 ft/s (76 m/s). The results are shown in Figure 4.5. The specimens in annealed form are represented by open circle markers, work hardened represented by filled circle markers and square markers are data points of thermally hardened materials. Vertical axis is the erosion resistance which is defined as one over volumetric erosion in g/mm^3, and horizontal axis is the Vickers hardness of the target material. It is observed that erosion resistance correlates mainly with annealed hardness of the specimen, and work and thermal hardening processes have negligible effect. For

some pure materials, the erosion resistance is proportional to the annealing Vickers hardness, and for some others including iron and three alloy steels 1213, 1045 and tool steel, it is proportional to the square root of annealing Vickers hardness.

For deformation erosion and its empirical constant, finding the correlation is more difficult. In Figure 4.6, the threshold velocity on the left axis and deformation wear factor on the right axis are plotted versus target material hardness. Open markers represents threshold velocity and filled markers are deformation wear factors for aluminum, two carbon steels and four stainless steels. But an approximate correlation may be found for each group of materials between the empirical constants and material hardness, and we can estimate erosion behavior of other steels with these correlations. The threshold velocity is decreasing with the material hardness for all of the samples. The deformation wear factor increased with material hardness for aluminum and stainless steel but showed dissimilar behavior for carbon steels.
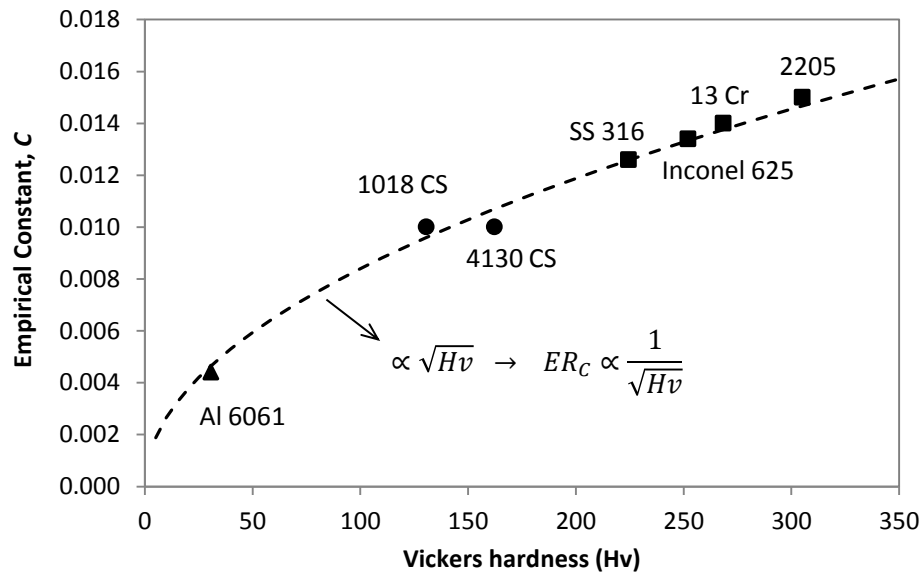
Figure 4.4 Cutting erosion empirical constants for tested materials
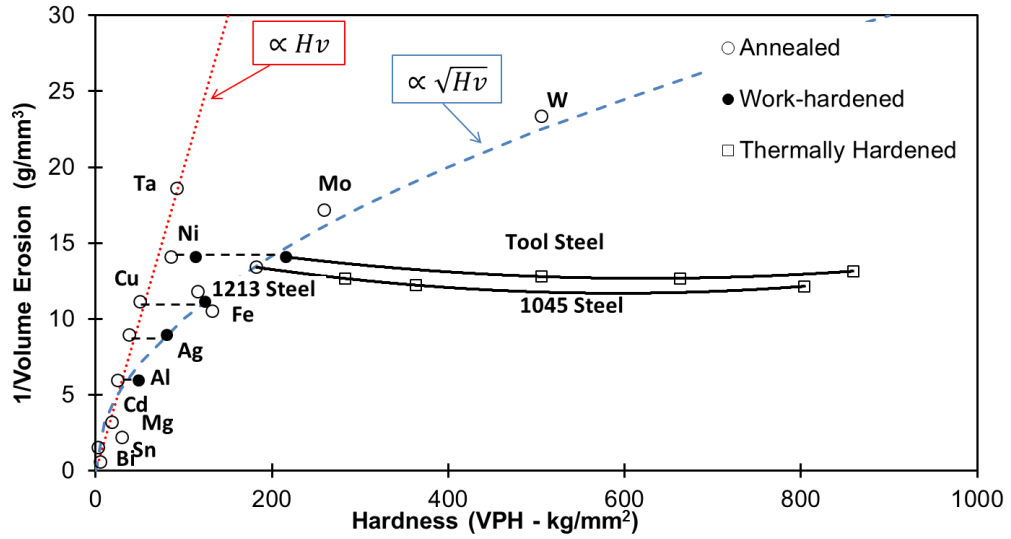
Figure 4.5 Erosion resistance versus material hardness
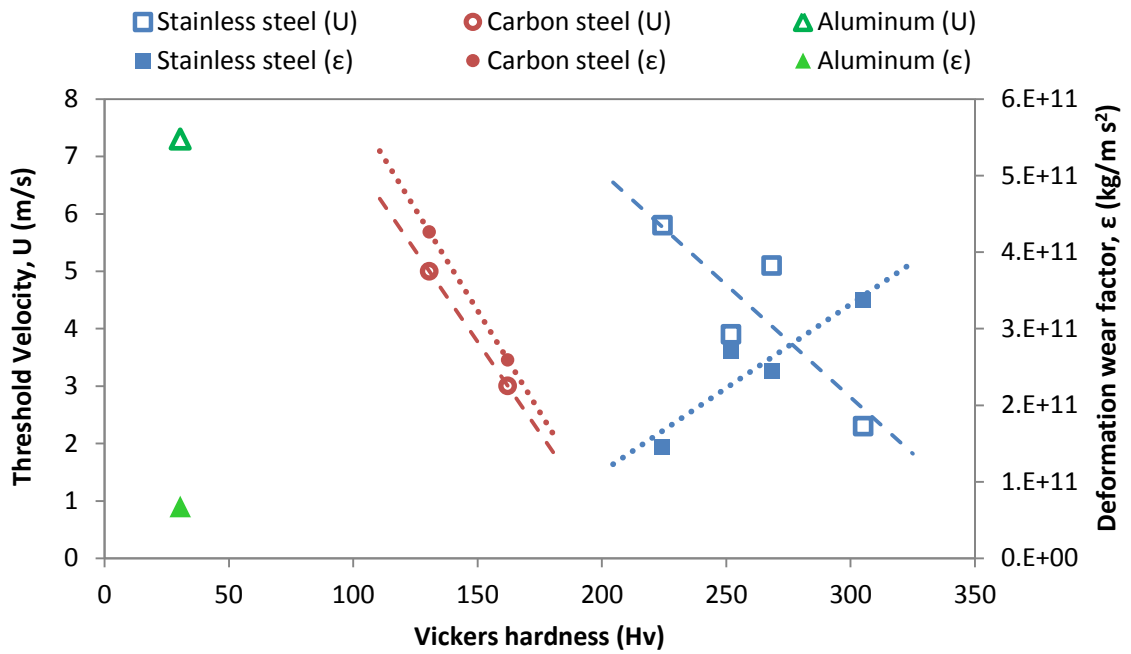
Figure 4.6 Deformation erosion empirical constants for tested materials

Figures 4.7 shows a sample of prediction by the erosion equation for satinless steel 316 and contribution of cutting and deformation in the total erosive wear.
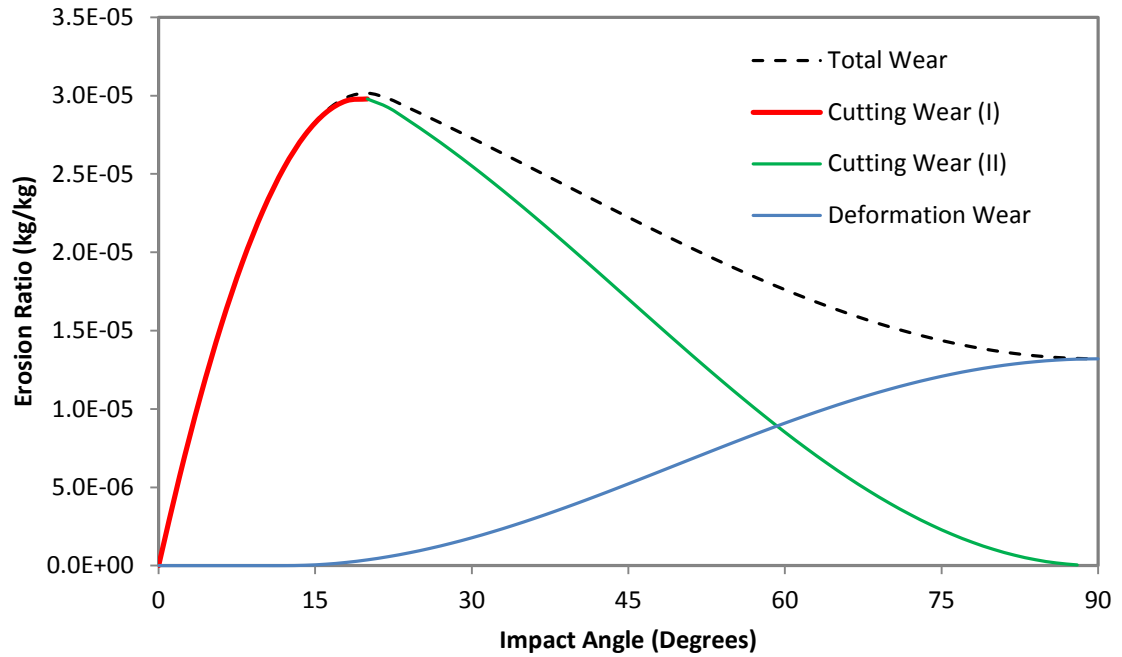
Figure 4.7 Contribution of cutting and deformation wear in the total wear

Figures 4.8 to 4.10 show experimental data for carbon steel 1018, stainless steel 2205 and aluminum alloy 6061 and corresponding values from the erosion equation. Fair agreement is observed between the model predictions and experimental values.
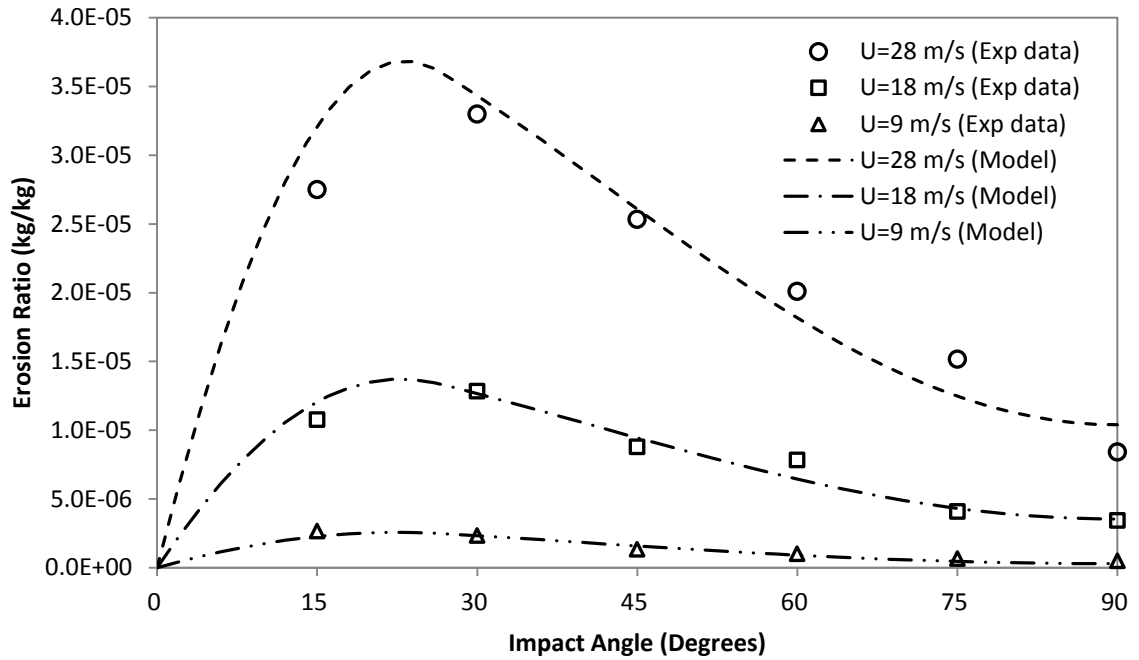
Figure 4.8 Erosion ratio of carbon steel 1018 at different impact velocities and
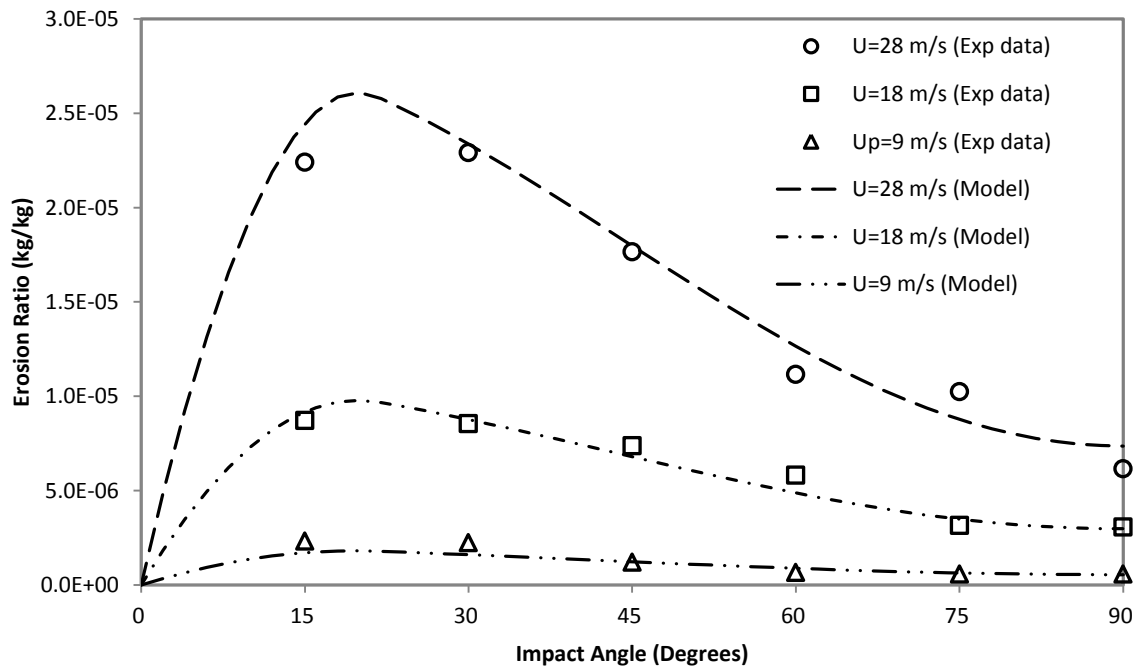
angles

Figure 4.9 Erosion ratio of stainless steel 2205

at different impact velocities and angles
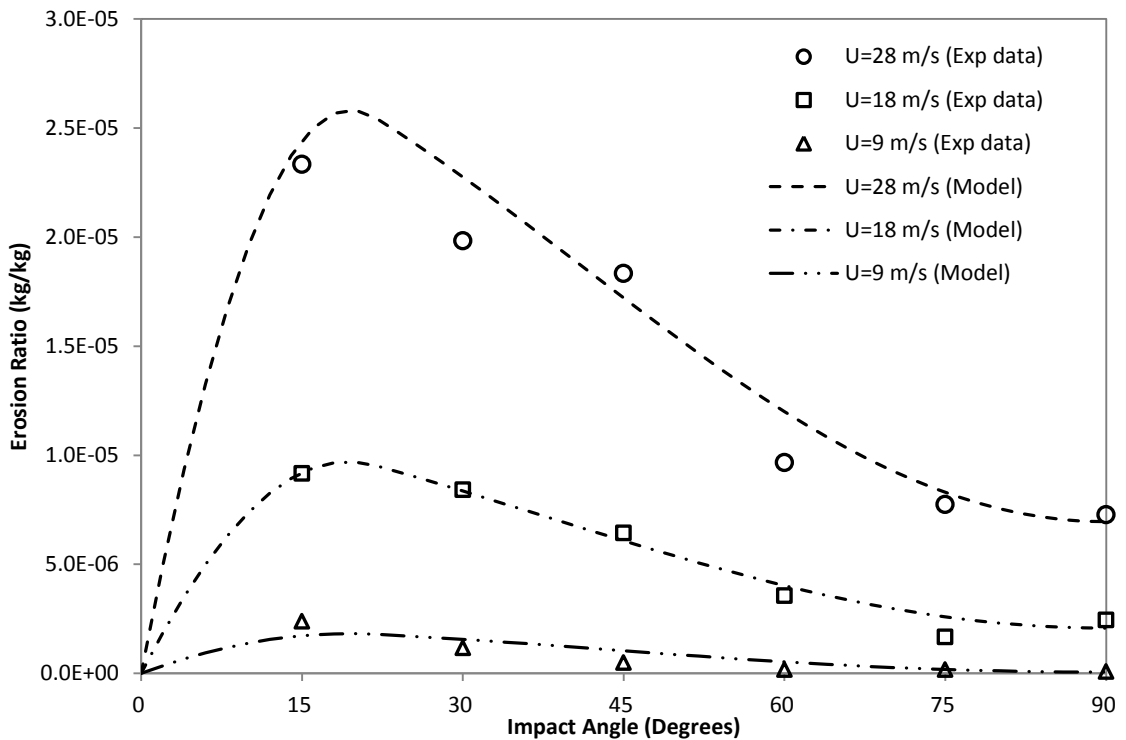
Figure 4.10 Erosion ratio of aluminum alloy 6061

at different impact velocities and angles

In this erosion equation, the angle dependency of erosion varies with velocity. At impact velocity lower than threshold velocity, the deformation erosion is negligible. By increasing the particle impact velocity, the deformation erosion term become appreciable especially at normal impact and changes the angle dependence of the erosion ratio. Figure 4.11 shows normalized erosion ratio with respect to the maximum value for each impact velocity. It is observed that the angle function is not the same at all impact velocities, and a feature of the new model is that it captures angle function variation with impact velocity. This phenomenon is not important at impact velocities higher than the threshold velocity (Oka et al. 1997).
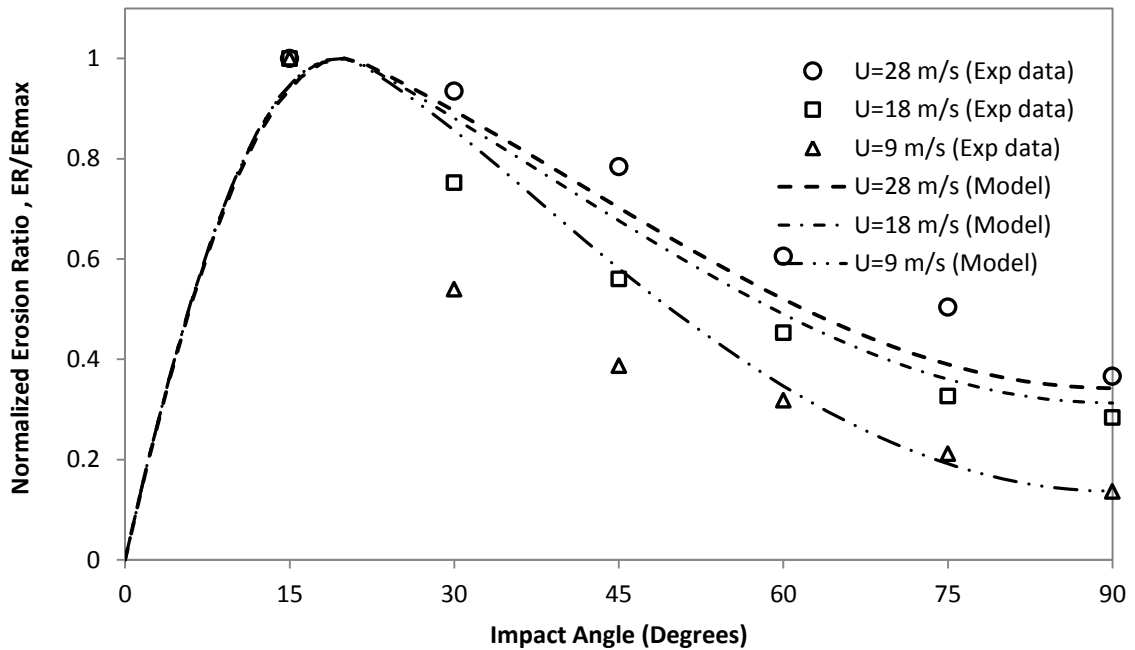
Figure 4.11 Normalized ER of Inconel 625 at different impact velocities and angles

In another comparison, model predictions are compared to experimental data of stainless steel 316 (Vieira 2014) eroded with 300 μm sand particles at different velocities and impact angles (Figure 4.12). It is important to note that the model is developed with experimental data for 150 μm sand and only two parameters have been changed. Threshold velocity is decreased from 5.8 to 2 m/s based on the concept that kinetic energy of a 300 μm particle is about 8 times that of a 150 μm particle with the same velocity, and the sharpness factor is also increased to 1 because 300 μm sand particles are very angular.
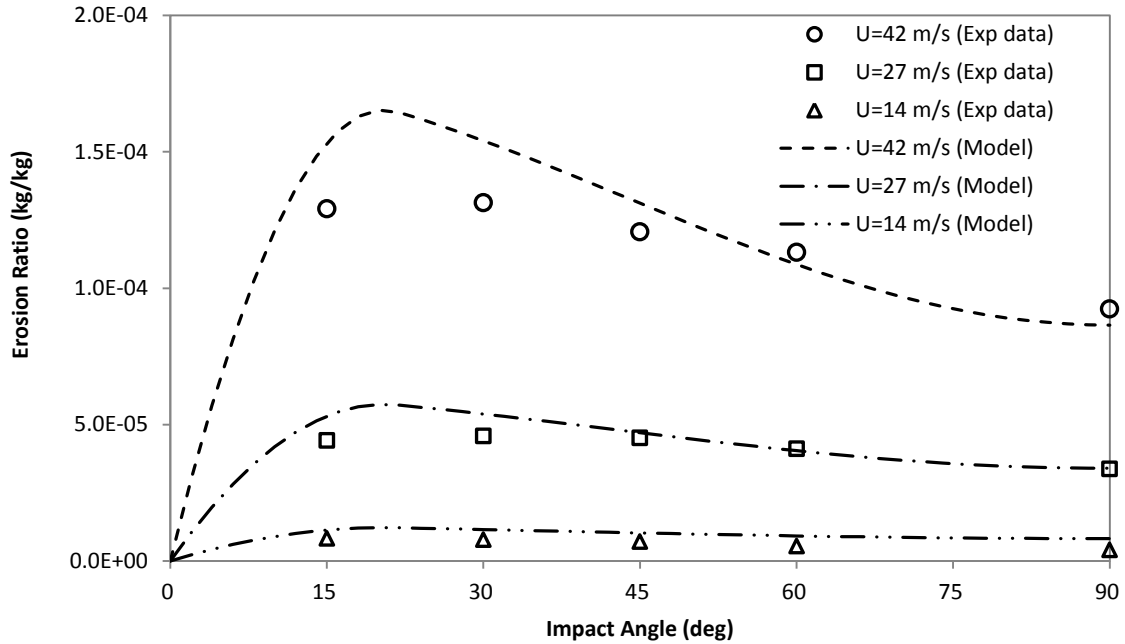
Figure 4.12 Erosion ratio of stainless steel 316

at different impact velocities and angles

In order to study the effect of particle shape on the angle dependency of erosion, the normalized erosion ratio of aluminum alloy 6061 eroded with 150 µm glass beads (Nidasanametla 2012) is compared to the corresponding values from 150 µm sand erosion tests (Figure 4.13). The markers are experimental data for 150 µm sand and glass beads, and the dashed, solid and dashed dot lines are model predictions for sand at high velocity and glass beads at high and low impact velocities, respectively. The value of K is increased from 0.4 for sand particles to 1 for glass beads based on Eq. (4.14). This shifts the location of maximum erosion to higher impact angles, which is in agreement with experimental data.
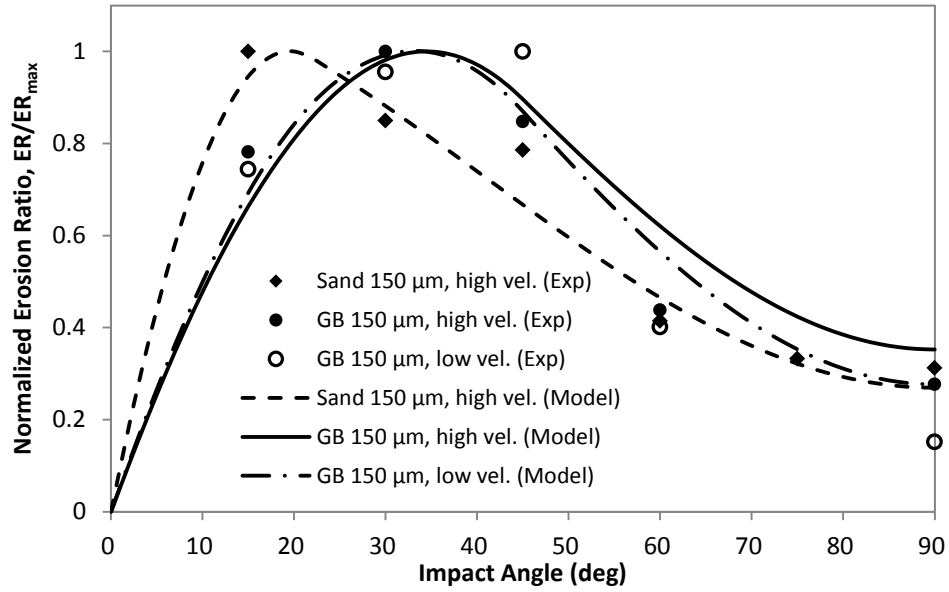
Figure 4.13 Normalized erosion ratio of aluminum alloy 6061

eroded with sand and glass beads

So the final form of the erosion equation is

$$ER_C = \begin{cases} C_1 F_S \dfrac{U^{2.41} \sin(\theta)[2K\cos(\theta) - \sin(\theta)]}{2K^2} & \theta < tan^{-1}(K) \\[4mm] C_1 F_S \dfrac{U^{2.41}\cos^2(\theta)}{2} & \theta > tan^{-1}(K) \end{cases} \qquad (4.15)$$

$$ER_D = C_2 F_S \frac{(U\sin\theta - U_{tsh})^2}{2} \qquad (4.16)$$

and the empirical constants for all tested materials are listed in Table 4.2. It should be noted that the values of K and U_{tsh} are listed for 150µm sand, and they should be adjusted for other particles.

Table 4.2 Empirical constants for the erosion equation

Material	C_1	C_2	K	U_{tsh} (m/s)
Carbon steel 1018	5.90E-08	4.25E-08	0.5	5.5
Carbon steel 4130	4.94E-08	3.02E-08	0.4	3.0
Stainless steel 316	4.58E-08	5.56E-08	0.4	5.8
Stainless steel 2205	3.92E-08	2.30E-08	0.4	2.3
13 chrome duplex	4.11E-08	3.09E-08	0.5	5.1
Inconel 625	4.58E-08	4.22E-08	0.4	5.5
Aluminum alloy 6061	3.96E-08	3.38E-08	0.4	7.3

4.5 Uncertainty Analysis and Error Propagation

4.5.1 Uncertainty in Velocity Measurement

The uncertainty in the velocity measurement originates from the gas velocity measurement by Pitot tube and particle velocity measurement by PIV. According to the error propagation rule (Taylor 1981), if q is any function of several variables x_1, x_2, x_3, …, x_n then

$$\delta q = \sqrt{\left(\frac{\partial q}{\partial x_1}\delta x_1\right)^2 + \cdots + \left(\frac{\partial q}{\partial x_n}\delta x_n\right)^2} \tag{4.17}$$

where δq is the estimated error for the function q from independent random errors in variables x_1, x_2, x_3, …, x_n. Recalling Eq. (3.3) on the relation of fluid velocity and the

measured dynamic pressure

$$V = \sqrt{\frac{2\,\Delta p}{\rho}} = \sqrt{2\,\Delta p \frac{RT}{p}} \tag{4.18}$$

where Δp is the measured dynamic pressure in Pa, ρ is gas density in kg/m^3, R is the ideal gas constant, T is the gas temperature in K and p is the gas pressure in Pa. So, the relative uncertainty in the Pitot tube measurement is

$$e_V = \frac{\delta q}{q} = \sqrt{e_{\Delta p}^2 + e_T^2 + e_p^2} \tag{4.19}$$

and

$$e_{\Delta p} = \frac{1}{\bar{V}} \frac{\partial V}{\partial\,\Delta p} u_{\Delta p} = \frac{1}{2} \frac{u_{\Delta p}}{\Delta p} \tag{4.20}$$

$$e_T = \frac{1}{\bar{V}} \frac{\partial V}{\partial T} u_T = \frac{1}{2} \frac{u_T}{T} \tag{4.21}$$

$$e_p = \frac{1}{\bar{V}} \frac{\partial V}{\partial p} u_p = -\frac{1}{2} \frac{u_p}{p} \tag{4.22}$$

in which $\bar{V}$ is the average measured velocity and u_x/x is the relative uncertainty in the measuring parameter x. Among the uncertainties in these parameters, the uncertainty in the dynamic pressure measurement is of great importance. Experimental measurement revealed that for the hand-held Pitot tube the dynamic pressure is fluctuating at most 0.5 inches of water which corresponds to 20% relative error in measuring 2.5 inches of water (0.5/2.5). The relative error decreases with increase in the dynamic pressure, but we are considering the worst case for error analysis. All of the measurements where done inside the building, so the temperature fluctuations should not exceed 5 K which corresponds to 1.7% (5/298) relative error. The variation in ambient pressure where the velocity is measured is also estimated to be less than 2% (0.3 psi / 14.7 psi) and will not be

considered here. So, the final uncertainty in the gas velocity measurement is

$$e_V = \sqrt{\frac{1}{4}(0.2)^2 + \frac{1}{4}(0.017)^2 + \frac{1}{4}(0.02)^2} = 0.101 \approx 10\% \qquad (4.23)$$

The uncertainty in particle velocity determination is of a different nature. Particles move in the nozzle with different velocities as the injection point is not far from the nozzle exit (about 6"), and the particles have not reached steady-state condition yet. The particle velocity fluctuations may be also due to the random nature of particle movement in turbulent gas flow in the pipe. PIV measurements are assumed to be accurate compared to uncertainties in the gas velocity measurements because this method uses high precision devices (laser, camera and synchronizer) to determine the particle velocity. The results of PIV measurements for 150 μm sand at different gas velocities are summarized in Table 4.3.

Table 4.3 Particle velocity measurement results for 150 μm sand

Dynamic pressure (in H$_2$O)	Air Velocity (m/s)	Particle Average Velocity (m/s)	Particle Velocity STD (m/s)	Relative Uncertainty (%)
5	45.9	15.8	4.1	26
10	64.9	20.4	5.9	29
15	79.5	22.7	5.1	22
20	91.8	30.1	8.7	29
25	102.7	33.4	9.1	27
30	112.5	35.1	7.9	22

The uncertainty values in Table 4.3 are higher than 10% which is the value obtained for the gas velocity, but it should be noted that particle velocity variations are

not errors in the measurements but are the nature of the erosion testing apparatus that yields a distribution of particle velocities. In a testing condition where the average velocity of particles is V, there are many particles (about 68% of the population based on the normal distributions) that move with velocity between $V - \sigma$ and $V + \sigma$ where σ is the particle velocity standard deviation. In other words, there are some particles that move faster than the average and at the same time some particles move slower than the average. Based on the experimental observation, the erosion is proportional to $V^{2.41}$. If we calculate the erosion caused by an individual particle in a particle stream at a specific gas velocity and compare it with the erosion calculated from the average particle velocity, we will find the effect of velocity uncertainty on the erosion ratio calculation. Table 4.4 shows the relative difference between the erosion caused by individual particles and erosion from the representative average particle velocity.

Table 4.4 Effect of particle velocity uncertainty on erosion

Particle Average Velocity (m/s)	$V_{avg}^{2.41}$	$\dfrac{1}{n}\displaystyle\sum_{i=1}^{n} V_i^{2.41}$	Relative error (%)
15.8	768.6	929.4	-10
20.4	1425.7	1587.9	-12
22.7	1848.9	1965.1	-8
30.1	3570.2	3855.8	-12
33.4	4652.2	4980.7	-11
35.1	5108.5	5543.9	-11

The average relative error in Table 4.4 is 11% about half of the average relative uncertainty in Table 4.3 (26%), but from the uncertainty estimation equation (Eq. 4.17) it

51

is

$$\frac{\delta\ ER}{ER} = 2.41\frac{\delta\ V}{V} \approx 2.41(26\%) \approx 63\% \tag{4.24}$$

The reason that we obtained 17% compared to 63% is probably the compensation effect of faster and slower particles than the average. We will take into account both cases, uncertainty in the gas velocity determination and uncertainty in the particle velocity determination in the final erosion equation.

4.5.2 Uncertainty in Mass Loss Measurement

As described in detail in Chapter 3, the mass loss is measured by a digital scale, and a line is fit through the cumulative mass loss points versus sand throughput. Table 4.5 shows the standard relative error in the coefficient of the regression line.

Table 4.5 Relative uncertainty in the erosion ratio determination from mass loss

Material	Average standard relative error (%)		
	9.2 (m/s)	18.4 (m/s)	27.6 (m/s)
Carbon steel 1018	6.8	7.3	2.4
Carbon steel 4130	11.5	4.5	6.1
Stainless steel 316	24.9	4.6	3.8
Stainless steel 2205	7.2	6.4	11.0
13 chrome duplex	8.7	3.9	4.8
Inconel 625	12.4	4.7	3.9
Aluminum alloy 6061	38.6	8.2	8.7

The average value for all materials and particle velocities is about 9%, which is

consistent with the weight measurement scale uncertainty (±0.0002 g / 0.0020 g).

4.5.3 Error Propagation in Erosion Ratio Equation

The erosion equation is developed based on experimental data including particle velocity and weight loss of the tested coupon. Based on Eq. (4.17) and applying error propagation rules, the uncertainty in the empirical constants in the erosion equation is

$$e_{ER} = \sqrt{e_V{}^2 + e_{\text{mass loss}}^2} \qquad (4.25)$$

Table 4.6 shows the average relative uncertainty in the erosion ratio resulting from uncertainty in the velocity measurement, either gas velocity or particle velocity, and mass loss measurement. The uncertainty due to particle velocity determination is evaluated in two ways. First, it is assumed that the uncertainty from particle velocity (which is 26% on average) propagates according to Eq. (4.17) and for the second case, the compensation effect of particles with lower velocity than the average and particles with higher velocity than the average is considered. The results show that even 60% error in the erosion ratio is not surprising but the most realistic estimate of max uncertainty would be 26% because of the uncertainty in gas velocity and mass loss measurement.

Table 4.6 Quantification of relative uncertainty in the erosion ratio

Parameter	Uncertainty in Erosion Ratio (%)		
	due to gas velocity	due to particle velocity	
Velocity uncertainty	2.41×10	2.41×26	11
Mass loss uncertainty	9	9	9
Total uncertainty	25.7	63.3	14.2

Figure 4.14 shows the experimental data and model prediction of erosion ratio for stainless steel 316 and the error bars shows the corresponding 26% uncertainty.
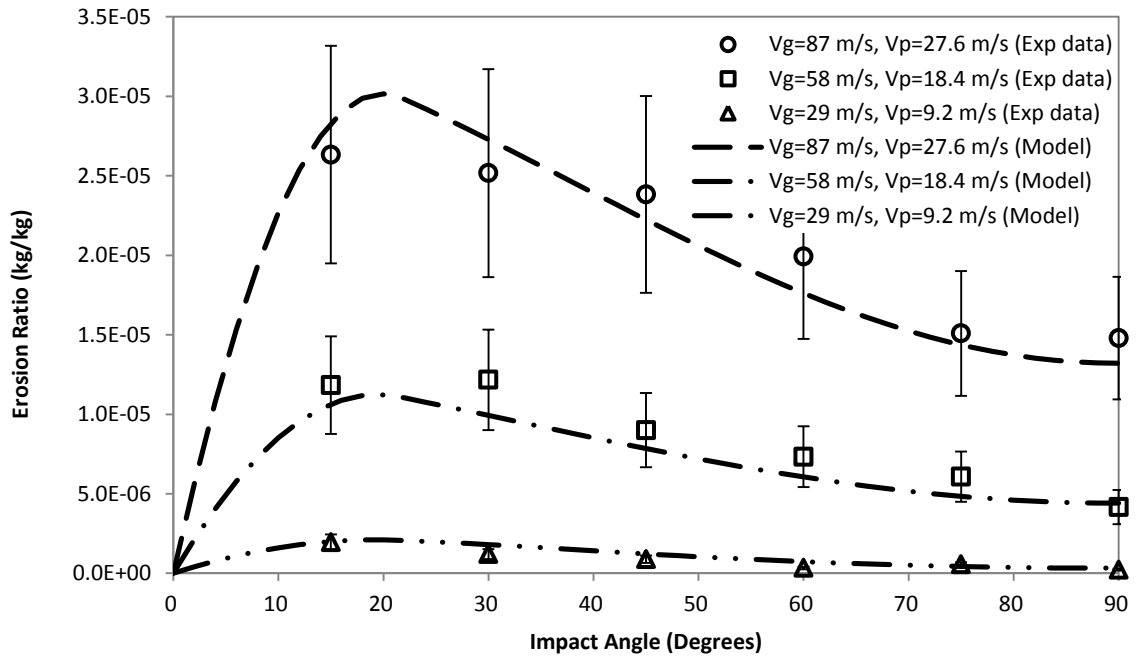
Figure 4.14 Erosion ratio of stainless steel 316

at different impact velocities and angles

CHAPTER 5

EROSION BY SOLID PARTICLES OTHER THAN SAND

5.1 Introduction

In the previous chapter, we studied the erosion caused by sand particles but there are some other solid particles that may cause erosion. The examples are some scale products such as calcite, magnetite, hematite and barite and these particles may also cause erosion. Calcite is one of the main scale products which is formed due to changes in conditions of the fluid in the reservoir. Black powder which is mainly composed of magnetite is another scale product which forms in the presence of water, oxygen, hydrogen sulfide and carbon dioxide from corrosion of ferrous steel pipe, and hematite is another corrosion scale of ferrous steel pipe. Barite is a scale product that forms when sea water which is rich in sulfate ions comes in contact with the barium ion in the brine. Moreover, some of these particles are being used as a densifying agent in particulate well kill fluids.

Although significant work has been conducted on sand erosion, the erosion of other particles has not been widely investigated. Levy et al. (1983) examined effects of particle characteristics on erosion of AISI 1020 carbon steel. Particles examined were calcium carbonate (calcite), silica flour, aluminum oxide, silicon carbide and steel. The particles were sharp and the sizes ranged from 180 to 250 μm, and two impact angles were examined at an impact velocity of 80 m/s. Measured erosion ratios (mass of target

material/mass of impacting particles) were much lower than sand when a soft erodent such as calcite was used as the erodent. They concluded that particles with lower hardness than sand may shatter when they impact the target at this high velocity, and this may cause the particle fragments to be embedded into the steel target thereby protecting the target material from subsequent impacts and reducing erosion rate. Additionally, particles with higher hardness values than sand such as aluminum oxide and silicon carbide did not cause higher erosion ratios than sand. But, Babu et al. (2011) indicated that for harder target materials such as tungsten carbide, SiC particles caused more erosion than sand. Wada et al. (1987) proposed a correlation that erosion rate of target material depends on the ratio of the target material hardness to the impacting particle hardness raised to an exponent. Shipway et al. (1996) also investigated the effects of particle hardness on various target materials and concluded that increasing the ratio of the erodent particles to the target material hardness increases the erosion rate and even affects the velocity exponent on erosion rate. In general, characteristics of both target and erodent particles including density and hardness may be important in addition to shape and size of particles. High velocity of larger impacting particles may also cause fragmentation of particles and cause impacting soft particles to embed inside the target materials affecting erosion data.

Iron oxides, calcium carbonate, barite and silica represent some of the small solid particles that are entrained in liquids and may impact oil and gas pipelines and equipment at much lower velocities than those examined previously by other investigators. Akbarzadeh et al. (2012) studied the erosive behavior of magnetite particles on different materials at 90 and 130 m/s. There are limited data available about erosive behavior of

small scale products at lower velocities, especially when they are entrained in the liquid.

As stated earlier, erosion is a function of different parameters including particle size, shape and hardness and because of the different characteristics (exclusively hardness) of the new particles, sand erosion models are not applicable to calculate erosion resulting from these particles.

5.2 Experimental data

In this work, two experimental apparatuses have been used, (1) particles entrained in submerged liquid jet in a slurry tank and (2) gas testing with liquid droplets containing particles, and the tests have been conducted with nine erodent particles. The details of experimental setup is described in Chapter 2. The small erodent particles that have been selected have a wide range of properties (see Table 5.1). Iron powder is the softest particle with a hardness of 65 kgf mm^{-2} using the Vickers scale, and silicon carbide is the hardest (3000 kgf mm^{-2}). The average size varies from 2 μm (for magnetite) to 40 μm (for apatite), and the density range is from 2650 to 7860 kg/m^3 for silica flour and iron powder, respectively. Scanning electron microscope (SEM) images of some of these particles are shown in Figure 5.1. For some of these particles, the average size was unknown, and SEM images have been processed to characterize the particle size distribution. Figures 5.2 to 5.6 show the particle size distributions for iron powder, calcite, barite, magnetite and silica flour, respectively. Density and size of particles affect their impact velocity as they move in the liquid layers formed on the target wall by the jet or droplet impacts. It is required to estimate the impact velocities to find a correlation

between the particle hardness and induced erosion. CFD simulations and particle tracking were used to estimate the average impact velocity for each case, but droplet velocity is not the same as gas velocity in mist flow testing and was measured by particle image velocimeter (PIV).

Table 5.1 Erodent particle properties

Particle	Density (kg/m^3)	Average size (µm)	Hardness (VHN)
Iron powder (Fe)	7860	32	65
Calcite ($CaCO_3$)	2710	6	145
Barite ($BaSO_4$)	4300	38	173
Apatite ($Ca_5(PO_4)_3$)	3140	40	300
Hematite (Fe_2O_3)	5260	30	600
Magnetite (Fe_3O_4)	5170	2	680
Silica Flour (SiO_2)	2650	24	1000
Alumina (Al_2O_3)	3950	20	2000
Silicon Carbide (SiC)	3210	20	3000
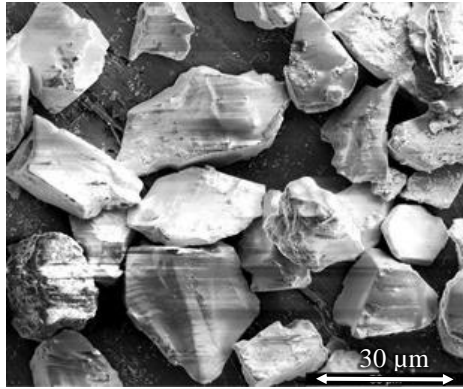
Alumina
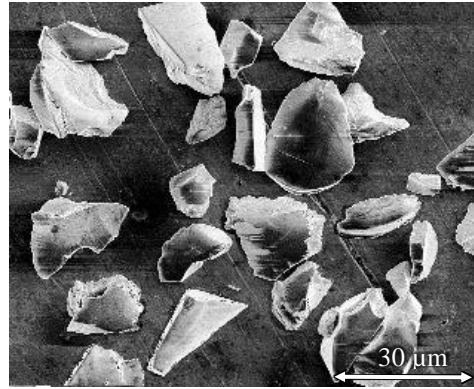
Silicon carbide
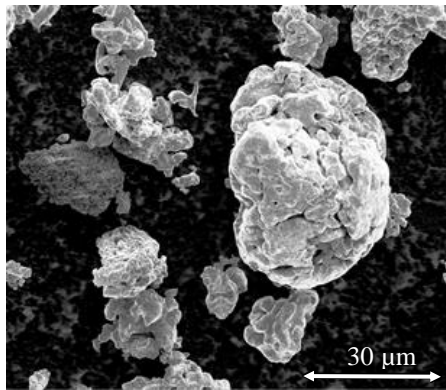
Iron powder
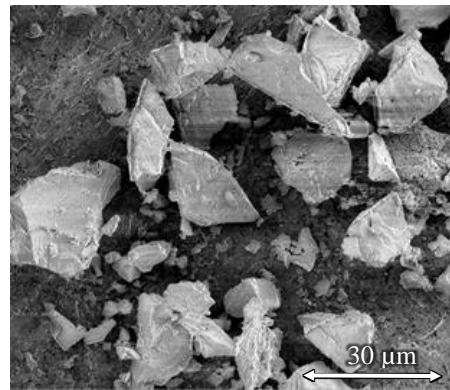
Silica flour
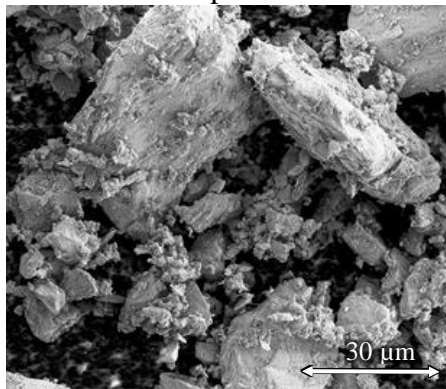
Barite
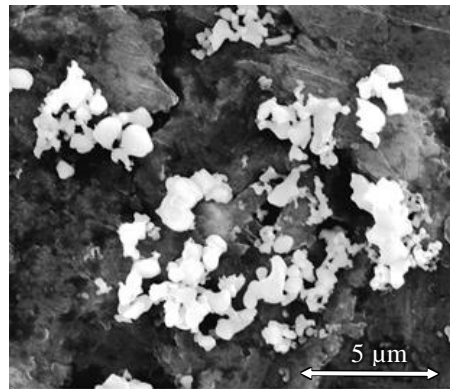
Magnetite

Figure 5.1 SEM images of erodent particles
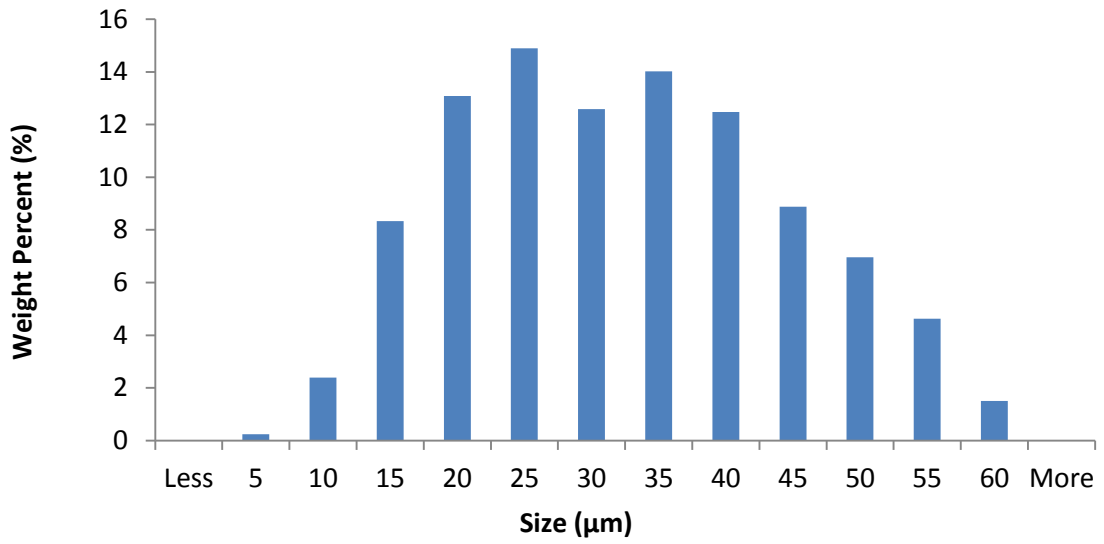
Figure 5.2 Iron powder particle size distribution
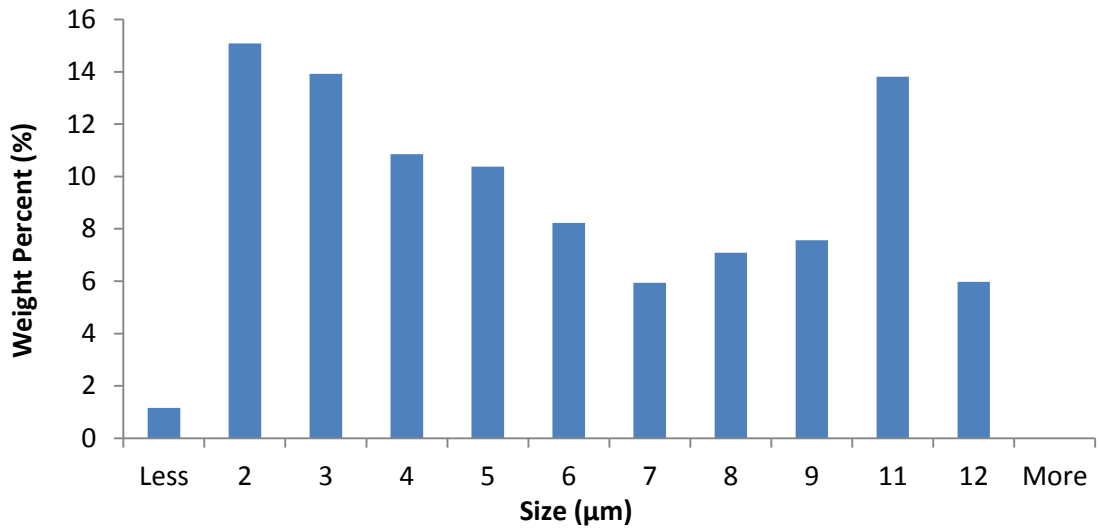
Figure 5.3 Calcite particle size distribution
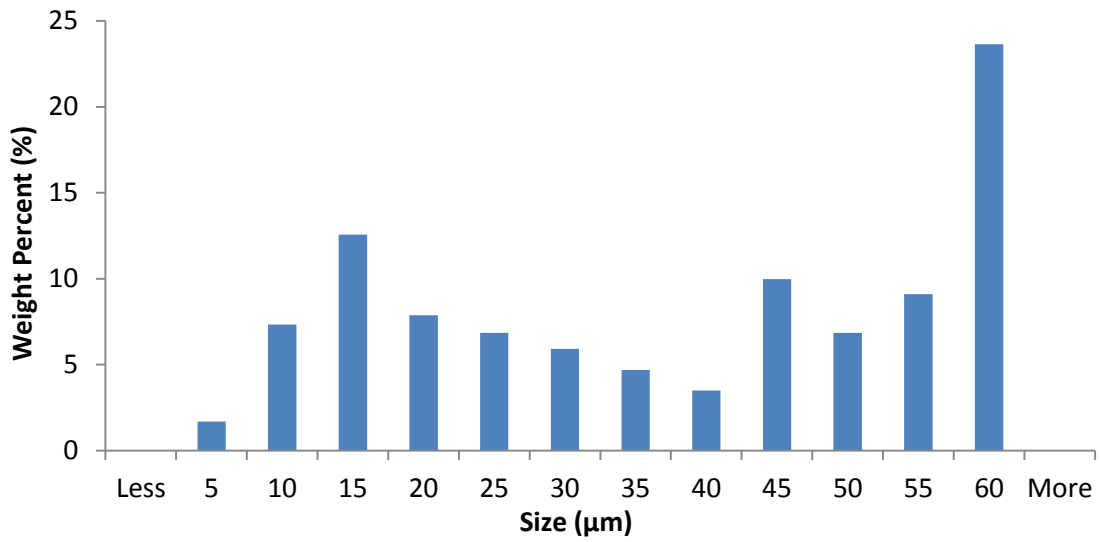
Figure 5.4 Barite particle size distribution
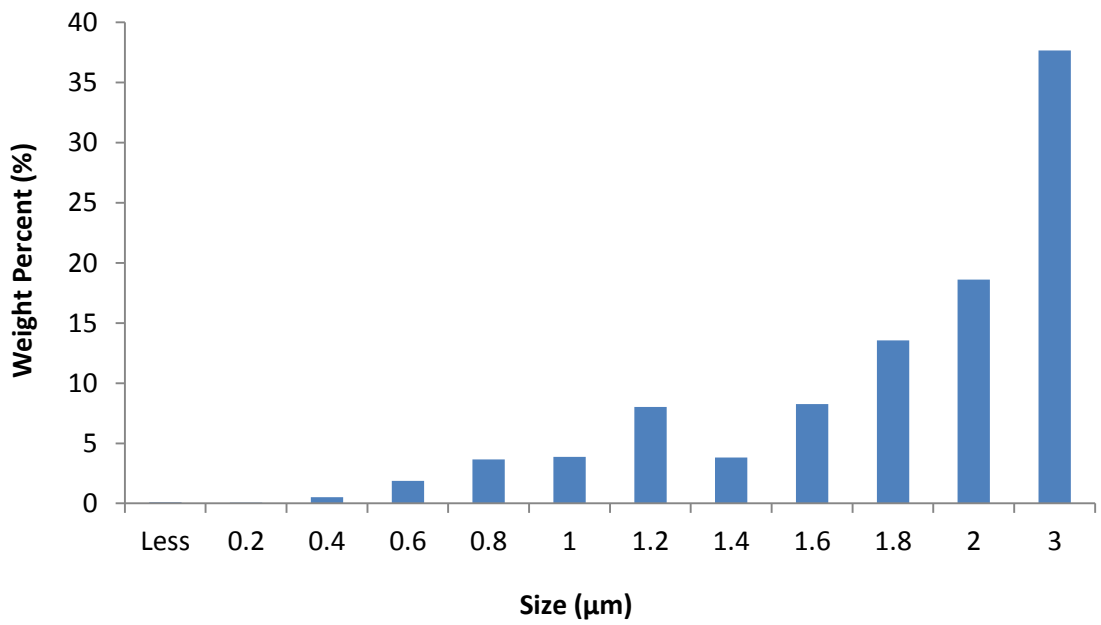
Figure 5.5 Magnetite particle size distribution
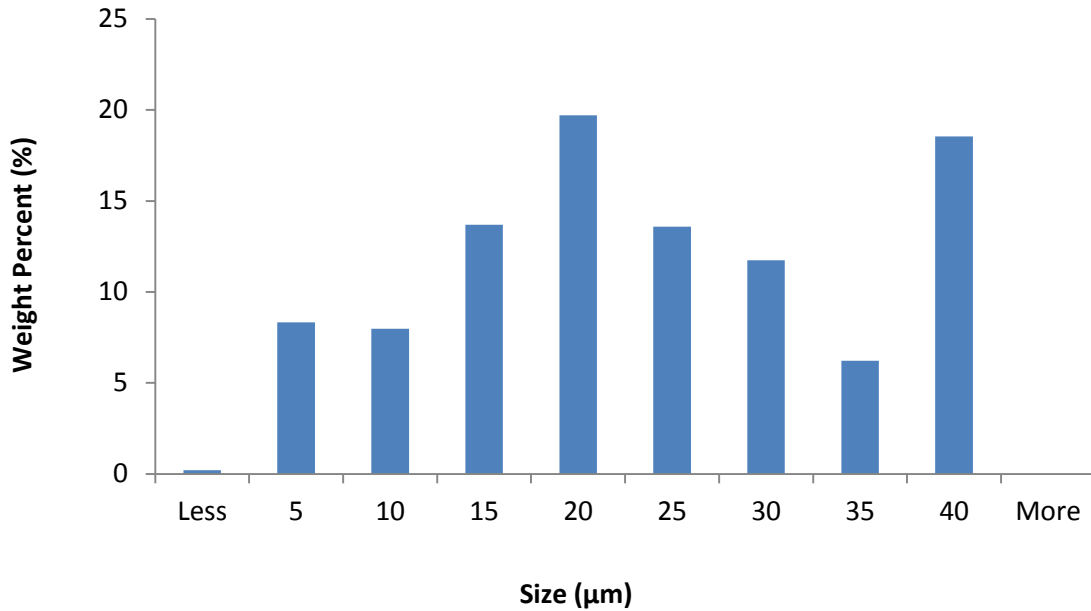
Figure 5.6 Silica flour particle size distribution

Figure 5.7 shows mass loss of the SS-316 specimens after 72 hours of testing in both submerged and mist flow configurations. Markers are experimental data points and solid and dashed-dot lines are the average of three experiments conducted at same condition to show repeatability of the results. The particle throughput in the two experimental apparatuses was different, so the mass loss values are converted to erosion ratio (ratio of mass loss to the mass of particles throughput based on concentration and liquid rate) and plotted in Figure 5.8. Squares are data points for submerged tests, and diamonds represents mist flow data. Mass losses of the specimens in the submerged test were higher than what was observed in the mist flow tests because the liquid flow rate and particle impingement rate were higher, but the erosion ratio is relatively consistent in the two experiments for most of the particles as it is normalized by the particles throughput. It should be noted that particles that are impacting the target are impacting at

different impact velocities due to differences in density and size as they slip through the liquid protecting the target, and thereby their velocities are much smaller than the liquid jet and gas velocities.
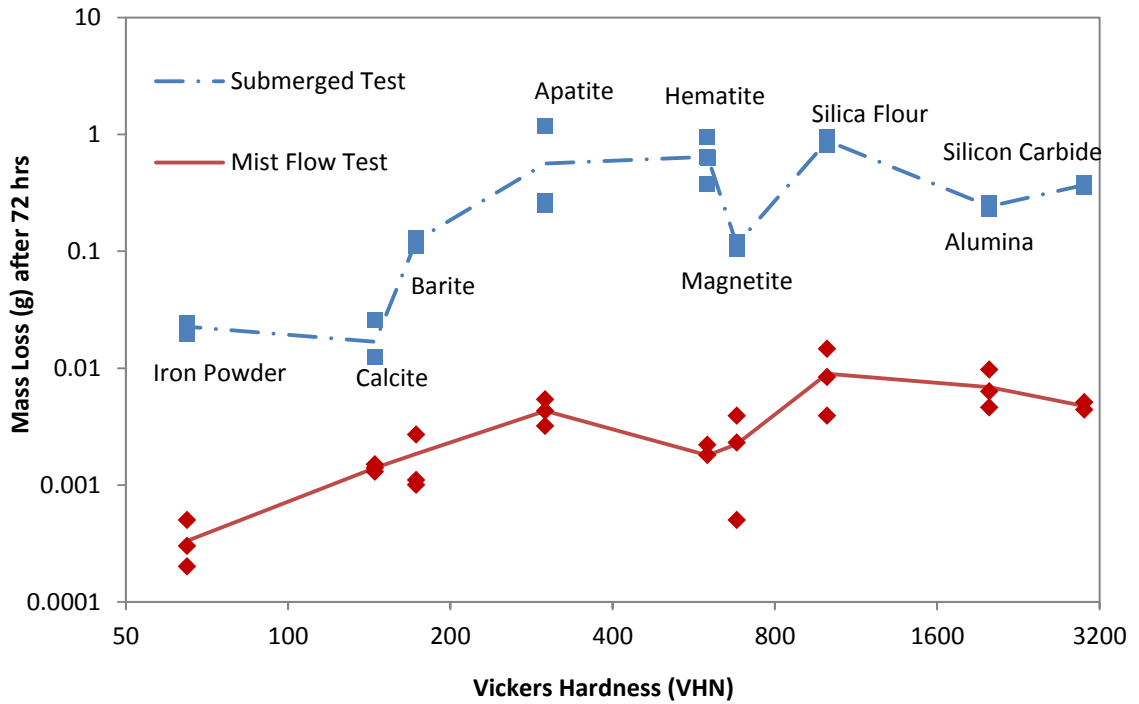
Figure 5.7 SS-316 mass loss after 72 hours in submerged and mist flow tests
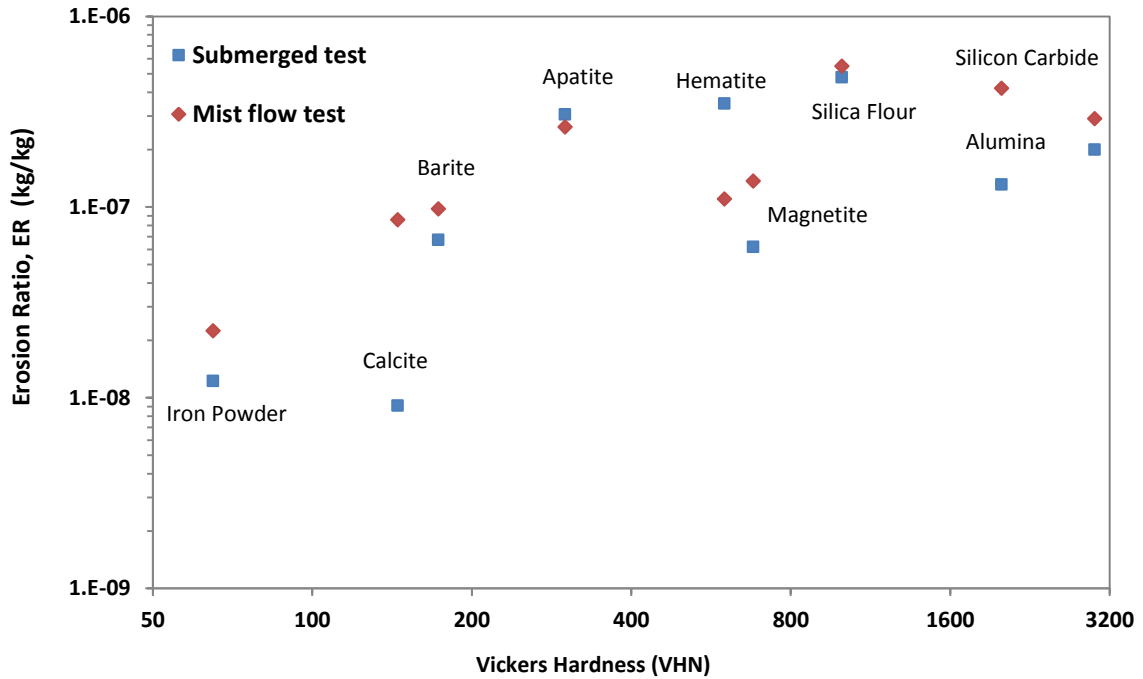
Figure 5.8 Erosion ratio of the SS-316 specimens for different particles

In order to correlate erosion with particle properties, particle angularity and impact velocity must be known. Powers (1953) classified particles into six categories based on their roundness: very angular, angular, sub-angular, sub-rounded, rounded and well-rounded as shown in Figure 5.9. Experimental results at the Erosion/Corrosion Research Center (E/CRC) showed that well rounded particles (glass beads) cause four to five times less erosion than very angular particles (sharp sand), and this phenomenon has been observed by other researchers (Desale, et al. 2006; Bahadur, et al. 1990). So, angularity numbers have been assigned to each category from 0.25 for well rounded up to 1.0 for very angular particles and the other categories take numbers in between. Table 5.2 shows angularity numbers assigned to each particle based on the visual observation under SEM (Figure 5.1). The angularity factor that has been assigned to the particles in this study ranges from 0.5 to 1. Angularity factors less than 0.5 are not applicable to these

particles because none of these particles are rounded or well-rounded as observed in the SEM micrographs. So, the possible error associated with this method will be confined in the specified range.
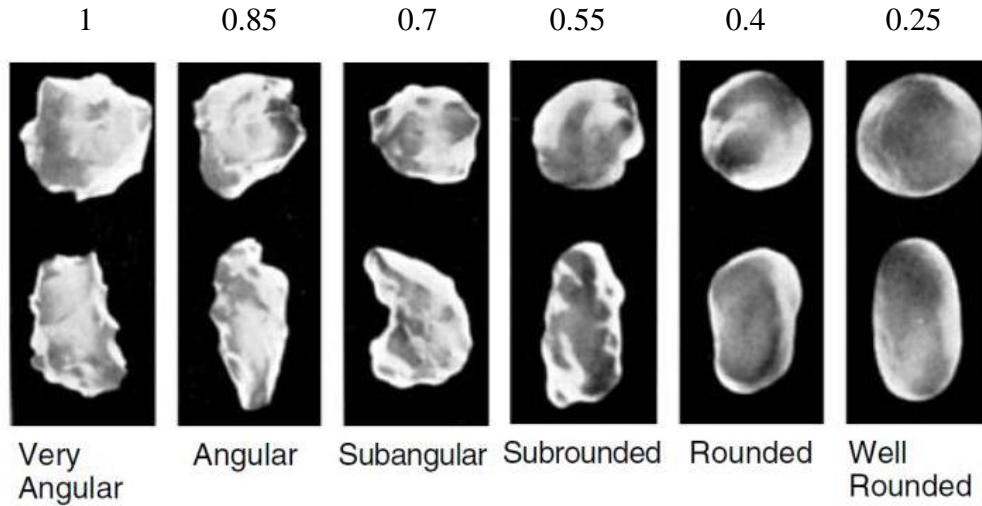
Figure 5.9 Classification of the particles according to their shape (Powers 1953)

Figure 5.10 shows surfaces of SS-316 specimens eroded by silica flour, iron powder, barite and magnetite. The top image is in the center of the impacting area, and the lower images show the eroded surfaces at 4 mm from the center. At the center, particles impact the specimen normally and platelets are formed on the surface which may lead to surface failure after repetitive impacts. At locations far from this point, particles impact the specimen at grazing angles and craters are formed on the surface in so called scouring erosion phenomenon. The SEM images did not show any fragments of particles embedded as the impact velocities of these particles with the SS-316 material are fairly low as shown below. This was confirmed by using Energy Dispersive X-ray Spectroscopy (EDX) in the locations that were suspicious to have embedded particles after the test. It is noted that craters created by silica sand are much deeper than others,

and even tiny magnetite particles create craters that are similar to larger silica sand.

Silica flour	Iron powder
Barite	Magnetite
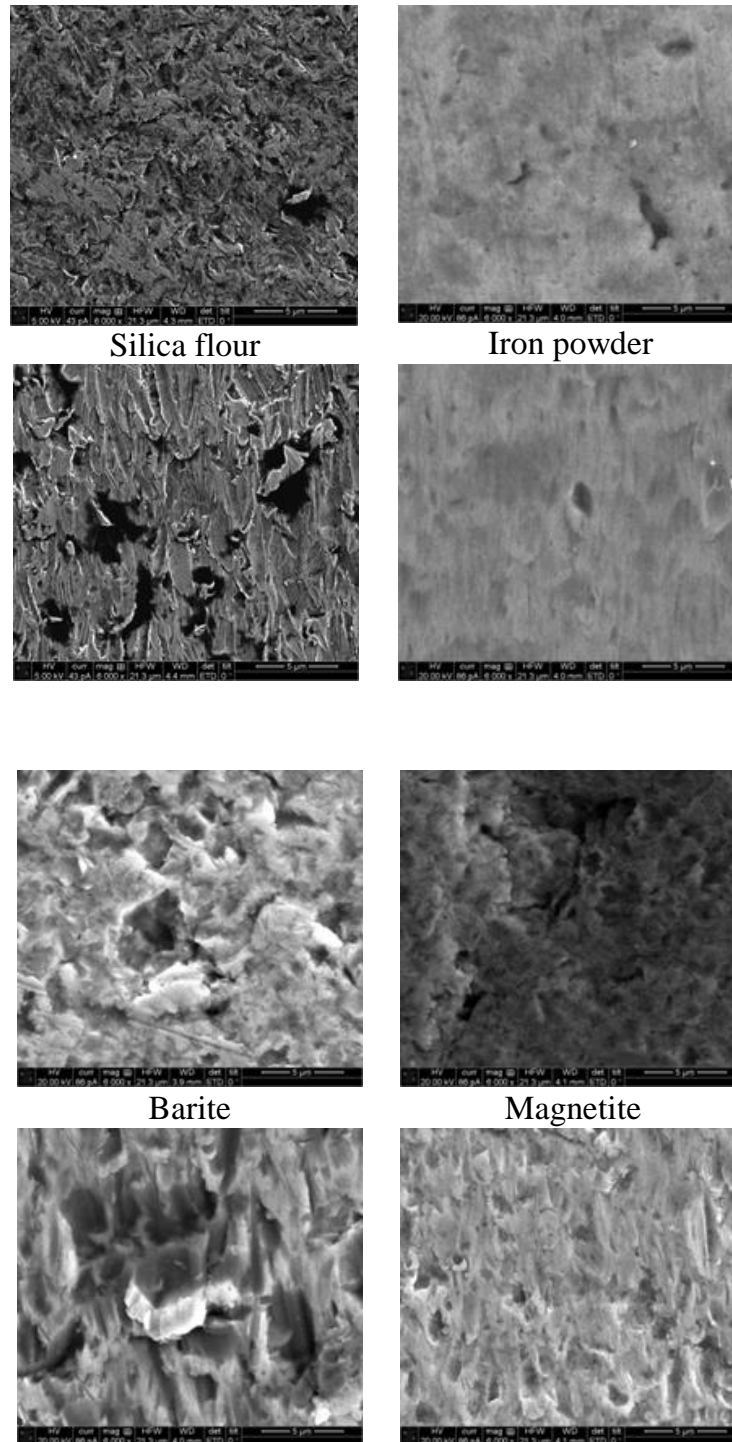
Figure 5.10 SEM micrographs of different locations on SS-316 specimens eroded with different particles

5.3 Data Analysis and CFD Simulation

It is well known that the major contributor to erosion is impact velocity of particles. Thus, significant work was dedicated to estimate the representative impact velocities of these particles. To estimate impact velocity of particles that were entrained in the liquid droplets, the velocities of droplets were first measured by PIV. Then for both submerged and mist flow tests, CFD simulations and particle tracking inside the liquid droplet or jet were conducted to estimate the impact velocity of particles that penetrate into the liquid layer formed by droplets or continuous jet impact.

ANSYS Fluent is used to study relative motion of the particles with respect to liquid when it is spreading out on the wall. The simulation for submerged slurry jet impact was done with the turbulent Reynolds stress model, and after obtaining the steady-state flow solution, particles were injected at the nozzle exit and modeled as a discrete phase (DPM) and traced until they leave the simulation domain. Figure 5.11-a and 5.11-b show velocity contours and particle traces in the submerged configuration, respectively. For droplets containing small particles, the simulation is more complex. Transient multiphase flow with volume of fluid (VOF) model was used to simulate a droplet moving with an initial velocity measured by PIV toward the wall. The initial particle location, size and velocity were set through an injection file in Fluent and particles traced until they leave the simulation domain. It is assumed that the droplet and particles that are inside the droplet have the same initial velocity, and particles are distributed uniformly in the droplet. For droplet impact, the simulation was done with a laminar fluid model with uniform mesh over the 10 mm by 15 mm field and the cell size was 5×10^{-5} m. A variable time step was used to keep the Courant number below one. The resulting time step was

approximately 1 µs.

Figure 5.11-c shows a sequence of a droplet with particles inside during impact. The velocity of impacting particles was not constant, and the average value from simulations for both cases is reported in Table 5-2.

a)   b)

c)
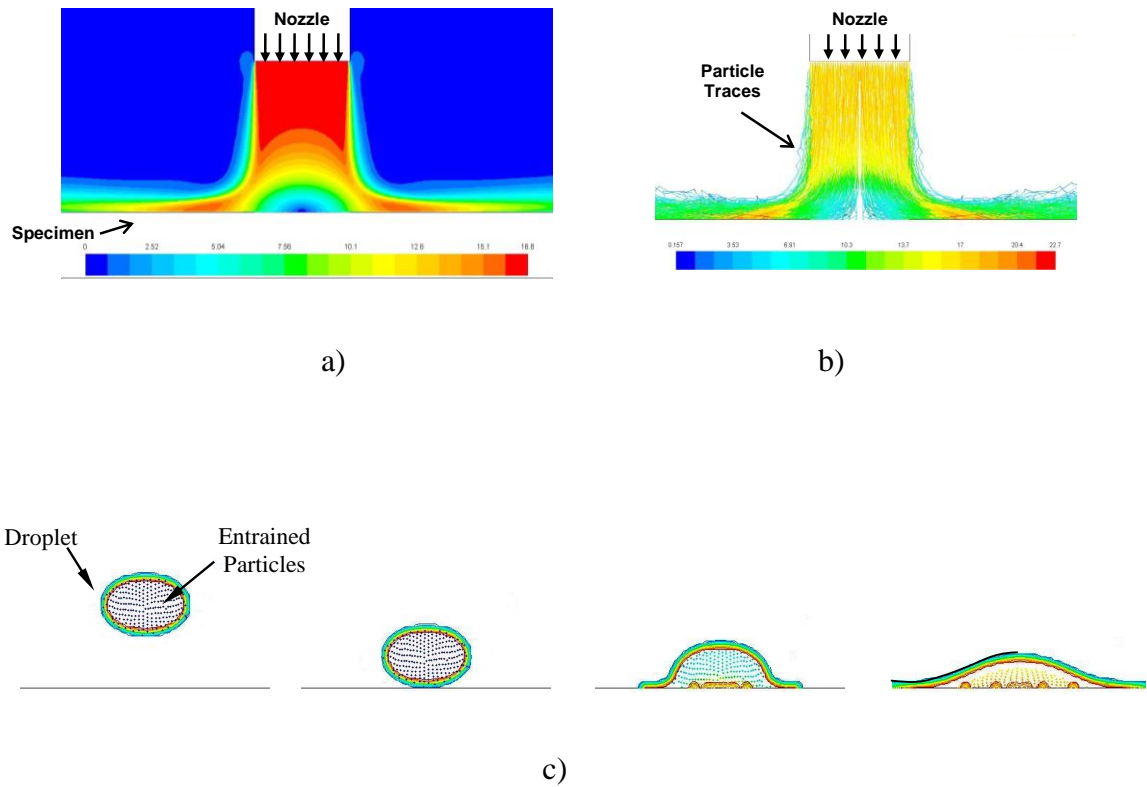
Figure 5.11 CFD simulation and particle tracking results, a) velocity contours and b) particle traces in submerged jet flow and c) sequences of droplet impact with particles

Table 5.2 Average particle impact velocity and angularity

Particle	Angularity	Representative normal component of impact velocity in submerged test (m/s)	Average normal component of impact velocity in mist flow tests (m/s)
Iron powder (Fe)	0.50	3.76	6.86
Calcite ($CaCO_3$)	0.75	1.67	2.66
Barite ($BaSO_4$)	0.70	3.45	6.17
Apatite ($Ca_5(PO_4)_3$)	0.75	3.16	5.36
Hematite (Fe_2O_3)	0.75	2.99	3.70
Magnetite (Fe_3O_4)	0.75	1.62	2.10
Silica Flour (SiO_2)	1.00	2.75	3.10
Alumina (Al_2O_3)	1.00	2.11	3.33
Silicon Carbide (SiC)	1.00	1.97	2.89

5.4 Effect of Particle Hardness on Erosion

Figure 5.12 shows test results for submerged and droplet testing obtained in this study and Levy's data in the literature that was gathered using an experimental facility, procedure and velocities that were much different than the current study and were obtained for much larger particles entrained in gas streams (Levy 1995). The vertical axis is erosion ratio divided by the normal impact velocity squared to consider the effect of particle size and density that affect deceleration of a particle when it enters the viscous

layer near the wall and divided by the angularity factor obtained from visual observation of the particles under SEM. Considering that these data were gathered with three experimental facilities that were considerably different with particle impact velocities ranging from 2 to 80 m/s, the normalized data appear to line up well as a function of Vickers hardness of the particles.
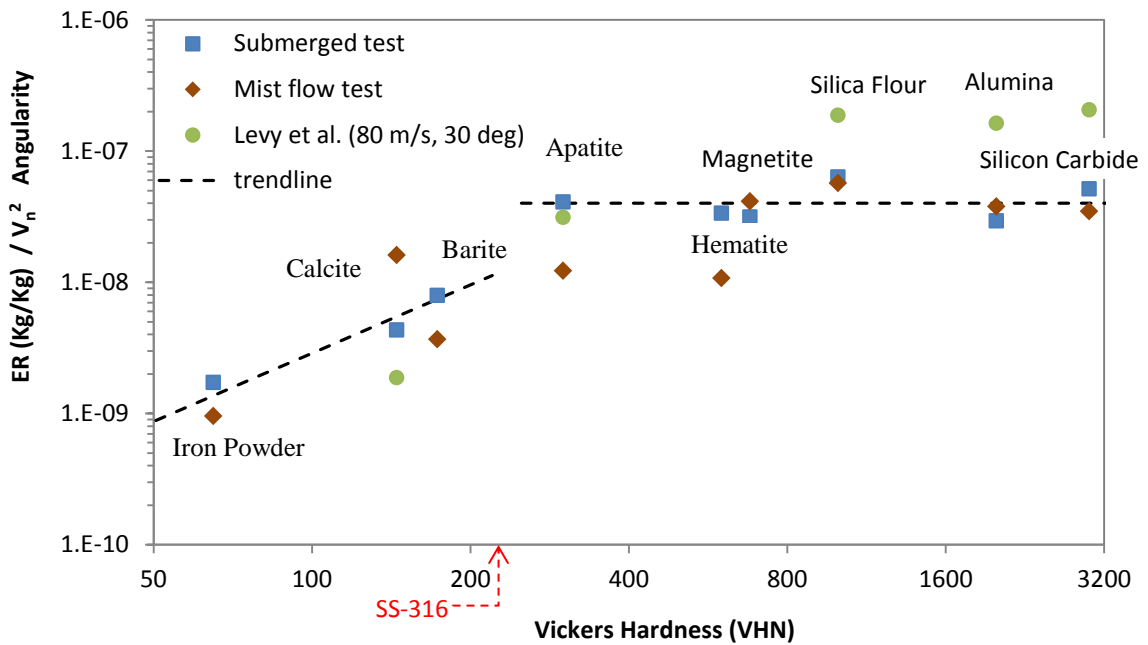
Figure 5.12 Correlation between normalized erosion and particle hardness

The dashed line in Figure 5.12 is passed through the data points for which the hardness of the particle is less than the hardness of SS-316 (~ 220) and other particles separately. The overall trend of experimental data shows that erosion increases with particle hardness, but as observed in Figure 5.7 the hardness effect is remarkable when the hardness of particle is less than the hardness of target material and erosion ratio does not increase significantly when the particle hardness is higher than the material hardness

and the particle keeps its integrity during impact. The erosivity of the particles depends on their ability to concentrate force locally on the target (Levy et al. 1983, Shipway et al. 1996). When impacting particles are not as hard as the target material, they may deform during impact, and their kinetic energy will not be effectively transferred to the target material.

CHAPTER 6

LIQUID DROPLET EROSION MODELING

6.1 Introduction

There are many high productivity gas wells around the globe that can produce large volumes of gas and condensate but are being choked to prevent erosion and erosion-corrosion. Pipe walls are subjected to erosion not only by sand particles but also by liquid droplets, and many oil and gas operators believe that the threshold velocity for sand free production should be based on liquid impact erosion.

In this study, experimental data and a corresponding method in the literature for erosion caused by liquid impacts are utilized and their applicability to the oil and gas industry has been examined. Experimental data that has been obtained for several oilfield materials and the method developed in this study are used to develop a model to predict the erosion ratio (ratio of volume loss of material to volume of water impinging) of these materials for a desired condition. This model has been implemented into a method for predicting droplet impact velocities to predict erosion caused by liquid impacts and calculate thickness loss rate of oilfield elbow materials for different conditions.

Two cases that are susceptible to become eroded by liquid impacts are shown in Figure 6.1. In the case when liquid droplets pass through an orifice or in choke flow, liquid droplets may hit the wall and cause erosion. In another scenario, for two-phase flow through an elbow, liquid droplets may hit the pipe wall and cause erosion.
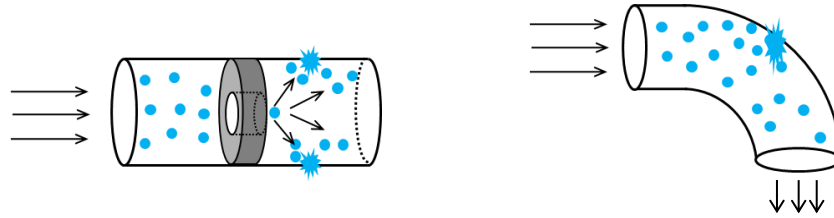
Figure 6.1 Two possible cases for liquid droplet impingement erosion

6.2 Experimental Data

In the literature, two major types of experimental methods to evaluate the material integrity exposed to liquid droplet impacts have been utilized. In the first type, specimens are mounted on a rotating disk or arm and cut through a liquid jet or liquid droplet stream (see Figure 6.2-a). In the second type, a liquid jet or droplet stream is accelerated to hit a fixed specimen as shown in Figure 6.2-b. Experimental results show that there is a significant difference between the results provided by these two types experiment.

(a)   (b)
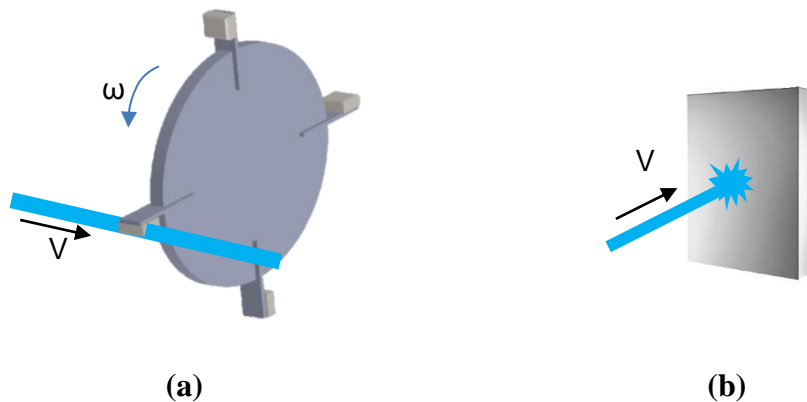
Figure 6.2 Rotating arm and liquid jet erosion experiment schematics

Some of the experimental studies in the literature are as follows. Thiruvengadam et al. (1970) used aluminum-1100 and SS-316 with diameter of $3/8^{th}$ inch mounted on a

rotating disk cutting through a $1/16^{th}$ inch jet of water. In Figure 6.3 the number of impacts required to initiate erosion is shown on the horizontal axis, whereas the vertical axis shows the corresponding impact velocity. The circle markers show experimental values for SS-316, and the threshold velocity is estimated to be 150 ft/s. Triangle markers show values for aluminum, and the corresponding threshold velocity is found to be 50 ft/s.
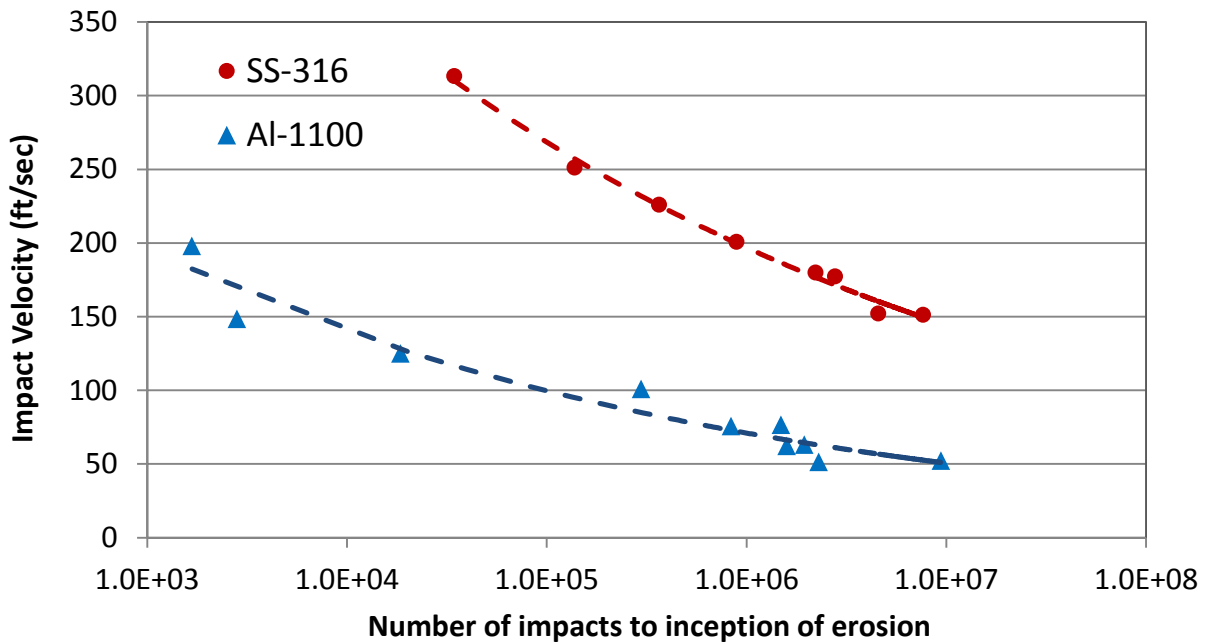
Figure 6.3 Effect of impact velocity on liquid impact erosion inception

In another study, Baker et al. (1966) used a 12% Chromium Steel specimen rotating on a disk, hitting water droplets. As shown in Figure 6.4, the maximum values of erosion rate for different liquid droplet sizes are obtained versus different impact velocities. The maximum erosion rate is for the maximum size of droplets, 1050 microns, and the threshold velocity is found to be 120 m/s (390 ft/s).

Another recent example is the work conducted by Higashi et al. (2009). He used a specimen mounted on a rotating disk cutting a jet flow. Wastage rate of the pipe is

provided in Figure 6.5. The blue color shows that the wastage rate of the pipe is below 2 mm/year, and the orange color shows that this value is over 2 mm/y. Impingement speed required to erode pipe over 2 mm/year is plotted for aluminum, brass and stainless steel. So, the threshold velocity is 30 m/s for Aluminum, 40 m/s for brass and 45 m/s for stainless steel. This observation is clearly not in agreement with the Baker et al. (1966) study described above.
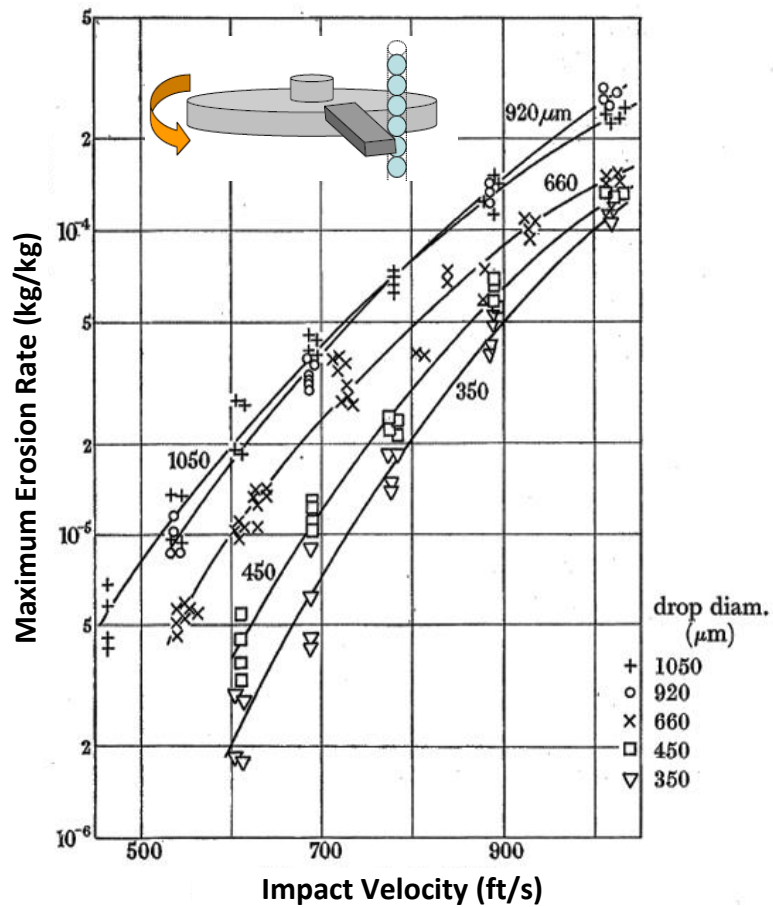
Figure 6.4 Maximum erosion rate vs. impact velocity (Baker et al. 1966)
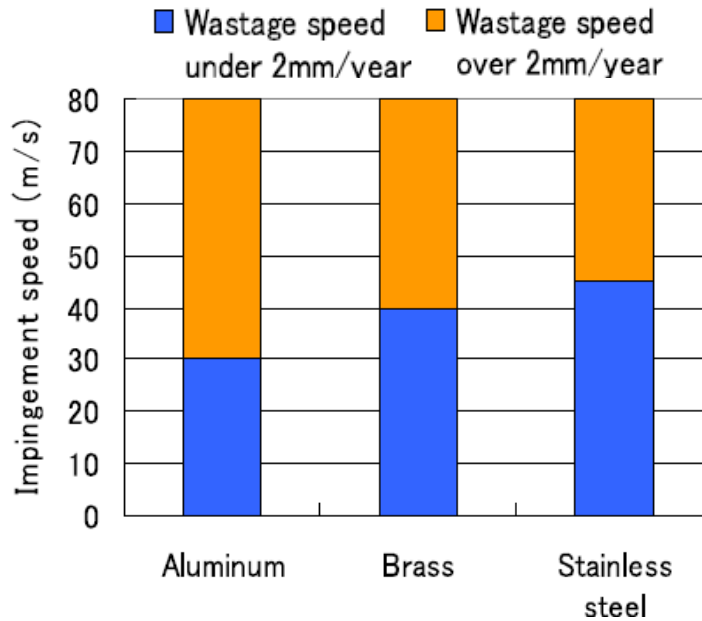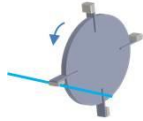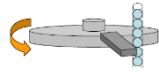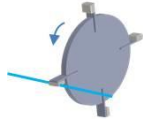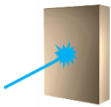
Figure 6.5 Wastage speed of the pipe (Higashi et al. 2009)

Hattori (2010) measured the maximum depth of erosion for three materials: S15C or carbon steel, stainless steel 304, and STPA24 which is an alloy steel used for pipes. He used a fixed specimen configuration and accelerated the water jet toward the specimen. The maximum depth of erosion was measured during exposure time for carbon steel. The threshold velocity in which no measurable erosion would take place is 80 m/s for carbon steel and 120 m/s for stainless steel 304.

The results of the experiments reviewed so far are summarized in Table 6.1. The experiment could be a paddle wheel type with continuous jet or a droplet stream or a nozzle jet type. Different materials have been used in these experiments but some of them are similar. It can be seen that the results provided by these different types of experiments vary significantly.

Table 6.1 Experimental studies in the literature

No.	Reference	Exp. Type	Material	Velocity (m/s)	(ft/s)	Erosion
1	Thiruvengadam et. al. (1970)	Stream & Paddle Wheel	Aluminum	15	50	Threshold Velocities
			SS-316	46	150	
2	Baker et. al. (1966)	Droplet & Paddle Wheel	H.S.S.	120	390	Threshold Velocity
3	Higashi et. al. (2009)	Stream & Paddle Wheel	Aluminum	30	98	2 mm/y (78 mpy)
			Brass	40	131	
			SS-304	45	147	
4	Hattori (2010)	Nozzle Jet	S15C	80	260	Threshold Velocities
			STPA 24	90	295	
			SS-304	120	393	

A set of proprietary experiments were conducted at the University of Tulsa in 1994 by Professor Shadley (Shadley 1994). The "liquid jet and paddle wheel" erosion apparatus used a design that conforms to the American Society for Testing and Materials Standard G73-10 (ASTM 2010). The test specimens were mounted on a rotating paddle wheel by means of special mounting brackets (Figure 6.2-a). The wheel turns at a constant rotational speed, and a jet of fluid is directed transverse to the plane of rotation so that the specimens impact the fluid jet. The angular velocity of the wheel dominates the impact velocity. The specimens are slightly tilted so that the impact angle is 90°. Figure 6.6 shows how this angle produces a normal impact of resultant velocity. Nine materials were evaluated in this program. Mechanical properties and chemical

composition of materials tested are shown in Table 6.2 and Table 6.3, respectively.
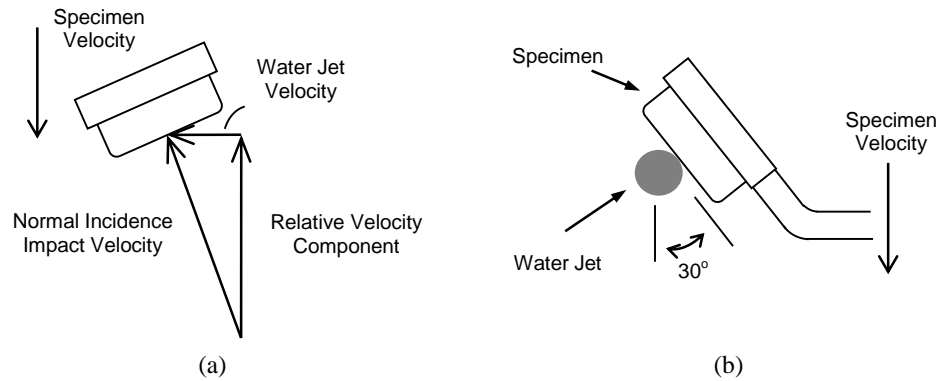
Figure 6.6 (a) Specimen jet normal incidence, (b) 30° impact angle

Table 6.2 Mechanical properties of tested materials

Alloy	UNS no.	Tensile strength, ksi	Yield strength, ksi	Hardness Brinell
9Cr-1Mo	K90941	95 *	68 *	214 *
CS-1018	G10180	99.5	90	210
13 Cr-A	S42000	105.1	61.4	200
13 Cr-H	S42000	92.7	76.5	197
SS-316	S31603	85	35	210
Sm25-Cr	S31260	130 *	125 *	337 *
2205 duplex	S31803	90 *	65 *	293 *
Inc 625	N06625	120 *	60 *	200 *
Inc 825	N08825	96 *	49 *	200 *

* approximate value

Table 6.3 Chemical composition of tested materials in wt% (balance Fe)

Alloy (UNS no.)	C	Si	Mn	Cu	Ni	Cr	Mo
9Cr-1Mo (K90941)	0.1	0.5	0.4	0.0	0.0	9.3	1.0
CS-1018 (G10180)	17.0	0.0	0.8	0.0	0.0	0.0	0.0
13 Cr-A (S42000) 13 Cr-H (S42000)	0.2	0.6	0.6	0.0	0.0	13.0	0.0
SS-316 (S31603)	0.0	0.3	1.0	0.0	12.0	17.0	2.5
Sm25-Cr (S31260)	0.0	0.7	1.0	0.5	6.5	25.0	3.0
2205 duplex (S31803)	0.0	1.0	2.0	0.0	5.5	22.0	3.0
Inc 625 (N06625)	0.1	0.5	0.5	0.0	58.0	21.5	9.0
Inc 825 (N08825)	0.0	0.5	1.0	2.2	42.0	21.5	3.0

Materials were cut into cylindrical specimens approximately 0.75 inches in diameter and 0.25 inches thick. Actual dimensions varied somewhat depending on the dimensions of the material from which the specimens were cut. Specimens were mounted on a wheel as depicted in Figure 6.2, and electrically insulated from any other conductive parts. The wheel was turned at a constant rotational speed by an A.C. induction motor. A jet of the test fluid was directed transverse to the plane of rotation so that as the wheel rotated, the specimens would impact the fluid jet, the higher the wheel rotation speed, the higher the impact velocity. In some tests, the specimens were aligned so that the impact angle would be 90°, i.e., normal incidence. This is shown in Figure 6.6-a. At the higher wheel rotation rate used (3510 rpm), the velocity of the specimen as it impacted the test fluid jet was 167 ft/s (51 m/s). The velocity of the liquid jet was selected to be a minimum of 34 ft/s (10 m/s). Figure 6.6-a shows how adding these two velocity vectors gives a resultant impact velocity of 170 ft/s (52 m/s) at an angle of 11.5°. To produce normal incidence, the specimen was tilted 11.5°. To achieve 30° impact, the

specimen was rotated about another axis. Figure 6.6-b shows the 30° impact angle produced by rotating the specimen. In this figure, the water jet is directed into the plane of the figure. Two test solutions were used: 1) aerated 3% NaCl brine and 2) aerated tap water. Two impact speeds were used: 1) 170.0 ft/s (high velocity) and 2) 84.6 ft/s (low velocity). Two impact angles were used: 1) 90° (normal incidence) and 2) 30°. Four specimens were tested in each test run except for 1018; the specimens tested in each test run were mixed, i.e., not all specimens on the wheel at one time were the same material. The 1018 specimens were all run together because they deteriorated much more rapidly than the other materials. If a 1018 specimen were run with non-deteriorating materials, it was feared the wheel could become too unbalanced during a test and destroy the machine's bearings. High velocity tests were run nominally 72 hours. Low velocity tests were run 144 hours to approximately achieve the same number of impacts as the high velocity tests. Specimens of 1018 were only run 16 hours because they deteriorated so rapidly. Adjustments were made in the graphed data to scale weight losses to 144 hour test periods.

Weight loss for each test was recorded, and the results were averaged for the tests where more than one specimen was tested. In order to facilitate direct comparison between different tests, the weight losses that are shown Figure 6.7 are adjusted to a 144 hour test period by assuming that weight loss rates observed in the testing periods would have continued to the 144th hour. The tests were repeated with high velocity brine and water for all materials and with other fluids only for carbon steel 1018. The associated standard error bars are provided in Figure 6.7. It can be concluded generally from the chart that brine caused more weight loss than tap water, and 1018 carbon steel had the

80

highest weight loss while Inconel 625 had the lowest.

In the high velocity brine test, the four materials of lowest chromium content were ranked pretty much as one would expect. However, weight losses in the corrosion resistant alloys were surprisingly high. In some specimens of these materials, chunks of material appeared to be broken out of the specimens more in the manner of erosion than of corrosion. The tests were proceeded with the high velocity tap water test assuming that corrosion losses should be lower for this test, at least for the 1018 and low-chrome materials. Figure 6.7 also compares the weight losses between brine tests and tap water tests for the carbon steel and low-chrome materials. Weight losses for the tap water tests were significantly lower than for brine tests, especially for the 1018 and 9Cr-lMo materials. But, weight losses for the tap water tests for some of the corrosion resistant alloys were higher than weight losses for the brine tests.
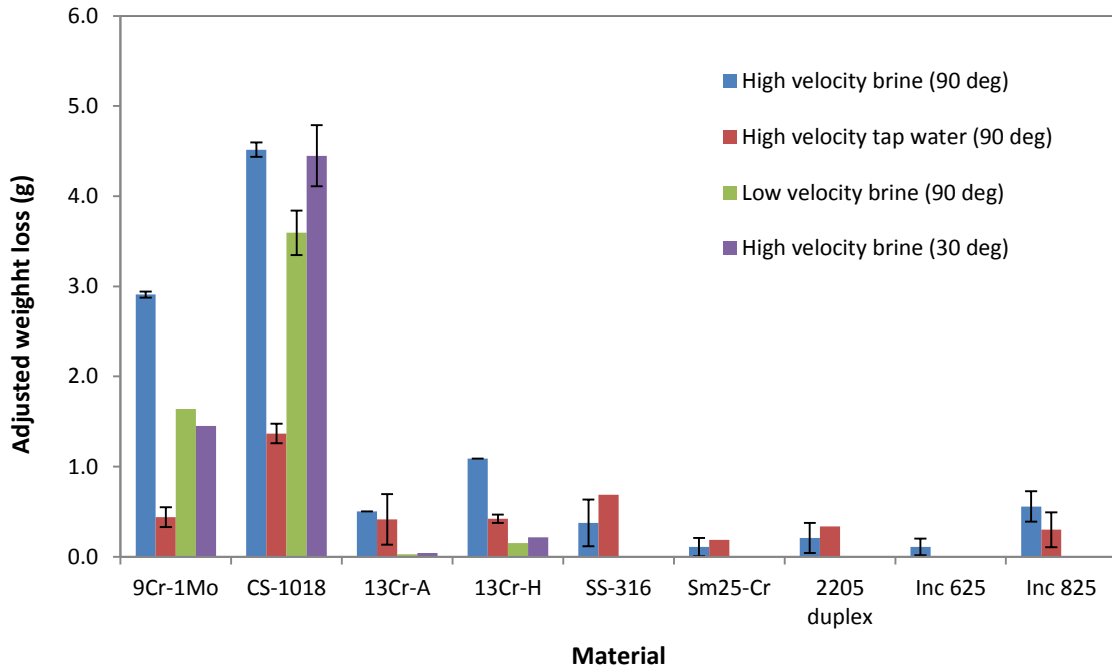
Figure 6.7 Adjusted mass loss of the specimens to 144 hrs

6.3 Erosion Modeling

The adjusted mass loss is not a good parameter to compare erosion/corrosion conditions of the samples at different condition because it does not account for the number of impacts of the fluid jet on the specimen, i.e. the total amount of the liquid that impinged the surface. The volumetric erosion/corrosion ratio (ECR) is defined as the ratio of volume loss of the target material to the volume of the impinged jet.

$$ECR = \frac{\text{Volumetric loss}}{\text{Impinged liquid volume}} \tag{6.1}$$

Figure 6.8 shows ECR of the samples tested with high velocity brine and tap water versus their chromium contents. As one would expect, the ECR is higher for materials with lower chromium content than corrosion resistance alloys especially when brine is used as the jet fluid and the effect of jet fluid was significant. This observation reinforces the hypothesis that the weight losses for the corrosion resistant materials were primarily due to erosion and not corrosion.
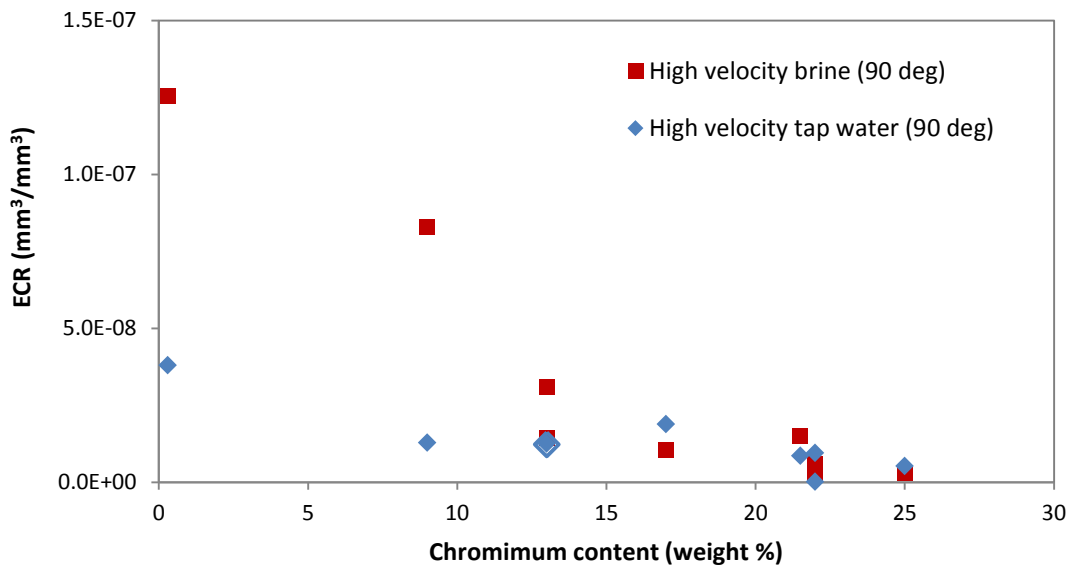
Figure 6.8 ECR versus chromium content of the samples for brine and tap water

Figure 6.9 provides results for all nine materials for high velocity and low velocity brine impacting at 90°. It appears that material degradation for 1018 carbon steel and low-chrome specimens may be controlled by corrosion or a combination of erosion and corrosion, whereas for corrosion resistant alloys, erosion is the mechanism of degradation, and it became negligible when impact velocity was reduced. For the two 13Cr materials, the ECR was reduced by the decrease in impact velocity, and as shown in Figure 6.8, the ECR value was less for water tests than brine. The reason for high ECR values for brine in comparison to water is the effect of electrolyte conductivity on corrosion rate. Oxygen corrosion rate increases by increasing salt concentration up to about 5% because salt increases the conductivity of the solution. However, increasing salt concentration more than 5% will reduce the corrosion rate because it will reduce the solubility of oxygen in water. So, it might be hypothesized that there are significant corrosion and erosion components in the high velocity tests. In liquid impact erosion, it is believed that repeated impacts fatigue the metal and produce sub-surface cracks if the impact velocity exceeds the threshold velocity. When cracks propagate and then intersect, pieces of the fatigued material fall out.

A higher synergistic effect at higher flow velocities can be also explained by faster removal of corrosion products from the surface. Iron oxide forms on the surface as a result of oxygen corrosion. Liquid at higher velocities (i.e. with higher erosivity) removes the corrosion products from the surface faster and creates an active carbon steel surface without corrosion products that can be corroded faster in comparison to a carbon steel surface covered with iron oxide.
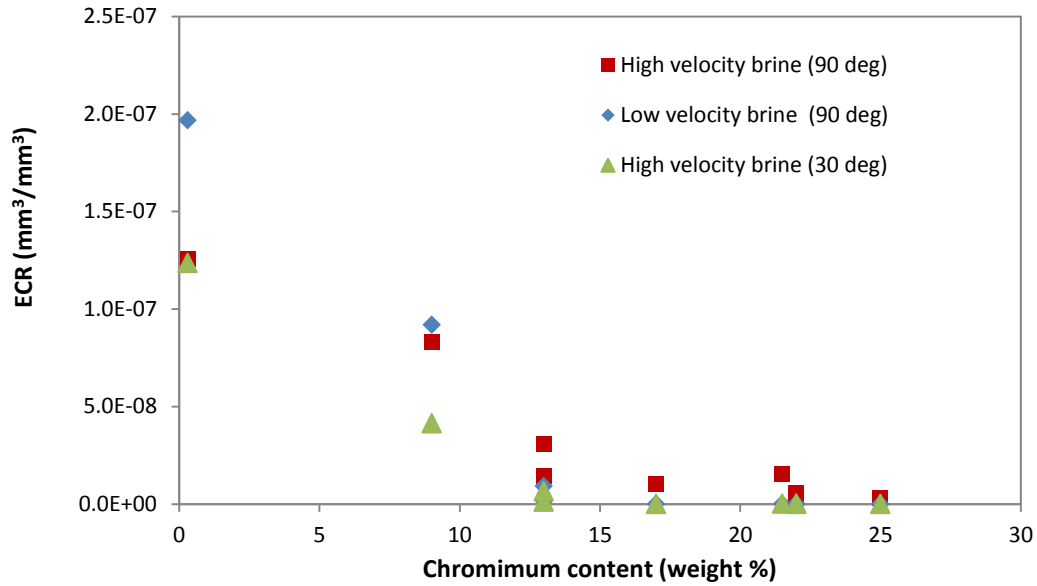
Figure 6.9 ECR versus chromium content of the samples for brine

For the tests at high velocity but with reduced impact angle to 30° (Figure 6.9), ECR values for 1018 carbon steel and 9Cr-1Mo were of the order of losses observed for the high velocity normal incidence test; but for materials of higher chromium content, the 30° test results were much lower than for the 90° tests. This reveals that materials are more susceptible to erosion loss for normal incidence liquid impacts than for smaller angles of incidence. This is an important finding in regard to application to injection wells where liquid impacts the wall at gradual bends at a small angles of incidence.

For materials with high chromium content, weight loss is controlled by erosion. The American Society for Testing and Materials Standard (ASTM) G73-10 proposed a standard method to characterize erosion ratio in different conditions. According to this standard, the maximum erosion ratio is defined as the ratio of material volume loss to the volume of impinged liquid.

$$ER_{Li} = R_e = \left(\frac{V_{loss}}{V_{water}}\right) \qquad (6.2)$$

Also, the incubation period for the number of specific impacts that initiates erosion can be obtained by multiplying the volumetric incubation period by the projected area and then dividing by the volume of a single droplet or jet impinged.

$$N_0 = H_0 \left(\frac{A}{B}\right) \qquad (6.3)$$

where H_0 is incubation period (volume of liquid impinged per unit area), A is projected area and B is volume of a single impacting drop or jet.

For jets, $\quad H_0 = \pi d \frac{N_0}{4}$

For drops, $\quad H_0 = 2d \frac{N_0}{3}$

In each series of experiments, two major parameters determine the erosion resistance of a specified material, erosion resistance number (NER)

$$\log(NER) = \left[\sum_{i=1}^{k} (\log Q_{ei} + \log S_{eri})\right] \Big/ k - \log Q_{ex} \qquad (6.4)$$

and incubation resistance number (NOR)

$$\log(NOR) = \left[\sum_{i=1}^{k} (\log S_{0ri} - \log t_{0i})\right] \Big/ k - \log t_{0x} \qquad (6.5)$$

where, Q_{ex} is maximum erosion rate for test material x, Q_{ei} is maximum erosion rate for reference material i, t_{0x} is nominal incubation period for test material x, t_{0i} is nominal incubation period for reference material i, S_{eri} is reference erosion resistance for reference material I and S_{ori} is reference incubation resistance for reference material i.

The *NER* parameter shows resistivity of the materials against liquid impingement

erosion based on the measured mass loss. If we assume that we have a reference material where the erosion resistance number and incubation resistance are equal to 1, we can calculate the erosion resistance number and incubation resistance number for each material with respect to that reference from these correlations. This technique helps to normalize the erosion resistance of a specific material with respect to a well-known material and eliminate some of the effects of the experimental method. The normalized erosion resistances of several materials that were tested are determined from average values of erosion ratio in the test and are summarized in Table 6.4. The normalized erosion resistance of SS-316 has been used as a reference. It is observed from the table that erosion resistance of Inconel 625 to liquid impact is 5 times greater than the reference material, but the erosion resistance of 1018 to liquid impact erosion-corrosion is about 7 times less than SS-316.

Table 6.4 Normalized erosion resistance (NER) for several oilfield materials

Designation	Normalized Erosion Resistance (NER)
SS-316	1.00
9Cr-1M	0.25
1018	0.15
13Cr-a	0.90
13Cr-h	0.64
Sm25-Cr	3.43
2205	1.83
625	5.19
Sm825	0.96

It is assumed that we have already passed the incubation period which leads to more conservative results. But generally by obtaining the *NER* and *NOR* from experimental data, we could now use

$$\log R_e = 4.8 \log V - \log \text{NER} - 16.65 + 0.67 \log d + 0.57 J - 0.22K \qquad (6.6)$$

and

$$\log N_0 = -4.9 \log V + \log \text{NOR} + 16.40 - 0.40 J \qquad (6.7)$$

to calculate the maximum erosion ratio and incubation period for each material and desired condition, where N_0 is rationalized incubation period, R_e is rationalized maximum erosion rate, *NER* is "erosion resistance number" of material, *NOR* is "incubation resistance number" of material, V is impact velocity in m/s, d is diameter of drops or jet, in mm, J is 0 for drops and 1 for jets and K is 0 for flat specimens at normal impact and 1 for curved or cylindrical specimens.

In order to assess the obtained model, some experimental values of erosion ratio (using a paddle wheel type apparatus) for carbon steel from ASTM STP 474 are compared to model predictions. The results are shown in Figure 6.10. Experimental values represented by markers have been compared to the model predictions represented by dashed lines for four different impact velocities. The vertical axis shows the erosion ratio, and corresponding impact velocities are shown on the horizontal axis. As it can be seen, both models agree well with data, and the red dashed line is slightly closer to the experimental values.
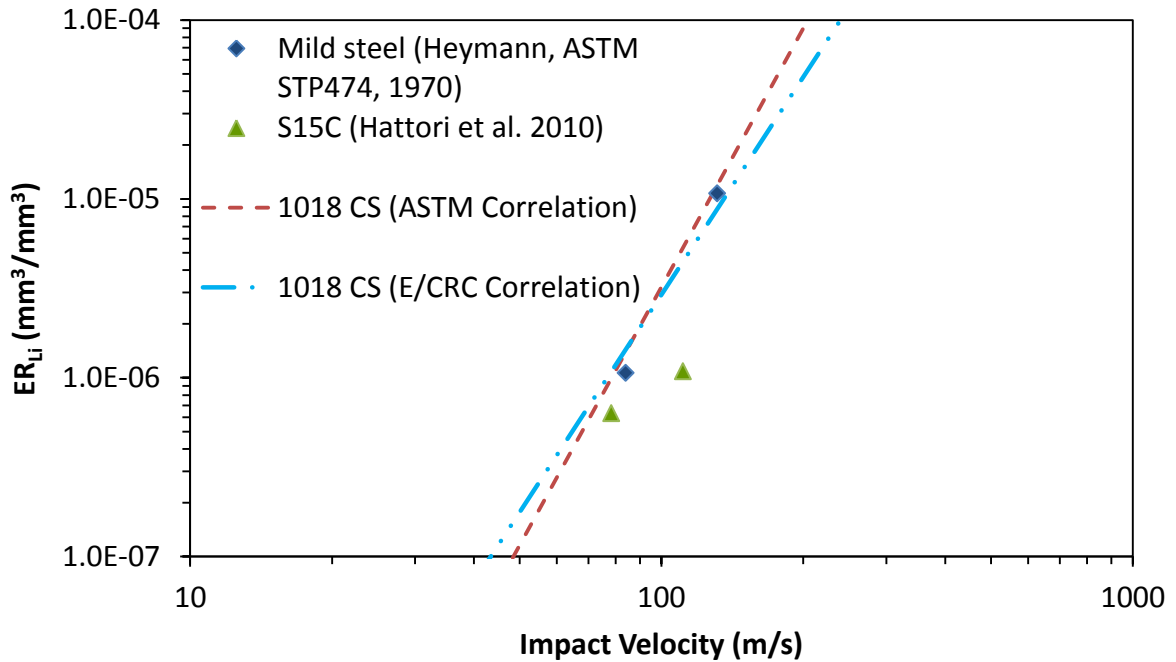
Figure 6.10 Erosion ratio vs. impact velocity

In another experiment from literature, Baker et al. (1966) measured erosion ratio values for chromium steel for a range of droplet sizes (350 μm to 1050 μm). The specimens were mounted on a rotating disk and impacted with liquid droplets. The ASTM G73-10 correlation predictions have also been compared to this experimental data in Figure 6.11. The vertical axis shows volumetric erosion ratios, and the corresponding impact velocities are shown on the horizontal axis. The model predictions closely match experimental measurements for large droplets and overpredict the values for smaller droplets at lower impact velocities.
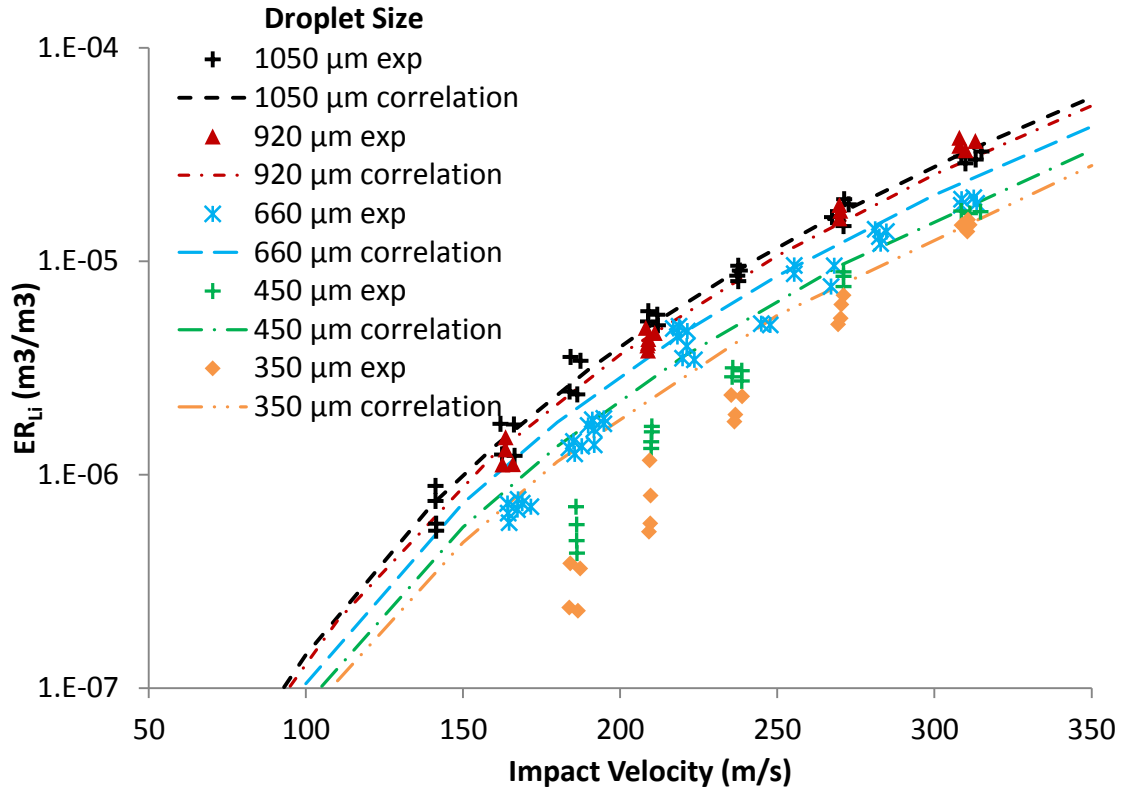
Figure 6.11 Erosion ratio vs. impact velocity (ASTM correlation and exp. data)

The ASTM correlation predictions are good for large droplets (> 1mm), but it overpredicts the erosion ratios for small droplets, especially at lower velocities. Low velocities (less than 100 m/s) are more applicable to the oil and gas industry. So, the correlation has been modified to obtain better predictions at lower velocities and small droplet sizes as shown by Eq. (6.8).

$$ER_{Li} = 10^a \frac{V^{(10-5d^{1/3})} \, d^9}{NER} \quad , \quad a = 0.57 \, J - 0.22 \, K - 17.1 \tag{6.8}$$

In the new correlation, the velocity exponent has been changed from a constant value of 4.8 to a function of droplet size, and the droplet exponent has been raised from 0.67 to 9 as droplet size is also affecting the velocity exponent. The predictions from the modified correlation have been compared to experimental data discussed earlier from the

literature (See Figure 6.10 and Figure 6.12). The ER values are now closer to the experimental data for low velocity cases as compared to ASTM correlation predictions. Since the source of data for model development is data gathered at E/CRC while compared values are from experimental data in the literature, the observed deviation is reasonable.
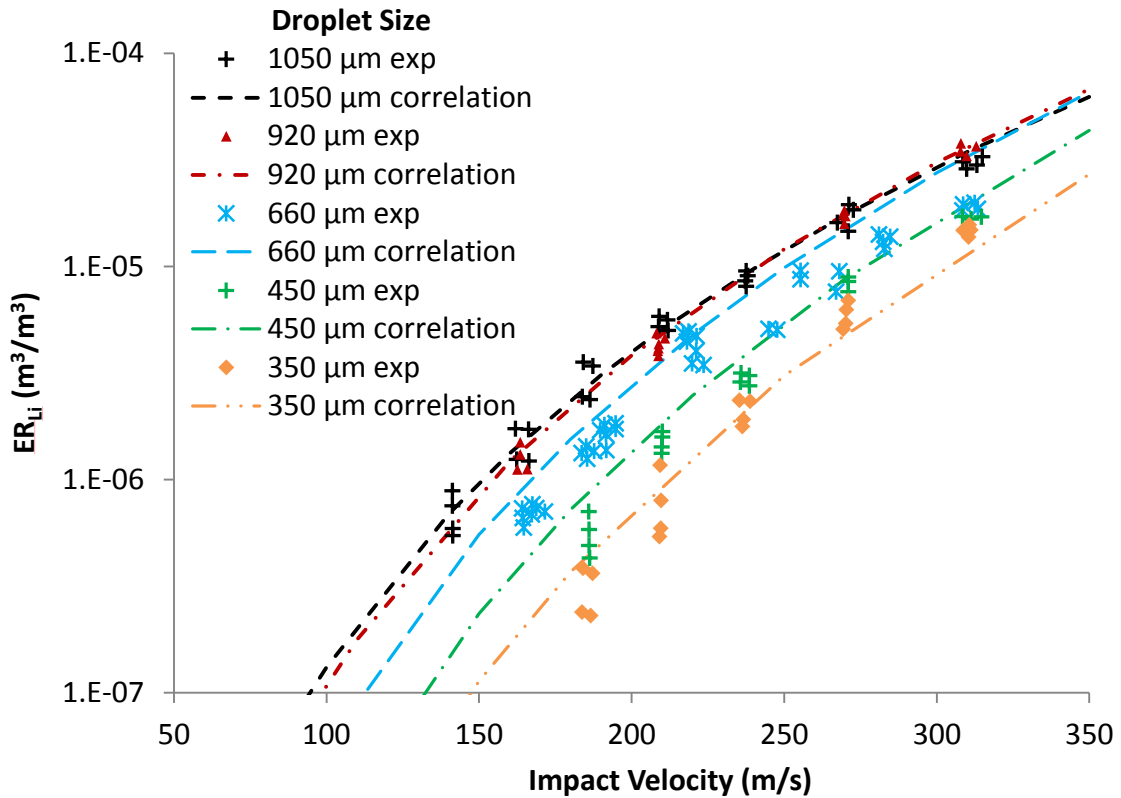
Figure 6.12 Erosion ratio vs. impact velocity (modified correlation and exp. data)

Based on the ASTM standard and liquid jet impingement tests, a correlation is proposed to calculate erosion ratio for liquid impact. But for 1018 carbon steel and 9Cr-1Mo that are not considered corrosion resistant, corrosion is the dominant mechanism of material degradation. In corrosive conditions, the effects of impact speed and angle are not as significant as the effect of chemical composition and oxygen content of the fluid jet. The weight losses of the samples in high velocity normal incidence tests were of the

same order of weight loss as in the low velocity tests. For these materials, corrosion models (based on material properties, oxygen concentration, temperature, viscosity, density, and chemical composition of the fluid) and erosion-corrosion models (based on synergistic effects of erosion and corrosion) should be applied to estimate the wear rate in the pipe.

6.4 Application to Pipe Flow and Threshold Erosional Velocity Calculation

This erosion model can be applied to estimate the erosion rate at a given operating condition or calculate the threshold erosional velocity for a given penetration rate. Erosion rate is a function of impact velocity, droplet size and the amount of liquid droplets or solid particles that impinge the wall in the time unit. So in both cases, whether penetration rate is given and threshold velocity is desired or the other way, it is required to estimate the liquid droplet/solid particle impact velocity, droplet size and entrainment fraction. One way for extracting this information is the numerical simulation of multiphase flow with liquid droplet/solid particle trajectories which requires expertise in computational fluid dynamics (CFD) with a huge computational cost. The alternative is to estimate the average value of entrainment fraction and droplet size from multiphase flow correlations and droplet/particle impact velocity from a stagnation length concept model which has been shown to be acceptable in erosion modeling (McLaury et al. 2000).

A calculation flowchart is provided in Figure 6.13 to apply the model to pipe flow and to calculate thickness loss rate. Required inputs are superficial liquid and gas

velocities, V_{SL} and V_{SG}, diameter of the pipe, D and *NER* introduced earlier. Output is thickness loss rate of the pipe. Entrainment fraction, f_E, and droplet diameter can be calculated from mechanistic models that are presented in the literature. The impact velocity of the liquid droplets can be calculated from the SPPS (Sand Production Pipe Saver) program in the same way that impact velocity of a sand particle in elbows and tees is calculated. But, the model for elbows and tees is applied to droplets entrained in a gas stream and flowing through stagnation layers before they have an opportunity to impact the pipe wall. The "stagnation layers" reducing the speed of liquid droplets are the gas and a possible liquid film that may form at the outer walls of an elbow for certain flow conditions.

Volume loss of the material is obtained by multiplying erosion ratio (from Eq. (6.8)) by the total volume of the droplets impinging the pipe wall in a given area that is assumed to be the projected pipe area. Finally, thickness loss is equal to volumetric loss divided by projected impact area, A_p.
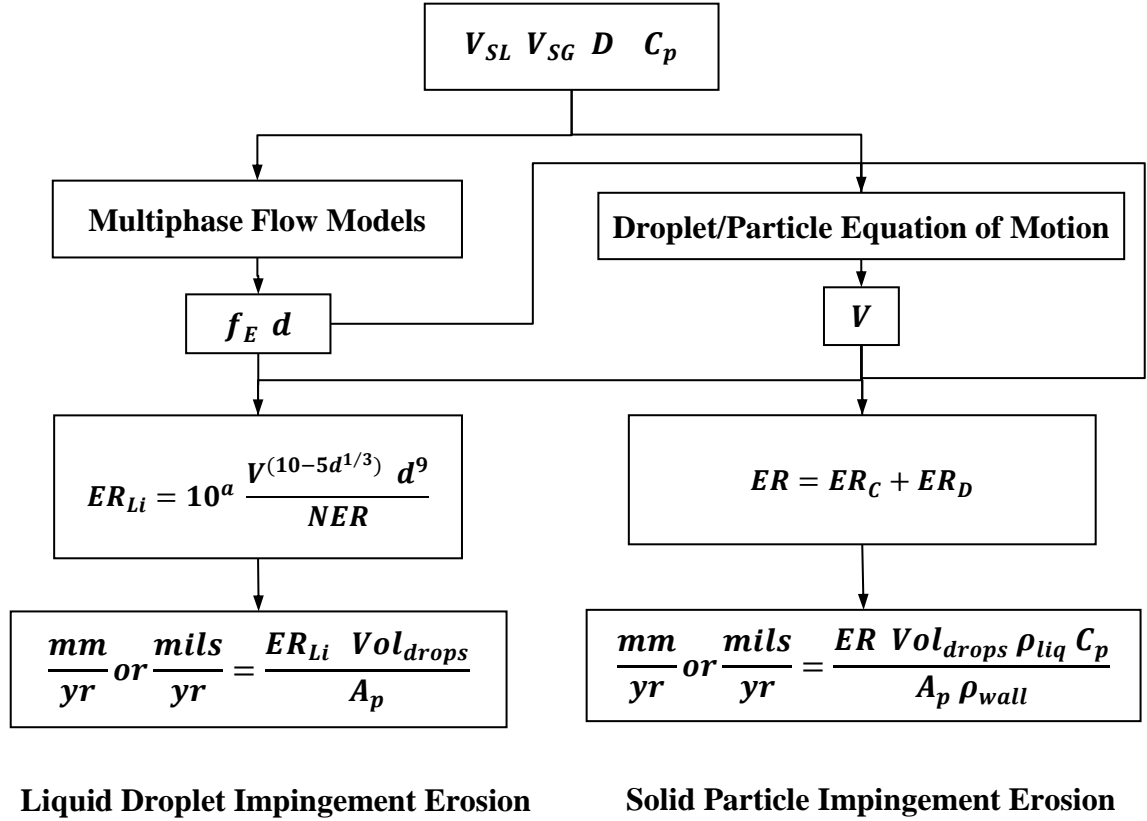
Figure 6.13 Calculation procedure of the penetration rate

due to liquid droplet/solid particle impact

Extensive theoretical and empirical studies have been carried out on the estimation of entrainment fraction and droplet size in two-phase flow systems. For horizontal flows, Pan and Hanratty (2002) proposed the following correlation to calculate entrainment fraction in the pipe.

$$\frac{f_E/f_{Em}}{1 - f_E/f_{Em}} = 9 \times 10^{-8} \left(\frac{D v_G{}^3 \sqrt{\rho_L \rho_G}}{\sigma}\right) \left(\frac{\rho_G{}^{1-m} \mu_G{}^m}{d_{32}{}^{1+m} g \rho_L}\right)^{1/(2-m)} \tag{6.9}$$

Ishii and Mishima (1989) obtained this correlation,

$$f_E = tanh\left(7.25 \times 10^{-7} We^{1.25} Re_{SL}^{0.25}\right) \qquad (6.10)$$

in which

$$We = \frac{\rho_G v_{SG}^2 D}{\sigma} \left(\frac{\rho_L - \rho_G}{\rho_G}\right)^{\frac{1}{3}} \qquad (6.11)$$

to estimate entrainment fraction in vertical flows. The average droplet size can be calculated from the Tatterson et al. (1977) correlation.

$$\left(\frac{\rho_G v_G^2 d_{32}}{\sigma}\right)\left(\frac{d_{32}}{D}\right) = 0.0091 \qquad (6.12)$$

The impact velocity of the liquid droplets can be calculated from models for calculating impact velocity of sand particles in elbows and tees. Studies in the literature have shown that the liquid film along the outer wall of an elbow is sometimes less than what forms in a straight pipe. The droplet impact velocity is obtained by applying the following equation of the motion of a droplet with average size estimated above across the stagnation length,

$$mV_d \frac{dV_d}{dx} = 0.5\rho_f\left(V_f - V_d\right)\left|V_f - V_d\right|C_D \frac{\pi d_d^2}{4} \qquad (6.13)$$

where *m* is mass of droplet, V_d is droplet velocity, ρ_f is fluid density, V_f is fluid velocity, C_D is drag coefficient and d_d is droplet diameter.

The drag coefficient is calculated from the following correlation.

$$C_D = \frac{24}{Re_r} + 0.5 \quad , \quad Re_r = \frac{\rho_f\left|V_f - V_d\right|d_d}{\mu_f} \qquad (6.14)$$

Droplet velocity is unknown in Eq. (6.14) and will be approximated by a one-dimensional particle tracking model. According to Shirazi et al. (1995b), a stagnation

length of L is assumed to be a region near the wall through which the droplet needs to penetrate to reach the wall. The stagnation length depends on flow geometry and is estimated empirically as a function of pipe diameter.

$$\frac{L}{L_0} = 1.35 - 1.32 \, \text{Tan}^{-1}(1.63D^{-2.96}) + D^{0.247} \quad , \quad L_0 = 1.06 \, \text{in} \qquad \text{for Tee} \qquad (6.15)$$

$$\frac{L}{L_0} = 1.00 - 1.27 \, \text{Tan}^{-1}(1.01D^{-1.89}) + D^{0.129} \quad , \quad L_0 = 1.18 \, \text{in} \qquad \text{for Elbow} \qquad (6.16)$$

In the stagnation zone, it assumed that the fluid velocity decrease linearly from V_0 to zero at wall as shown in Figure 6.14.

$$V_f = V_0 \left[1 - \frac{x}{L} \right] \tag{6.17}$$
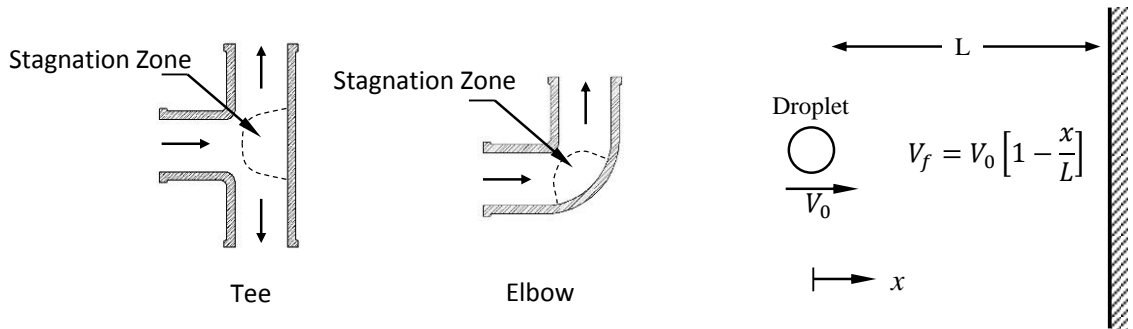
Figure 6.14 Stagnation length for tee and elbow

After substituting for entrainment fraction, droplet size and impact velocity in the erosion ratio equation for liquid impact, volumetric loss rate of the material is obtained by multiplying the erosion ratio (from Eq. (6.8)) by the total volume of the droplets impinging the pipe wall in a given area that is assumed to be the projected pipe area. Finally, thickness loss is equal to volumetric loss divided by projected impact area, A_p.

For droplets containing small particles there is an extra step in calculating impact

95

velocity. After the droplet impacts the wall, the particles need to penetrate through the liquid layer formed on the wall to impact the wall. ANSYS Fluent is used to study relative motion of the particles with respect to liquid when it is spreading out on the wall. It is assumed that the droplet and particle have the same initial velocity, and particles are distributed uniformly in the droplet. Figure 6.15-a shows a sequence of a droplet with particles inside during impact. Although particle impact velocity can be estimated from CFD simulation, it is not feasible to run simulations for each droplet size and velocity. So, the stagnation length concept can be used again by assuming that the representative particle is located at the center of the droplet and needs to penetrate through the liquid stagnation length equal to the radius of the droplet to reach the wall. This simplification is demonstrated in Figure 6.15-b. The next step is to substitute for wall material hardness, particle sharpness factor and particle impact velocity to calculate erosion ratio for solid particles. Finally, the penetration rate is equal to the erosion ratio multiplied by impinging particle mass divided by the density of wall material and impact projected area. Compared to liquid impingement erosion, the wall material density appears in the solid particle erosion calculation because the erosion ratio equation for liquid is mostly expressed in volumetric loss per volume of impinged liquid (e.g. m^3/m^3), but the unit of the erosion ratio equation for solid particles is mass loss per mass of impinging particles (e.g. kg/kg).

(a)

Droplet   Entrained
           Particles

(b)

Droplet

     Representative
       Particle

L
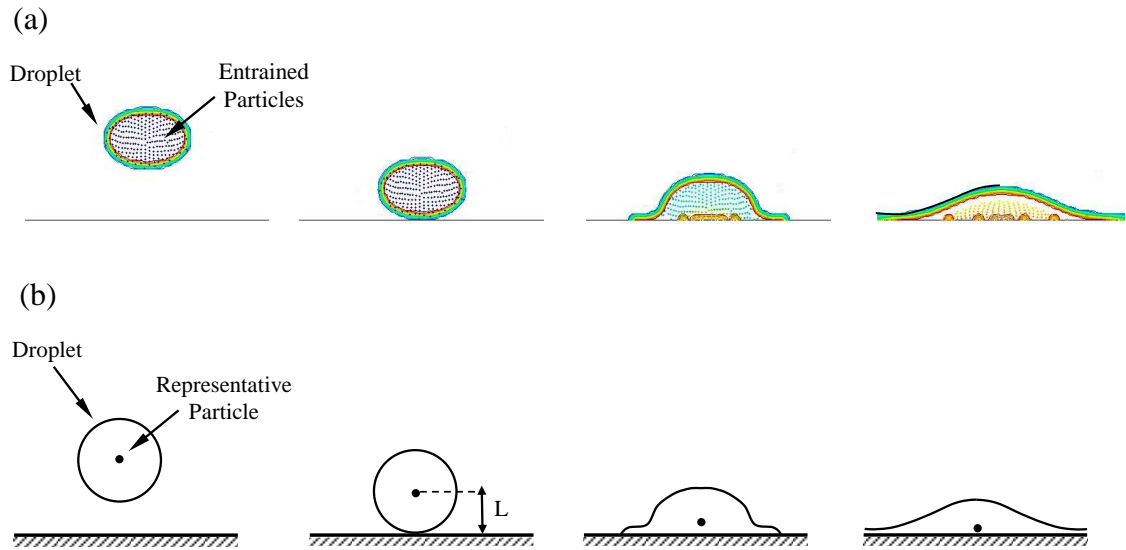
Figure 6.15 Sequence of simulated droplet and particle impingement and corresponding simplified model

The new calculation procedure can be applied in two ways: calculation of penetration rate for a given flow condition or calculation of threshold erosional velocity given allowable penetration rate. The second case will be described to compare the current model predictions to erosional velocities calculated from the API RP 14E correlation.

Figure 6.16 shows threshold velocity calculations for erosion caused by droplets with and without particles using the Sand Pipe Saver Program (SPPS) (Shirazi et al. 2000) developed at the E/CRC presented previously compared to predicted values by the API RP 14E correlation. These calculations have been carried out for an elbow geometry in a 4-inch (102 mm) pipe. Calculation for a tee joint and other pipe sizes can be easily done using the stagnation length correlations. The erosional velocity is assumed to be the velocity at which the erosion rate is 5 mpy (0.13 mm/yr). In these calculations, a sand size of approximately 25 microns is used which represents impurities or background sand

in the liquid with density of 2650 kg/m^3 and production rate of 10 lb/day. The solid line is the threshold boundary for droplets containing particles which yield 5 mpy (0.13 mm/yr). It follows the trend of SPPS predictions represented by the dash-dot line which is based on the semi-empirical particle tracking in single and multiphase flows with the same particles and behaves very differently than the API RP 14E correlation predictions (dash line). The API RP 14E does not account for solid particle behavior in liquid. In this correlation, the only parameter that changes with the presence of solid particles in liquid is the empirical constant *C* which is 100 for continuous service and 150 to 200 for solids-free with suppressed corrosion. The threshold line for pure liquid droplet impact (dash-double dot line) shows relatively high gas velocities. It is observed in the calculation that as gas velocity increases, droplet size decreases. Small droplets can hardly pass through the stagnation zone because of their small inertia followed by low impact velocity and low induced erosion. So, increase in gas velocity increases droplet initial velocity but decreases impact velocity. Here, it is assumed that droplet size is not reduced below 30 μm to calculate conservative results to compare with other cases, so the actual erosion may be even less than what is presented in Figure 6.16.
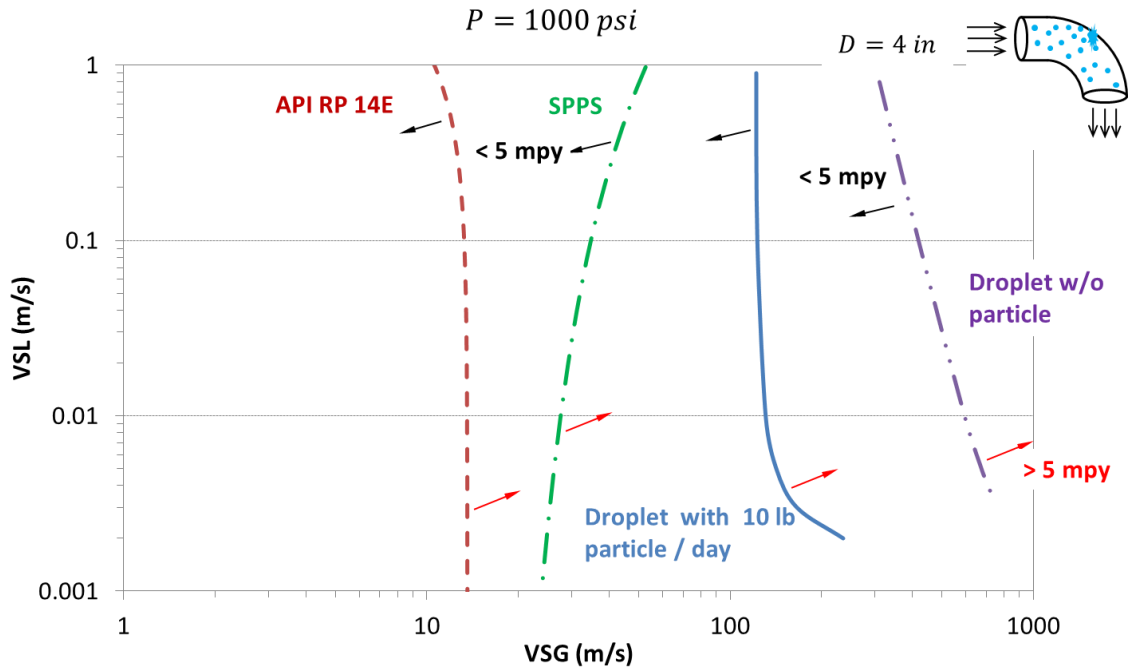
Figure 6.16 Comparison of predicted threshold erosional velocity

In another comparison, variations of erosional velocity versus operating pressure calculated from the API RP 14E correlation and the method and correlation developed in this work are plotted in Figure 6.17. A tolerable erosion-corrosion rate of 5 mpy (0.13 mm/yr) is assumed, and the operational flow conditions are back-calculated. For these comparisons, superficial liquid velocity is assumed to be 0.09 m/s, and mean size of the droplets is assumed to be 200 μm. The constant size of droplets will result in conservative values for erosional velocity because in real conditions, droplet size decreases with increase in gas velocity. Erosional velocity is shown on the vertical axis and operating pressure on the horizontal axis. The model predicts that for higher gas pressures that are normally encountered in gas producing wells, the droplets are slowed as the gas density increases and reduces the droplet impact velocity. Thus, the threshold velocity for liquid droplet impact erosion and erosion caused by solid particles inside the

droplet should increase as the pressure is increased. However, the results indicate that API RP 14E does not follow the trend predicted by the present model. The erosional velocity predicted by API RP 14 E decreases with gas pressure because the mixture density increases and erosional velocity is proportional to the inverse of the square root of mixture density.
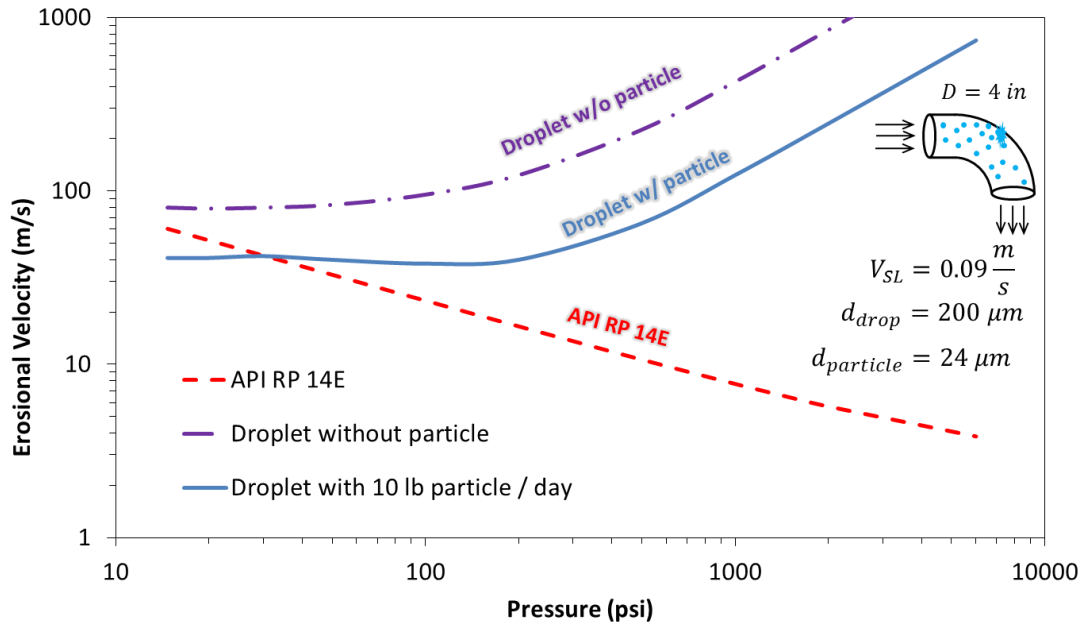
Figure 6.17 Variation of erosional velocity versus operating pressure

The behavior of different materials in erosive conditions has been discussed, but in corrosive conditions, the material behavior is different. Generally, corrosion is accelerated by increasing the fluid velocity which intensifies the mass transport rate and also corrosion product scale removal. Lu (2013) discussed that the dependence of erosion/corrosion rate on impact velocity is

$$\frac{mm}{yr} = const. V^{\beta} \qquad (6.18)$$

in which V is the liquid impact velocity in m/s, and the β value depends on the relative

contributions of corrosion and erosion to total loss, and it is 0.8 to 1 when corrosion is the rate controlling process for liquid impacts and 5 to 8 for liquid droplet impingement in high speed gas flow. The thickness loss rate for liquid impingement erosion is found to be

$$\frac{mm}{yr} = \frac{ER_{Li} \, V_{SL} \, A}{A_p} \approx ER_{Li} \, V_{SL} = Const.\frac{V^{\beta} \, d^{\alpha}}{NER} V_{SL} \qquad (6.18)$$

where ER_{Li} is erosion ratio due to liquid impact, V_{SL} is superficial liquid velocity, A is the pipe cross-sectional area, A_p is the projected impact area, V is liquid impact velocity, d is the droplet diameter and NER is the normalized erosion resistance of the target material that is obtained from experiments. For high speed liquid droplet impact, the ER_{Li} is a function of impact velocity and droplet diameter, but at low impact velocities and especially for low chromium alloys, corrosion rate is much higher than erosion rate. So, the erosion/corrosion ratio (ECR) does not change significantly with impact velocity (see Figure 6.9). The thickness loss rate may be estimated from

$$\frac{mm}{yr} \approx ECR.V_{SL} = Const.V_{SL} \qquad (6.19)$$

The form of this correlation is consistent with the empirical correlation provided by Lotz (1990). This model has been used to calculate the threshold velocity for an elbow geometry (made of stainless steel 316 and carbon steel 1018) in a pipe flow system by assuming a tolerable erosion-corrosion rate of 0.13 mm/yr (5 mpy) and back-calculating the operational flow velocity. The results are compared to the API RP 14E correlation in Figure 6.18. The threshold velocity due to erosion is a function of superficial gas and liquid velocities which determine the rate of liquid impact and impact velocity respectively, but in the corrosive condition and at superficial gas velocities more than 50 m/s the flow is annular and droplets are moving at similar speeds as the gas velocity. So,

they can remove the corrosion scales from the surface, and the liquid flow rate determines the wastage rate of the pipe. The corrosion line is based on the tests with tap water as the ECR value for 1018 carbon steel with brine is so high that the calculated threshold liquid rate is below the minimum value on this figure.
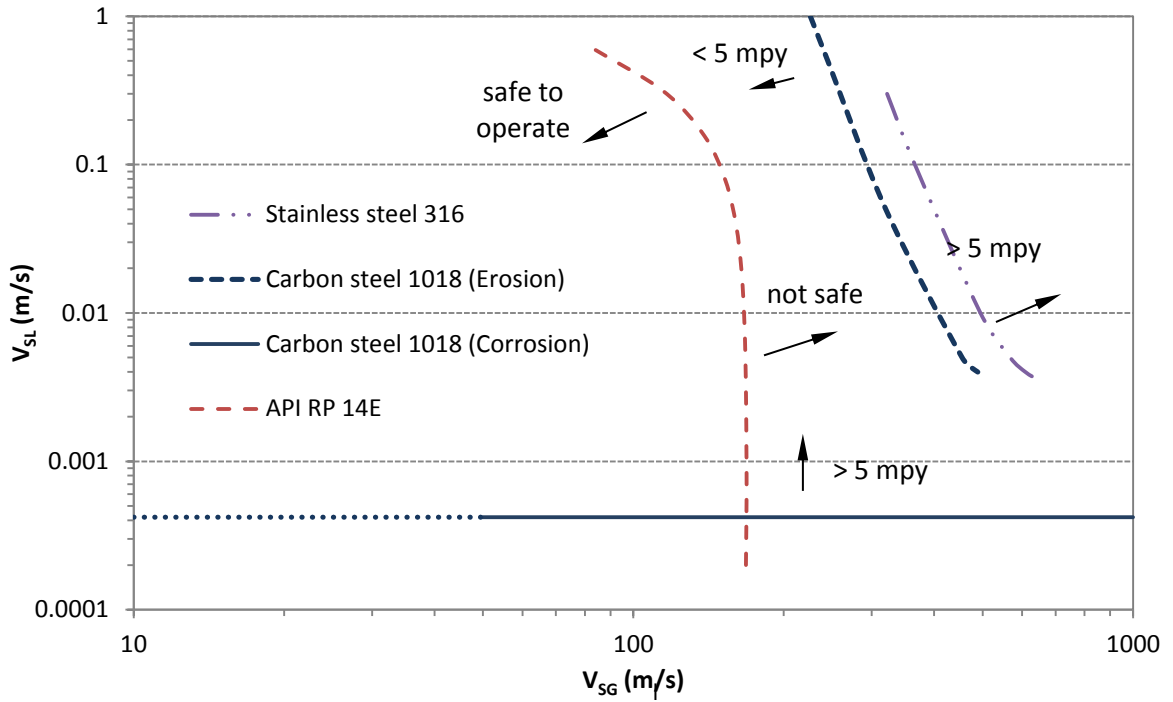
Figure 6.18 Comparison of predicted threshold erosional velocity

CHAPTER 7

SUMMARY AND CONCLUSIONS

A unified erosion equation has been developed based on some of the studies in the

literature to calculate the erosion of various metallic samples. The equation is composed

of two parts, cutting erosion that is related to cutting into the surface target material by

striking particles at grazing impact angles and deformation erosion which is caused by

platelet formation and surface failure as a result of multiple collisions of particles in the

normal direction. The distinction of erosion mechanisms for normal and tilted angle

impacts is supported by SEM images of the sample surface as a rough indented surface is

observed at locations where particles impact the surface normally and long craters are

found at locations where particles hit the target at grazing angles.

The model accounts for the particle shape and size and has been validated with

experimental data from direct impingement testing. The particle velocities in gas have

been measured using particle image velocimeter (PIV), and empirical constants have

been incorporated into the final erosion equation based on the experimental data. It was

concluded from experimental data that velocity exponent may be increased from 2 that is

obtained from the formulation to 2.41. Fair agreement has been observed between the

experimental data and model predictions for various samples at different impact

conditions. It was also found that most of the empirical constants follow a trend and can

be correlated to the mechanical properties of the materials indicating that the equations

are capturing the physics of the problem. Also the effects of particle size on the

deformation erosion threshold velocity and particle sharpness on erosion were justified physically. The new equation can be used in CFD simulations and particle tracking codes to calculate erosion damage for different geometries and materials.

Erosive behavior of very fine particles (iron powder, calcite, barite, hematite, magnetite, silica flour, alumina and silicon carbide) entrained in liquid has been studied in two experimental configurations, submerged and mist flow. Particle concentration was 1% by mass and particles were scanned by SEM to characterize representative size distribution, shape and angularity. PIV was used to measure the velocity of liquid droplets containing particles, and CFD simulations were performed to estimate the impact velocity of particles that are entrained by droplets in air/water mist flow or by the liquid jet spreading over the wall in the submerged case.

Mass loss of a specimen is measured after 72 hours of nonstop testing and converted to erosion ratio which is defined as the ratio of mass loss of the specimen to mass of erodent throughput. The results indicate that the induced erosion (mass loss) of the target specimen is not only a function of particle hardness, but other parameters such as particle impact kinetic energy and angularity also contribute. So, the erosion ratio values obtained from the two test configurations were divided by the estimated particle impact velocity squared and particle angularity to find the erodent hardness dependency of the erosion. The hardness effect was found to be remarkable when the hardness of the particle is less than the hardness of target material, and erosion ratio was found to not increase significantly when the particle hardness is higher than the material hardness and the particle keeps its integrity during impact.

A calculation guideline has been developed based on experimental results and simplified particle tracking models in the literature to predict erosion rate and threshold velocities due to the impingement of liquid droplets with or without small particles entrained. For liquid droplet erosion, the original ASTM G73-10 erosion ratio equation has been modified to predict better results especially for small droplets at low impact velocities which are more applicable to oil and gas industry production and transportation facilities. The erosion ratio of solid particles is calculated from the erosion equations available in the literature developed based on direct impingement testing with gas.

Entrainment fraction and droplet size in gas-liquid flow in the pipe are estimated with correlations in the literature. In order to estimate liquid droplet or solid particle impact velocity, it is assumed that droplets enter a stagnation zone near the wall in which the fluid velocity decreases linearly from the main stream velocity to zero. For solid particles, CFD simulations showed that when a droplet spreads over the wall, particles penetrate into the liquid film formed by the droplet impact and hit the wall. The stagnation length concept is used again but this time inside the liquid droplet to estimate impact velocity of a representative particle located initially at the center of the droplet. By knowing impact condition, one can calculate the erosion ratio either for droplets or entrained particles from erosion ratio equations. Penetration rate is calculated from the amount of liquid droplets or solid particles that impinge the wall multiplied by the erosion ratio. This procedure is implemented to predict threshold erosional velocity for a sample case and results are compared to API RP 14E and SPPS predicted values. It was found that the API correlation under estimated the threshold velocity for liquid impingement erosion and did not correlate with the limitation imposed by particles

entrained in liquid droplets, but SPPS predictions that are calculated from another mechanistic approach for multiphase flows showed similar trends with results obtained from this guideline. The comparisons also have been made over a range of operating pressures (from atmospheric pressure to 10000 psi). The API RP 14E predictions do not follow the trend of calculated values from the present model; it under-predicts the threshold velocity especially for high pressures. The erosional velocity in the API equation changes adversely with the fluid mixture density. In this formula, when pressure increases the density of the mixture increases that leads to lower erosional velocities, but in the present model and calculation procedure, as pressure increases, the density of the gas increases so it can decelerate the droplets (with or without particles) that impact the pipe wall so erosional velocity increases.

CHAPTER 8

RECOMMENDATIONS

Erodent particle properties are very important in the calculation of erosion. So, it is proposed to investigate the effect of particle size, shape and hardness on the erosion of other materials than presented here and study the erosion angle dependency on particle sharpness. The minimum impact angle in these tests was 15 degrees, and this was due to the limitation in the experimental apparatus. So, it would be interesting to conduct some experiments at lower impact angles and compare the results with the present study. One of the main applications of the developed erosion equation would be implementation in CFD codes (such as Fluent) and other erosion models, and it is recommended to use the erosion equations in the simulation and compare the results to the experimental data for different geometries and flow conditions.

A calculation guideline is proposed to estimate the erosion-corrosion caused by liquid impacts and the application includes but is not limited to production, process, and transportation facilities in petroleum, power plant and aerospace industries. Liquid impact erosion-corrosion is of great importance from both economical and safety aspects and in order to obtain more accurate results it is suggested to investigate the problem further and study the synergistic effect of erosion-corrosion in different materials and using other fluids (especially CO_2 which is very frequently found in the oil and gas industry).

BIBLIOGRAPHY

Akbarzadeh, E., Elsaadawy, E., Sherik, A.M., Spelt, J.K., Papini, M., 2012, "The Solid Particle Erosion of 12 Metals using Magnetite Erodent," Wear, Vol. 282, pp. 40-51.

API, 1991, API Recommended Practice for Design and Installation of Offshore Production Platform Piping Systems, API RP 14E, American Petroleum Institute, the 5th Edition. Washington D.C., October.

ASTM Standard G73, 2010, "Standard Test Method for Liquid Impingement Erosion Using Rotating Apparatus", ASTM International, West Conshohocken, PA, 2010, DOI: 10.1520/G0073-10 www.astm.org.

Babu, P.S., Basu, B., Sundararajan G., 2011, "The Influence of Erodent Hardness on the Erosion Behavior of Detonation Sprayed WC-12Co Coatings," Wear, Vol. 270, pp. 903-913.

Bahadur, S., Badruddin, R., 1990, "Erodent Particle Characterization and the Effect of Particle Size and Shape on Erosion," Wear, Vol. 138, pp. 189-208.

Baker, D. W. C., Jolliffe, K. H., Pearson, D., 1966, "The Resistance of Materials to Impact Erosion Damage" Philosophical Transactions of the Royal Society of London. Series A, Mathematical and Physical Sciences, Vol. 260, pp. 193-203.

Bingley, M.S., O'Flynn, D.J., 2005, "Examination and comparison of various erosive wear models," Wear, Vol. 258, pp. 511-525.

Bitter, J.G.A., 1963a, "A study of erosion phenomena part I," Wear, Vol. 6, pp. 5-21.

Bitter, J.G.A., 1963b, "A study of erosion phenomena: Part II," Wear, Vol. 6, pp. 169-190.

Bourgoyne, A., 1989, "Experimental Study of Erosion in Diverter Systems Due to Sand Production," Proceedings of SPE/IADC Drilling Conference, New Orleans, LA.

Castle, M. J., Teng, D. T., 1991, "Extending Gas Well Velocity Limits: Problems and Solutions". Proceedings of SPE Asia-Pacific Conference, Perth. Australia

Chein, R., Chung, J. N., 1988, "Particle Dynamics in A Gas-Particle Flow over Normal and Inclined Plates," Chemical engineering science, Vol. 43, pp. 1621-1636.

Chen, Q., Li., D.Y., 2003, "Computer Simulation of Solid Particle Erosion," Wear, Vol. 254, pp. 203-210.

Chen, X., 2004, Application of Computational Fluid Dynamics (CFD) to Single-phase and Multiphase Flow Simulation and Erosion Prediction, Ph.D. Dissertation, Department of Mechanical Engineering , The University of Tulsa

Chen, X., McLaury, B. S., Shirazi, S. A., 2004, "Application and Experimental Validation of a Computational Fluid Dynamics (CFD)-Based Erosion Prediction Model in Elbows and Plugged Tees," Computers & Fluids, Vol. 33, pp. 1251-1272.

Clark, H. M., 1992, "The Influence of the Flow Field in Slurry Erosion," Wear, Vol. 152, pp. 223-240.

Desale, G.R., Gandhi, B.K., Jain, S.C., 2006, "Effect of Erodent Properties on Erosion Wear of Ductile Type Materials," Wear, Vol. 261, pp. 914-921.

Dhar, S., Krajac, T., Ciampini, D., Papini, M., 2005, "Erosion Mechanisms due to Impact of Single Angular Particles," Wear, Vol. 258, pp. 567-579.

Dosanjh, S., Humphrey, J. A., 1985, "The Influence of Turbulence on Erosion by a Particle-Laden Fluid Jet," Wear, Vol. 102, pp. 309-330.

Edwards, J., 2000, <u>Development, Validation and Application of a Three-Dimensional CFD-Based Erosion Prediction Procedure</u>, Ph.D. Dissertation, Department of Mechanical Engineering, The University of Tulsa.

ElTobgy, M.S., Ng, E., Elbestawi, M.A., 2005, "Finite Element Modeling of Erosive Wear," International Journal of Machine Tools and Manufacture, Vol. 45, pp. 1337-1346.

Feng, Z., Ball, A., 1999, "The Erosion of Four Materials using Seven Erodents - Towards an Understanding," Wear, Vol. 233, pp. 674-684.

Finnie, I., 1960, "Erosion of Surfaces by Solid Particles," Wear, Vol. 3, pp. 87-103.

Finnie, I., McFadden, D. H., 1978, "On the Velocity Dependence of the Erosion of Ductile Metals by Solid Particles at Low Angles of Incidence," Wear, Vol. 48, pp. 181-190.

Finnie, I., Wolak, J., Kabil, Y., 1967, "Erosion of Metals by Solid Particles," Journal of Materials, Vol. 2, pp. 682.

Goodwin, J. E., Sage, W., Tilly, G. P., 1969, "Study of Erosion by Solid Particles," Proceedings of the Institution of Mechanical Engineers, Vol. 184, pp. 279-292.

Grant, G., Tabakoff, W., 1973, "An Experimental Investigation of the Erosive Characteristics of 2024 Aluminum Alloy," University of Cincinnati, Department of Aerospace Engineering Tech. Rep. No. 73-37.

Harsha, A.P., Bhaskar, D.K., 2008, "Solid Particle Erosion Behavior of Ferrous and Non-Ferrous Materials and Correlation of Erosion Data with Erosion Models,"

Materials & Design, Vol. 29, pp. 1745-1754.

Hattori, S., 2010, "Effect of Impact Velocity and Droplet Size on Liquid Impingement Erosion," Proceedings of International Symposium on the Ageing Management & Maintenance of Nuclear Power Plants, Vol. 58, pp. 71.

Head, W. J., Harr, M. E., 1970, "The Development of a Model to Predict the Erosion of Materials by Natural Contaminants," Wear, Vol. 15, pp. 1-46.

Higashi, Y., Narabayashi, T., Shimazu, Y., Tsuji, M., Ohmori, S., Mori, M., Tezuka, K., 2009, "Study on Pipe Wastage Mechanism by Liquid Droplet Impingement Erosion," Proceedings of ICAPP, Vol. 9, pp. 10-14.

Huang, C., Chiovelli, S., Minev, P., Luo, J., Nandakumar, K., 2008, "A Comprehensive Phenomenological Model for Erosion of Materials in Jet Flow, Powder Technology, Vol. 187, pp. 273-279.

Humphrey, J. A. C., 1990, "Fundamentals of Fluid Motion in Erosion by Solid Particle Impact," International Journal of Heat and Fluid Flow, Vol. 11, pp. 170-195.

Hutchings, I.M., 1977, "Deformation of Metal Surfaces by the Oblique Impact of Square Plates," International Journal of Mechanical Sciences, Vol. 19, pp. 45-52.

Hutchings, I.M., 1981, "A Model for the Erosion of Metals by Spherical Particles at Normal Incidence," Wear, Vol. 70, pp. 269-281.

Hutchings, I.M., 1993, "Mechanisms of Wear in Powder Technology: A Review," Powder Technology, Vol. 76, pp. 3-13.

Ishii, M., Mishima, K., 1989, "Droplet Entrainment Correlation in Annular Two-Phase Flow," International Journal of Heat and Mass Transfer, Vol. 32, pp. 1835-1846.

J. Shadley, 1994, "Erosion-Corrosion Evaluation of Nine Casing Materials for

Application to Kick Point in Condensate Water Injection Wells," Erosion/Corrosion Research Center Report, Tulsa, OK.

Johnson, R.W. (Ed.), 1998, "Handbook of Fluid Dynamics," CRC Press, Boca Raton, Florida

Laitone, J. A., 1979, "Aerodynamic Effects in the Erosion Process," Wear, Vol. 56, pp. 239-246.

Levin, B.F., Vecchio, K.S., DuPont, J.N., Marder, A.R., 1999, "Modeling Solid-Particle Erosion of Ductile Alloys," Metallurgical and Materials Transactions A, Vol. 30, pp. 1763-1774.

Levy, A.V., 1995, "Solid Particle Erosion and Erosion-Corrosion of Materials," ASM International

Levy, A.V., Chik, P., 1983, "The Effects of Erodent Composition and Shape on the Erosion of Steel," Wear, Vol. 89, pp. 151-162.

Li, D.Y., Chen, Q., Cook, B., 2011, "A Further Simulation Study on the Dual Role of Porosity in Solid-Particle Erosion of Materials," Wear, Vol. 271, pp. 1325-1330.

Liebhard, M., Levy, A., 1991, "The Effect of Erodent Particle Characteristics on the Erosion of Metals," Wear 151, Vol. 1991, 381-390.

Lotz, U., 1990, "Velocity Effects in Flow Induced Corrosion," NACE Corrosion 90, Paper No 27.

Lu, B., 2013, "Erosion-Corrosion in Oil and Gas Production," Research and Reviews in Materials Science and Chemistry, Vol. 2, pp. 19-60.

Mansouri, A., Shirazi, S.A., McLaury, B.S., 2014, "Experimental and Numerical Investigation of the Effect of Viscosity and Particle Size on the Erosion Damage

Caused by Solid Particles," Proceedings of ASME 2014 4th Joint US-European Fluids Engineering Division Summer Meeting, Paper no. 21613, Chicago, IL

McLaury, B., Shirazi, S., Shadley, J., Rybicki, E., 1995, "Parameters Affecting Flow Accelerated Erosion and Erosion-Corrosion," CORROSION 95, Paper No. 120, Houston, NACE International

McLaury, B.S., Shirazi, S.A., 2000, "Is API RP 14E Reliable for Predicting an Erosional Production Velocity when Sand Production is Anticipated?," Proceedings of ETCE/OMAE Joint Conference, pp. 14-17.

Meng, H. C., Ludema, K. C., 1995, "Wear Models and Predictive Equations: Their Form and Content," Wear, Vol. 181, pp. 443-457.

Misra, A., Finnie, I., 1981, "On the Size Effect in Abrasive and Erosive Wear," Wear, Vol. 65, pp. 359-373.

Molinari, J.F., Ortiz, M., 2002, "A Study of Solid-Particle Erosion of Metallic Targets," International Journal of Impact Engineering, Vol. 27, pp. 347-358.

Nguyen, A. V., Fletcher, C. A. J., 1999, "Particle Interaction with the Wall Surface in Two-Phase Gas-Solid Particle Flow", International journal of multiphase flow, Vol. 25, pp. 139-154.

Nidasanametla, S.A., 2012, Effects of Viscosity, Particle Size and Shape on Erosion Measurements and Predictions, M.Sc. Thesis, Department of Mechanical Engineering, The University of Tulsa.

Niu, Y. Y., 2001, "Evaluation of Erosion in a Two-Way Coupled Fluid-Particle System," International journal for numerical methods in fluids, Vol. 36, pp. 711-742.

Niu, Y.Y., Tsai, C. S., 2000, "Simulation of Erosion by the Dilute Particulate Flow

Impact," Numerical Heat Transfer, Part A, Vol. 37, pp. 167-187.

Njobuenwu, D.O., Fairweather, M., 2012, "Modeling of Pipe Bend Erosion by Dilute Particle Suspensions," Computers & Chemical Engineering, Vol. 42, pp. 235-247.

Nokleberg, L., Sontvedt, T. 1995, "Erosion in Choke Valves - Oil and Gas Industry Applications," Wear, Vol. 186, pp. 401-412.

Oka, Y.I., Ohnogi, H., Hosokawa, T., Matsumura, M., 1997, "The Impact Angle Dependence of Erosion Damage Caused by Solid Particle Impact," Wear, Vol. 203, pp. 573-579.

Oka, Y.I., Okamura, K., Yoshida, T., 2005a, "Practical Estimation of Erosion Damage Caused by Solid Particle Impact: Part 1: Effects of Impact Parameters on a Predictive Equation," Wear, Vol. 259, pp. 95-101.

Oka, Y.I., Yoshida, T., 2005b, "Practical Estimation of Erosion Damage Caused by Solid Particle Impact: Part 2: Mechanical Properties of Materials Directly Associated with Erosion Damage," Wear, Vol. 259, pp. 102-109.

Pan, L., Hanratty, T.J., 2002, "Correlation of Entrainment for Annular Flow in Horizontal Pipes," International journal of multiphase flow, Vol. 28, pp. 385-408.

Papini, M., Dhar, S., 2006, "Experimental Verification of a Model of Erosion due to the Impact of Rigid Single Angular Particles on Fully Plastic Targets," International journal of mechanical sciences, Vol. 48, pp. 469-482.

Pereira, G.C., de Souza, F.J., de Moro Martins, D.A., 2014, "Numerical Prediction of the Erosion Due to Particles in Elbows", Powder Technology, Vol. 261, pp. 105-117.

Powers, M.C., 1953, "A New Roundness Scale for Sedimentary Particles," Journal of Sedimentary Research, Vol. 23

Rickerby, D.G., Macmillan, N. H., 1980, "On the Oblique Impact of a Rigid Sphere against a Rigid-Plastic Solid," International Journal of Mechanical Sciences, Vol. 22, pp. 491-494.

Salama, M., 2000, "An Alternative to API RP 14E Erosional Velocity Limits for Sand-Laden Fluids," Journal of Energy Resources Technology, Vol. 122, pp. 71-77.

Salama, M., Venkatesh, E., 1983, "Evaluation of API RP 14E Erosional Velocity Limitations for Offshore Gas Wells," Proceedings of the 15th Offshore Technology Conference, Houston, TX, Paper No. 4485.

Schuh, M. J., Schuler, C. A., Humphrey, J. A. C., 1989, "Numerical calculation of particle-laden gas flows past tubes,", AIChE Journal, Vol. 35, pp. 466-480.

Sheldon, G. L., 1970, "Similarities and differences in the erosion behavior of materials," Journal of Fluids Engineering, Vol. 92, pp. 619-626.

Sheldon, G.L., Finnie, I., 1966, "The mechanism of material removal in the erosive cutting of brittle materials," J. Manuf. Sci. Eng., Vol. 88, pp. 393-399.

Sheldon, G.L., Kanhere, A., 1972, "An investigation of impingement erosion using single particles," Wear, Vol. 21, pp. 195-209.

Shipway, P.H., Hutchings, I.M., 1996, "The Role of Particle Properties in the Erosion of Brittle Materials" Wear, Vol. 193, 105-113.

Shirazi, S., McLaury, B., 2000, "Erosion modeling of elbows in multiphase flow," Proceedings of ASME Fluids Engineering Summer Meeting, pp. 11-15.

Shirazi, S., McLaury, B., Shadley, J., Rybicki, E., 1995a, "Generalization of the API RP 14 E Guideline for Erosive Service," Journal of Petroleum Technology, August, pp. 693-698.

Shirazi, S., Shadley, J., McLaury, B., Rybicki, E., 1995b, "A Procedure to Predict Solid Particle Erosion in Elbows and Tees," Journal of Pressure Vessel Technology, Vol. 117, pp. 45-52

Simmons, M.J., Hanratty, T.J., 2001, "Droplet Size Measurements in Horizontal Annular Gas-Liquid Flow," International journal of multiphase flow, Vol. 27, pp. 861-883.

Springer, G. S., 1976, "Erosion by liquid impact," John Wiley and Sons, New York, NY

Sundararajan, G., 1991, "A Comprehensive Model for the Solid Particle Erosion of Ductile Materials," Wear, Vol. 149, pp. 111-127.

Sundararajan, G., Shewmon, P. G., 1983, "A new model for the erosion of metals at normal incidence," Wear, Vol. 84, pp. 237-258.

Svedeman, S. J., 1995, "Experimental Study of the Erosional/Corrosional Velocity Criterion for Sizing Multiphase Flow Lines, Phase II - Experimental Results, Final Report" , SwRI Project No. 04-6461, Southwest Research Institute, San Antonio, Texas

Svedeman, S., Arnold, K., 1993, "Criteria for Sizing Multiphase Flow Lines for Erosive/Corrosive Service." SPE Production & Facilities, Vol. 9, pp. 74-80.

Tatterson, D.F., Dallman, J.C., Hanratty, T.J., 1977, "Drop Sizes in Annular Gas-Liquid Flows," AIChE Journal, Vol. 23, pp. 68-76.

Taylor, J.R., 1981, "An Introduction To Error Analysis: The Study Of Uncertainties In Physical Measurements," University Science Books, Mill Valley, CA

Thiruvengadam, A., Rudy, S. L., 1969, "Experimental and Analytical Investigations on Multiple Liquid Impact Erosion," (Washington D.C.: NASA)

Thiruvengadam, A., Rudy, S.L., 1969, "Experimental and Analytical Investigations on

Multiple Liquid Impact Erosion," NASA, Washington D.C..

Tilly, G.P., 1973, "A Two Stage Mechanism of Ductile Erosion," Wear, Vol. 23, 1973, pp. 87-96.

Vieira, R.E., 2014, Sand Erosion Model Improvement for Elbows in Gas Production, Multiphase Annular and Low-Liquid Flow, Ph.D. Dissertation, Department of Mechanical Engineering, The University of Tulsa.

Wada, S., Watanabe, N., 1987, "Solid Particle Erosion of Brittle Materials. III. The Interaction with Material Properties of Target and that of Impingement Particle on Erosive Wear Mechanism," J. Ceram. Soc. Jpn., Vol. 95, pp. 573-578.

Wang, Y.F., Yang, Z.G., 2008, "Finite Element Model of Erosive Wear on Ductile and Brittle Materials," Wear, Vol. 265, pp. 871-878.

Williams, J. H., Lau, E. K., 1974, "Solid particle erosion of graphite-epoxy composites," Wear, Vol. 29, pp. 219-230.

Wong, C.Y., Solnordal, C., Swallow, A., Wu, J., 2013, "Experimental and Computational Modelling of Solid Particle Erosion in a Pipe Annular Cavity," Wear, Vol. 303, pp. 109-129.

Zhang, Y., 2006, Application and Improvement of Computational Fluid Dynamics (CFD) in Solid Particle Erosion Modeling, Ph.D. Dissertation, Department of Mechanical Engineering, The University of Tulsa.

Zhang, Y., Reuterfors, E.P., McLaury, B. S., Shirazi, S. A., Rybicki, E. F., 2007, "Comparison of Computed and Measured Particle Velocities and Erosion in Water and Air Flows," Wear, Vol. 263, pp. 330-338.

SAND EROSION DATA

Table A.1 Erosion data for carbon steel 1018 at particle velocity of 9.2 m/s

Specimen: Carbon Steel 1018			Gas Velocity: 29.2 m/s			
Particle: Sand 150 µm			Particle Velocity: 9.2 m/s			
Impact Angle (degree)	Specimen #	start (g)	600 g	1200 g	1800 g	ER (g/g)
90	15	94.8489	94.8485	94.8482	94.8479	5.00E-07
75	15	94.8502	94.8497	94.8495	94.8489	6.67E-07
60	15	94.8519	94.8514	94.8509	94.8502	1.00E-06
45	15	94.8577	94.8567	94.8561	94.8553	1.17E-06
45	15	94.8542	94.8535	94.8527	94.8519	1.33E-06
		start (g)	300 g	600 g	900 g	
30	53	94.8327	94.8324	94.8321	94.8316	1.33E-06
30	53	94.8311	94.8307	94.8302	94.8297	1.67E-06
30	18	94.8573	94.8566	94.8557	94.8548	3.00E-06
15	20	95.0253	95.0241	95.0232	95.0224	2.83E-06
15	20	95.0224	95.0211	95.0204	95.0196	2.50E-06

Table A.2 Erosion data for carbon steel 1018 at particle velocity of 18.4 m/s

Specimen: Carbon Steel 1018			Gas Velocity: 58.4 m/s			
Particle: Sand 150 µm			Particle Velocity: 18.4 m/s			
Impact Angle (degree)	Specimen #	start (g)	300 g	600 g	900 g	ER (g/g)
90	97	95.0004	94.9997	94.9989	94.9975	3.67E-06
90	22	94.9785	94.9780	94.9773	94.9761	3.17E-06
75	22	94.9767	94.9752	94.9740	94.9733	3.17E-06
75	22	94.9733	94.9712	94.9697	94.9682	5.00E-06
60	24	95.0322	95.0306	95.0281	95.0259	7.83E-06
60	24	95.0259	95.0236	95.0214	95.0181	9.17E-06
45	24	95.0175	95.0155	95.0126	95.0105	8.33E-06
45	24	95.0105	95.0082	95.0057	95.0034	8.00E-06
45	19	94.6094	94.6067	94.6032	94.6007	1.00E-05
30	19	94.6208	94.6176	94.6135	94.6094	1.37E-05
30	57	94.0408	94.0377	94.0335	94.0305	1.20E-05
15	19	94.6559	94.6529	94.6497	94.6464	1.08E-05
15	19	94.6464	94.6432	94.6401	94.6368	1.07E-05

Table A.3 Erosion data for carbon steel 1018 at particle velocity of 27.6 m/s

Specimen: Carbon Steel 1018			Gas Velocity: 87.6 m/s			
Particle: Sand 150 μm			Particle Velocity: 27.6 m/s			
Impact Angle (degree)	Specimen #	start (g)	300 g	600 g	900 g	ER (g/g)
90	22	94.9679	94.9659	94.9632	94.9608	8.50E-06
90	22	94.9608	94.9577	94.9552	94.9527	8.33E-06
75	16	95.0473	95.0440	95.0400	95.0353	6.74E-07
75	97	95.0353	95.0320	95.0271	95.0225	2.89E-07
60	16	95.0654	95.0592	95.0528	95.0470	5.77E-07
60	17	94.9704	94.9644	94.9581	94.9525	6.74E-07
45	97	95.0223	95.0149	95.0077	95.0006	9.62E-08
45	57	94.0806	94.0737	94.0665	94.0585	7.70E-07
30	19	94.6860	94.6759	94.6658	94.6561	3.85E-07
30	18	94.9215	94.9120	94.9016	94.8923	1.06E-06
15	21	94.5256	94.5169	94.5086	94.5010	6.74E-07
15	20	95.0915	95.0832	95.0746	95.0667	6.74E-07

Table A.4 Erosion data for carbon steel 4130 at particle velocity of 9.2 m/s

Specimen: Carbon Steel 4130			Gas Velocity: 29.2 m/s			
Particle: Sand 150 μm			Particle Velocity: 9.2 m/s			
Impact Angle (degree)	Specimen #	start (g)	600 g	1200 g	1800 g	ER (g/g)
90	29	46.3141	46.3134	46.3130	46.3128	5.00E-07
75	44	45.7830	45.7828	45.7826	45.7822	5.00E-07
60	34	46.4636	46.4628	46.4624	46.4622	5.00E-07
45	25	48.0385	48.0374	48.0363	48.0354	1.67E-06
45	45	46.7798	46.7793	46.7783	46.7774	1.58E-06
		start (g)	300 g	600 g	900 g	
30	47	48.8089	48.8084	48.8076	48.8066	3.00E-06
30	47	48.8063	48.8060	48.8053	48.8041	3.17E-06
30	47	48.8089	48.8084	48.8076	48.8066	3.17E-06
15	36	48.0853	48.0843	48.0832	48.0824	3.00E-06
15	36	48.0824	48.0817	48.0809	48.0799	3.00E-06

Table A.5 Erosion data for carbon steel 4130 at particle velocity of 18.4 m/s

| Specimen: Carbon Steel 4130 | | | Gas Velocity: 58.4 m/s | | | |
| Particle: Sand 150 µm | | | Particle Velocity: 18.4 m/s | | | |
Impact Angle (degree)	Specimen #	start (g)	300 g	600 g	900 g	ER (g/g)
90	44	45.7869	45.7866	45.7859	45.7852	2.33E-06
90	44	45.7852	45.7848	45.7838	45.7828	3.33E-06
75	45	46.7859	46.7846	46.7837	46.7830	2.67E-06
75	45	46.7830	46.7821	46.7810	46.7798	3.83E-06
60	32	45.6674	45.6658	45.6647	45.6630	4.67E-06
60	32	45.6630	45.6616	45.6596	45.6583	5.50E-06
45	25	46.5378	46.5355	46.5331	46.5305	8.33E-06
45	25	46.5305	46.5278	46.5248	46.5211	1.12E-05
45	34	46.4231	46.4202	46.4178	46.4147	9.17E-06
30	33	46.5211	46.5183	46.5153	46.5123	1.00E-05
30	33	46.5123	46.5095	46.5065	46.5034	1.02E-05
30	34	46.4345	46.4309	46.4277	46.4231	1.30E-05
15	31	47.8859	47.8818	47.8775	47.8735	1.38E-05
15	31	47.8735	47.8699	47.8657	47.8615	1.40E-05
15	27	49.6516	49.6476	49.6431	49.6392	1.40E-05

Table A.6 Erosion data for carbon steel 4130 at particle velocity of 27.6 m/s

Specimen: 4130 Carbon Steel			Gas Velocity: 87.6 m/s			
Particle: Sand 150 μm			Particle Velocity: 27.6 m/s			
Impact Angle (degree)	Specimen #	start (g)	300 g	600 g	900 g	ER (g/g)
90	36	48.0935	48.0926	48.0905	48.0881	7.50E-06
90	29	46.3270	46.3254	46.3219	46.3209	7.50E-06
75	33	46.5508	46.5471	46.5432	46.5401	1.17E-05
75	32	45.7133	45.7099	45.7063	45.7033	1.10E-05
60	29	46.3638	46.3589	46.3538	46.3478	1.85E-05
60	28	45.8265	45.8216	45.8162	45.8107	1.82E-05
45	29	46.3478	46.3411	46.3347	46.3277	2.23E-05
45	27	46.6716	46.6646	46.6581	46.6511	2.25E-05
30	30	46.8064	46.8014	46.7957	46.7872	2.37E-05
30	28	45.8104	45.8028	45.7952	45.7878	2.50E-05
15	26	48.6468	48.6373	48.6287	48.6213	2.67E-05
15	27	49.6980	49.6891	49.6800	49.6722	2.82E-05

Table A.7 Erosion data for stainless steel 316 at particle velocity of 9.2 m/s

Specimen: Stainless Steel 316			Gas Velocity: 29.2 m/s			
Particle: Sand 150 µm			Particle Velocity: 9.2 m/s			
Impact Angle (degree)	Specimen #	start (g)	300 g	600 g	1200 g	ER (g/g)
90	29	45.59913	45.59897	45.5989	45.59883	2.22E-07
75	29	45.59977	45.59960	45.59933	45.59927	5.56E-07
60	28	45.67527	45.67497	45.67483	45.6748	3.33E-07
45	28	45.67617	45.67580	45.67543	45.67527	8.89E-07
30	28	45.67633	45.67623	45.67617	45.67587	6.11E-07
15	28	45.67813	45.67750	45.677	45.67633	1.94E-06

Table A.8 Erosion data for stainless steel 316 at particle velocity of 18.4 m/s

Specimen: Stainless Steel 316			Gas Velocity: 58.4 m/s			
Particle: Sand 150 µm			Particle Velocity: 18.4 m/s			
Impact Angle (degree)	Specimen #	start (g)	300 g	600 g	900 g	ER (g/g)
90	11	44.0738	44.073	44.0720	44.0707	3.83E-06
90	11	44.0707	44.0695	44.0679	44.0668	4.50E-06
75	11	44.0664	44.0646	44.0631	44.0609	6.17E-06
75	11	44.0609	44.0593	44.0576	44.0557	6.00E-06
60	11	44.0557	44.0538	44.0513	44.0492	7.67E-06
60	11	44.0492	44.0469	44.0448	44.0427	7.00E-06
45	11	44.0426	44.0409	44.0381	44.0354	9.17E-06
45	11	44.0354	44.0334	44.0310	44.0281	8.83E-06
30	14	43.4089	43.4068	43.4029	43.3996	1.20E-05
30	14	43.3996	43.397	43.3932	43.3896	1.23E-05
15	3	44.1385	44.1346	44.1313	44.1275	1.18E-05
15	22	46.5415	46.5373	46.5335	46.5296	1.28E-05

Table A.9 Erosion data for stainless steel 316 at particle velocity of 27.6 m/s

Specimen: Stainless Steel 316			Gas Velocity: 87.6 m/s			
Particle: Sand 150 µm			Particle Velocity: 27.6 m/s			
Impact Angle (degree)	Specimen #	start (g)	300 g	600 g	900 g	ER (g/g)
90	12	43.1735	43.1703	43.1660	43.1617	1.43E-05
90	18	45.5355	45.5327	45.5288	45.5247	1.33E-05
90	15RF	45.2025	45.1965	45.1911	45.1874	1.52E-05
90	15LF	45.1664	45.1633	45.158	45.1535	1.63E-05
75	2	43.1617	43.1582	43.1538	43.1489	1.55E-05
75	18	45.5249	45.5213	45.5168	45.5125	1.47E-05
60	2	43.1489	43.1432	43.1375	43.1310	2.03E-05
60	18	45.5125	45.5079	45.5014	45.4962	1.95E-05
45	2	43.1310	43.1244	43.1173	43.11041	2.33E-05
45	18	45.4932	45.4894	45.4827	45.4748	2.43E-05
30	12	44.8763	44.8686	44.8610	44.8535	2.52E-05
30	12	44.8535	44.8462	44.8389	44.8315	2.45E-05
15	18	44.8535	44.8453	44.8369	44.8290	2.72E-05
15	13	47.152	47.1427	47.1332	47.1274	2.55E-05

Table A.10 Erosion data for stainless steel 2205 at particle velocity of 9.2 m/s

Specimen: Stainless Steel 2205			Gas Velocity: 29.2 m/s			
Particle: Sand 150 μm			Particle Velocity: 9.2 m/s			
Impact Angle (degree)	Specimen #	start (g)	600 g	1200 g	1800 g	ER (g/g)
90	47	45.2274	45.2271	45.2269	45.2264	5.83E-07
75	38	44.4951	44.4949	44.4945	44.4942	5.83E-07
60	38	44.4964	44.4959	44.4955	44.4951	6.67E-07
45	14	45.1123	45.1117	45.1112	45.1106	9.17E-07
45	47	45.2335	45.2327	45.2318	45.2309	1.50E-06
30	44	45.1164	45.1158	45.1149	45.1135	1.92E-06
		start (g)	300 g	600 g	900 g	
30	39	45.1192	45.1183	45.1175	45.1168	2.50E-06
30	39	45.1168	45.1161	45.1156	45.1147	2.33E-06
15	46	45.0578	45.0570	45.0561	45.0556	2.33E-06
15	46	45.0556	45.0548	45.0536	45.0526	3.67E-06

Table A.11 Erosion data for stainless steel 2205 at particle velocity of 18.4 m/s

Specimen: Stainless Steel 2205			Gas Velocity: 58.4 m/s			
Particle: Sand 150 μm			Particle Velocity: 18.4 m/s			
Impact Angle (degree)	Specimen #	start (g)	300 g	600 g	900 g	ER (g/g)
90	45	45.2030	45.2023	45.2014	45.2005	3.00E-06
90	37	45.0435	45.0426	45.0419	45.0407	3.17E-06
75	37	45.0374	45.0362	45.0342	45.0310	8.67E-06
60	43	44.6490	44.6481	44.6459	44.6445	6.00E-06
60	42	44.5196	44.5183	44.5167	44.5149	5.67E-06
45	14	45.1294	45.1277	45.1260	45.1242	5.83E-06
45	14	45.1242	45.1229	45.1213	45.1196	5.50E-06
30	42	44.5144	44.5119	44.5098	44.5068	8.50E-06
30	42	44.5068	44.5043	44.5022	44.4997	7.67E-06
30	45	45.1851	45.1825	45.1802	45.1768	9.50E-06
15	44	45.1318	45.1296	45.1275	45.1251	7.50E-06
15	44	45.1251	45.1208	45.1182	45.1161	7.83E-06
15	40	45.6541	45.6519	45.6488	45.6454	1.08E-05

Table A.12 Erosion data for stainless steel 2205 at particle velocity of 27.6 m/s

Specimen: Stainless Steel 2205			Gas Velocity: 87.6 m/s			
Particle: Sand 150 μm			Particle Velocity: 27.6 m/s			
Impact Angle (degree)	Specimen #	start (g)	300 g	600 g	900 g	ER (g/g)
90	47	45.2438	45.2408	45.2410	45.2371	6.17E-06
90	46	45.0280	45.0278	45.0263	45.0256	3.67E-06
75	45	45.2106	45.2083	45.2051	45.2020	1.05E-05
75	44	45.1396	45.1371	45.1337	45.1311	1.00E-05
60	43	44.6836	44.6799	44.6761	44.6732	1.12E-05
60	42	44.5290	44.5262	44.5226	44.5195	1.12E-05
45	37	45.0553	45.0530	45.0461	45.0412	1.97E-05
45	38	44.5109	44.5064	44.5028	44.4970	1.57E-05
30	40	45.6761	45.6680	45.6609	45.6544	2.27E-05
30	41	44.2888	44.2811	44.2734	44.2672	2.32E-05
15	38	44.5326	44.5246	44.5175	44.5110	2.27E-05
15	39	45.1495	45.1426	45.1361	45.1293	2.22E-05

Table A.13 Erosion data for 13 chrome duplex at particle velocity of 9.2 m/s

Specimen: 13 Chrome Duplex			Gas Velocity: 29.2 m/s			
Particle: Sand 150 μm			Particle Velocity: 9.2 m/s			
Impact Angle (degree)	Specimen #	start (g)	600 g	1200 g	1800 g	ER (g/g)
90	3	204.6260	204.6255	204.6252	204.6247	6.67E-07
75	3	204.6276	204.6273	204.6268	204.6260	1.08E-06
60	3	204.6295	204.6289	204.6285	204.6276	1.08E-06
45	3	204.6327	204.6320	204.6309	204.6295	2.08E-06
45	25	204.7585	204.7573	204.7563	204.7550	1.92E-06
		start (g)	300 g	600 g	900 g	
30	10	204.2932	204.2928	204.2918	204.2911	2.83E-06
30	10	204.2911	204.2906	204.2900	204.2894	2.00E-06
30	5	196.4602	196.4596	196.4588	196.4578	3.00E-06
15	6	203.7730	203.7721	203.7716	203.7711	1.67E-06
15	5	196.5289	196.5281	196.5273	196.5267	2.33E-06
15	5	196.4636	196.4631	196.4618	196.4602	4.83E-06

Table A.14 Erosion data for 13 chrome duplex at particle velocity of 18.4 m/s

Specimen: 13 Chrome Duplex			Gas Velocity: 58.4 m/s			
Particle: Sand 150 μm			Particle Velocity: 18.4 m/s			
Impact Angle (degree)	Specimen #	start (g)	300 g	600 g	900 g	ER (g/g)
90	12	204.4440	204.4438	204.4428	204.4419	3.17E-06
90	12	204.4419	204.4409	204.4400	204.4390	3.17E-06
75	12	204.4390	204.4384	204.4373	204.4357	4.50E-06
75	12	204.4356	204.4341	204.4330	204.4319	3.67E-06
60	6	203.7253	203.7238	203.7216	203.7198	6.67E-06
45	6	203.7184	203.7176	203.7158	203.7140	6.00E-06
45	6	203.7140	203.7129	203.7112	203.7093	6.00E-06
30	4	201.1053	201.1036	201.1003	201.0978	9.67E-06
30	4	201.0978	201.0959	201.0937	201.0914	7.50E-06
15	4	201.0912	201.0884	201.0858	201.0835	8.17E-06
15	4	201.0835	201.0811	201.0788	201.0762	8.17E-06
15	3	204.6239	204.6210	204.6186	204.6158	8.67E-06

Table A.15 Erosion data for 13 chrome duplex at particle velocity of 27.6 m/s

Specimen: 13 Chrome Duplex			Gas Velocity: 87.6 m/s			
Particle: Sand 150 μm			Particle Velocity: 27.6 m/s			
Impact Angle (degree)	Specimen #	start (g)	300 g	600 g	900 g	ER (g/g)
90	12	204.4511	204.4488	204.4459	204.4442	7.67E-06
90	11	204.0450	204.0433	204.0412	204.0388	7.50E-06
90	11	204.0388	204.0372	204.0352	204.0327	7.50E-06
75	9	203.0771	203.0745	203.0720	203.0694	8.50E-06
75	9	203.0689	203.0661	203.0630	203.0595	1.10E-05
60	10	204.3166	204.3126	204.3089	204.3049	1.28E-05
60	10	204.3049	204.3012	204.2976	204.2938	1.23E-05
45	88	203.0591	203.0549	203.0495	203.0443	1.77E-05
45	11	204.0621	204.0569	204.0523	204.0462	1.78E-05
30	7	204.7808	204.7752	204.7677	204.7610	2.37E-05
30	8	204.4381	204.4321	204.4255	204.4183	2.30E-05
15	1	204.2287	204.2227	204.2158	204.2105	2.03E-05
15	2	203.2864	203.2791	203.2728	203.2676	1.92E-05

Table A.16 Erosion data for Inconel 625 at particle velocity of 9.2 m/s

Impact Angle (degree)	Specimen #	start (g)	600 g	1200 g	1800 g	ER (g/g)
Specimen: Inconel 625			Gas Velocity: 29.2 m/s			
Particle: Sand 150 µm			Particle Velocity: 9.2 m/s			
90	60	49.8835	49.8833	49.8828	49.8826	5.83E-07
75	60	49.8849	49.8847	49.8842	49.8835	1.00E-06
60	60	49.8870	49.8867	49.8859	49.8849	1.50E-06
45	59	45.7243	45.7238	45.7229	45.7220	1.50E-06
45	59	45.7220	45.7211	45.7202	45.7192	1.58E-06
		start (g)	300 g	600 g	900 g	
30	82	45.7316	45.7314	45.7307	45.7295	3.17E-06
30	82	45.7295	45.7294	45.7292	45.7283	1.83E-06
30	57	47.8312	47.8294	47.8284	47.8271	3.83E-06
15	63	47.6141	47.6129	47.6119	47.6105	4.00E-06
15	63	47.6105	47.6095	47.6086	47.6075	3.33E-06
15	49	48.1547	48.1525	48.1515	48.1496	4.83E-06

Table A.17 Erosion data for Inconel 625 at particle velocity of 18.4 m/s

Specimen: Inconel 625			Gas Velocity: 58.4 m/s			
Particle: Sand 150 μm			Particle Velocity: 18.4 m/s			
Impact Angle (degree)	Specimen #	start (g)	300 g	600 g	900 g	ER (g/g)
90	58	49.6471	49.6469	49.6458	49.6447	3.67E-06
90	58	49.6447	49.6443	49.6434	49.6424	3.17E-06
75	53	49.0276	49.0268	49.0259	49.0253	2.50E-06
75	53	49.0253	49.0242	49.0230	49.0222	3.33E-06
60	53	49.6304	49.6296	49.6280	49.6264	5.33E-06
60	52	49.8965	49.8956	49.8945	49.8930	4.33E-06
45	63	47.6228	47.6219	47.6202	47.6183	6.00E-06
45	63	47.6183	47.6171	47.6153	47.6137	5.67E-06
45	50	48.6403	48.6388	48.6372	48.6355	5.50E-06
30	55	49.4313	49.4297	49.4278	49.4258	6.50E-06
30	55	49.4258	49.4240	49.4219	49.4195	7.50E-06
30	60	49.8733	49.8713	49.8695	49.8669	7.70E-07
30	50	48.6477	48.6456	48.6437	48.6410	7.67E-06
15	55	49.4195	49.4170	49.4142	49.4117	8.83E-06
15	54	47.3141	47.3114	47.3088	47.3062	8.67E-06
15	50	48.6559	48.6528	48.6501	48.6477	8.50E-06

Table A.18 Erosion data for Inconel 625 at particle velocity of 27.6 m/s

Specimen: Inconel 625			Gas Velocity: 87.6 m/s			
Particle: Sand 150 μm			Particle Velocity: 27.6 m/s			
Impact Angle (degree)	Specimen #	start (g)	300 g	600 g	900 g	ER (g/g)
90	53	49.0099	49.0072	49.0041	49.0009	1.05E-05
75	53	49.0223	49.0184	49.0145	49.0099	1.42E-05
60	56	47.2393	47.2349	47.2301	47.2244	1.75E-05
45	56	47.2586	47.2520	47.2455	47.2393	2.12E-05
30	56	47.2816	47.2742	47.2668	47.2586	2.60E-05
15	56	47.3058	47.2981	47.2899	47.2812	2.82E-05

Table A.19 Erosion data for aluminum alloy 6061 at particle velocity of 9.2 m/s

Specimen: Aluminum Alloy 6061			Gas Velocity: 29.2 m/s			
Particle: Sand 150 μm			Particle Velocity: 9.2 m/s			
Impact Angle (degree)	Specimen #	start (g)	600 g	1200 g	1800 g	ER (g/g)
90	68	16.3975	16.3975	16.3975	16.3974	8.33E-08
75	68	16.3977	16.3977	16.3976	16.3975	1.67E-07
60	68	16.3978	16.3978	16.3978	16.3976	1.67E-07
		start (g)	300 g	600 g	900 g	
30	69	16.5861	16.5858	16.5855	16.5854	6.67E-07
30	69	16.5854	16.5852	16.5850	16.5849	5.00E-07
30	57	16.6193	16.6189	16.6184	16.6182	1.17E-06
15	67	16.6681	16.6677	16.6668	16.6665	2.00E-06
15	67	16.6665	16.6658	16.6650	16.6642	2.67E-06
15	57	16.6212	16.6208	16.6201	16.6193	2.50E-06

Table A.20 Erosion data for aluminum alloy 6061 at particle velocity of 18.4 m/s

Specimen: Aluminum Alloy 6061			Gas Velocity: 58.4 m/s			
Particle: Sand 150 μm			Particle Velocity: 18.4 m/s			
Impact Angle (degree)	Specimen #	start (g)	300 g	600 g	900 g	ER (g/g)
90	64	16.4377	16.4373	16.4365	16.4359	2.33E-06
90	68	16.3998	16.3994	16.3987	16.3981	2.17E-06
90	78	16.5580	16.5575	16.5566	16.5558	2.83E-06
75	66	16.5729	16.5726	16.5723	16.5715	1.83E-06
75	66	16.5715	16.5713	16.5710	16.5704	1.50E-06
60	65	16.5202	16.5193	16.5186	16.5178	2.50E-06
60	62	16.9126	16.9118	16.9111	16.9101	2.83E-06
60	68	16.3110	16.3099	16.3081	16.3067	5.33E-06
45	64	16.4357	16.4344	16.4324	16.4297	7.83E-06
45	64	16.4297	16.4288	16.4274	16.4259	4.83E-06
45	65	16.5175	16.5159	16.5140	16.5119	6.67E-06
30	61	16.2569	16.2555	16.2532	16.2506	8.17E-06
30	61	16.2506	16.2489	16.2459	16.2437	8.67E-06
15	67	16.6839	16.6819	16.6788	16.6758	1.02E-05
15	67	16.6758	16.6739	16.6713	16.6684	9.17E-06

Table A.21 Erosion data for aluminum alloy 6061 at particle velocity of 27.6 m/s

Specimen: Aluminum Alloy 6061			Gas Velocity: 87.6 m/s			
Particle: Sand 150 µm			Particle Velocity: 27.6 m/s			
Impact Angle (degree)	Specimen #	start (g)	300 g	600 g	900 g	ER (g/g)
90	66	16.5695	16.5684	16.5664	16.5640	7.33E-06
90	66	16.5640	16.5628	16.5609	16.5582	7.67E-06
90	64	16.3845	16.3819	16.3799	16.3778	6.83E-06
75	67	16.7052	16.7037	16.7018	16.6998	6.50E-06
75	66	16.5821	16.5805	16.5787	16.5774	5.17E-06
75	64	16.3923	16.3899	16.3875	16.3845	9.00E-06
60	64	16.4465	16.4437	16.4416	16.4379	9.67E-06
60	65	16.5611	16.5586	16.5560	16.5528	9.67E-06
60	64	16.4043	16.4001	16.3962	16.3923	1.30E-05
45	69	16.6009	16.5969	16.5917	16.5859	1.83E-05
45	67	16.7002	16.6963	16.6902	16.6843	2.00E-05
30	65	16.5525	16.5477	16.5418	16.5358	1.98E-05
30	65	16.5358	16.5309	16.5251	16.5196	1.88E-05
15	61	16.2838	16.2771	16.2698	16.2628	2.38E-05
15	69	16.6218	16.6147	16.6076	16.6010	2.28E-05

APPENDIX B

EROSION DATA FOR OTHER SOLID PARTICLES

Table B.1 Erosion data for other solid particles in submerged configuration (particle concentration: 1% (kg/kg))

Test	Spec. #	Liq. Vel. (m/s)	Particle	Time (hr)	Start W. (g)	Stop W. (g)	Loss (g)	ER (g/g)
submerged	61	16.8	Silicon Carbide	72	45.3887	45.0062	0.3825	2.07E-07
submerged	58	16.8	Silicon Carbide	72	45.5166	45.1595	0.3571	1.93E-07
submerged	63	16.8	Silicon Carbide	72	45.5844	45.2493	0.3351	1.81E-07
submerged	42	16.8	Alumina	72	45.7791	45.5514	0.2277	1.23E-07
submerged	24	16.8	Alumina	72	45.7677	45.5066	0.2611	1.41E-07
submerged	57	16.8	Alumina	72	45.7547	45.5166	0.2381	1.29E-07
submerged	2	16.8	Silica Flour	72	45.4643	44.6531	0.8112	4.38E-07
submerged	9-R	16.8	Silica Flour	72	47.1676	46.221	0.9466	5.11E-07
submerged	15	16.8	Silica Flour	72	45.4635	44.5647	0.8988	4.85E-07
submerged	6	16.8	Magnetite	72	48.9442	48.8238	0.1204	6.50E-08

submerged	11-R	16.8	Magnetite	72	47.3183	47.2012	0.1171	6.32E-08
submerged	33	16.8	Magnetite	72	45.6473	45.5419	0.1054	5.69E-08
submerged	67	16.8	Hematite	72	45.6763	45.0515	0.6248	3.37E-07
submerged	71	16.8	Hematite	72	45.7439	45.3695	0.3744	2.02E-07
submerged	73	16.8	Hematite	72	45.7708	45.133	0.6378	3.44E-07
submerged	84	16.8	Hematite	72	45.4173	44.4735	0.9438	5.10E-07
submerged	81	16.8	Apatite	72	45.3925	44.2105	1.1820	6.38E-07
submerged	80	16.8	Apatite	72	45.3956	45.1278	0.2678	1.45E-07
submerged	85	16.8	Apatite	72	45.5043	45.2565	0.2478	1.34E-07
submerged	9	16.8	Barite	72	47.3157	47.1903	0.1254	6.77E-08
submerged	5-R	16.8	Barite	72	48.7833	48.6723	0.1110	5.99E-08
submerged	25	16.8	Barite	72	45.8261	45.6955	0.1306	7.05E-08
submerged	25	16.8	Barite	72	45.8261	45.6955	0.1306	7.05E-08
submerged	14	16.8	Calcite	72	45.7177	45.7054	0.0123	6.64E-09
submerged	21	16.8	Calcite	72	45.7167	45.7043	0.0124	6.69E-09
submerged	41	16.8	Calcite	72	45.8055	45.7798	0.0257	1.39E-08
submerged	10	16.8	Iron Powder	72	47.1893	47.1699	0.0194	1.05E-08
submerged	6-R	16.8	Iron Powder	72	48.6423	48.6179	0.0244	1.32E-08
submerged	30	16.8	Iron Powder	72	45.6949	45.6709	0.0240	1.30E-08

Table B.2 Erosion data for other solid particles in mist flow configuration (particle concentration: 1% (kg/kg))

Test	Spec. #	Gas Vel. (m/s)	Liq. Rate (ml/min)	Particle	Time (hr)	Start W.(g)	Stop W. (g)	Loss (g)	ER (g)
air/water	59	45	800	Silicon Carbide	72	45.4137	45.4093	0.0044	2.69E-07
air/water	56	45	800	Silicon Carbide	72	45.5766	45.5715	0.0051	3.12E-07
air/water	65	45	800	Silicon Carbide	72	45.5706	45.5647	0.0059	3.61E-07
air/water	34	45	800	Alumina	72	45.5421	45.5375	0.0046	2.81E-07
air/water	20	45	800	Alumina	72	45.4242	45.4179	0.0063	3.85E-07
air/water	55	45	800	Alumina	72	45.5863	45.5766	0.0097	5.93E-07
air/water	3	45	800	Silica Flour	72	48.1979	48.1833	0.0146	8.93E-07
air/water	7-L	45	800	Silica Flour	72	47.3366	47.3282	0.0084	5.14E-07
air/water	17	45	800	Silica Flour	72	45.6758	45.6719	0.0039	2.38E-07
air/water	10-2	45	800	Magnetite	72	47.1699	47.1676	0.0023	1.41E-07
air/water	35	45	800	Magnetite	72	45.4722	45.4717	0.0005	3.06E-08
air/water	45	45	800	Magnetite	72	45.8124	45.8085	0.0039	2.38E-07
air/water	69	45	800	Hematite	72	45.8531	45.8513	0.0018	1.10E-07
air/water	86	45	800	Hematite	72	45.2565	45.2543	0.0022	1.35E-07
air/water	86	45	800	Hematite	72	45.2543	45.2512	0.0031	1.90E-07
air/water	79	45	800	Apatite	72	45.3999	45.3956	0.0043	2.63E-07

air/water	82	45	800	Apatite	72	44.2105	44.2051	0.0054	3.30E-07
air/water	83	45	800	Apatite	72	45.4205	45.4173	0.0032	1.96E-07
air/water	7	45	800	Barite	72	47.3402	47.3375	0.0027	1.65E-07
air/water	27	45	800	Barite	72	45.7764	45.7754	0.001	6.11E-08
air/water	44	45	800	Barite	72	45.8088	45.8077	0.0011	6.73E-08
air/water	23	45	800	Calcite	72	45.7687	45.7672	0.0015	9.17E-08
air/water	37	45	800	Calcite	72	45.6314	45.6301	0.0013	7.95E-08
air/water	39	45	800	Calcite	72	45.1691	45.1677	0.0014	8.56E-08
air/water	8	45	800	Iron Powder	60	47.3371	47.3366	0.0005	3.67E-08
air/water	31	45	800	Iron Powder	72	45.5114	45.5112	0.0002	1.22E-08
air/water	47	45	800	Iron Powder	72	45.6689	45.6686	0.0003	1.83E-08

LIQUID IMPACT EROSION DATA

Table C.1 Liquid impact erosion data with brine (high velocity)

#	Material	Impact vel. (ft/s)	rpm	Time (hr)	Start weight (g)	End weight (g)	Loss (g)
1	Sm825	173.8	3510	71	11.32244	11.143695	0.178745
1	625	173.8	3510	71	12.358215	12.253387	0.104828
1	2205	173.8	3510	71	11.07646	11.030214	0.046246
1	Sm25-Cr	173.8	3510	71	10.418965	10.400229	0.018736
2	1018	173.8	3510	16	15.096604	14.582415	0.514189
2	1018	173.8	3510	16	14.788804	14.295345	0.493459
2	1018	173.8	3510	16	15.07943	14.579	0.50043
2	1018	173.8	3510	16	15.17995	14.680995	0.498955
3	316	173.8	3510	72	11.51495	11.514325	0.000625
3	2205	173.8	3510	72	10.59611	10.578245	0.017865
3	Sm25-Cr	173.8	3510	72	11.013405	11.009665	0.00374
3	13Cr-A	173.8	3510	72	12.98423	12.95477	0.02946
4	316	173.8	3510	72	11.18814	10.933445	0.254695

4	Sm825	173.8	3510	72	12.2282	11.8924	0.3358
4	625	173.8	3510	72	12.619215	12.542455	0.07676
4	13Cr-A	173.8	3510	72	12.911585	12.43835	0.473235
5	Sm825	173.8	3510	72	10.317765	9.99769	0.320075
5	625	173.8	3510	72	11.58382	11.548695	0.035125
5	2205	173.8	3510	72	10.09267	9.920665	0.172005
5	Sm25-Cr	173.8	3510	72	11.09197	10.983735	0.108235
6	316	173.8	3510	44	15.402755	15.278675	0.12408
6	9Cr-1M	173.8	3510	44	16.585615	15.703835	0.88178
6	13Cr-H	173.8	3510	44	13.593535	13.261185	0.33235
6	9Cr-1M	173.8	3510	44	18.209055	17.313155	0.8959
7	316	173.8	3510	72	10.894955	10.603075	0.29188
7	625	173.8	3510	72	12.694465	12.693275	0.00119
7	2205	173.8	3510	72	14.960055	14.78058	0.179475
7	Sm25-Cr	173.8	3510	72	14.843875	14.75773	0.086145

Table C.2 Liquid impact erosion data with tap water (high velocity)

#	Material	Impact vel. (ft/s)	rpm	Time (hr)	Start weight (g)	End weight (g)	Loss (g)
8	1018	173.8	3510	16	14.084425	13.928385	0.15604
8	1018	173.8	3510	16	14.44622	14.31093	0.13529
8	1018	173.8	3510	16	13.9626	13.798825	0.163775
8	1018	173.8	3510	16	13.85728	13.70532	0.15196
9	316	173.8	3510	72	14.816415	14.472285	0.34413
9	625	173.8	3510	72	13.43372	13.430575	0.003145
9	2205	173.8	3510	72	16.47961	16.311275	0.168335
9	Sm25-Cr	173.8	3510	72	14.09982	14.006315	0.093505
10A	Sm825	173.8	3510	69	13.319785	13.241335	0.07845
10A	9Cr-1M	173.8	3510	69	17.77244	17.599755	0.172685
10A	13Cr-A	173.8	3510	69	13.252485	13.149465	0.10302
10A	13Cr-H	173.8	3510	69	13.298375	13.11224	0.186135
10B	Sm825	173.8	3510	72	12.503675	12.285425	0.21825
10B	9Cr-1M	173.8	3510	72	13.792735	13.53403	0.258705
10B	13Cr-A	173.8	3510	72	13.513775	13.206925	0.30685
10B	13Cr-H	173.8	3510	72	12.99572	12.76823	0.22749

Table C.3 Liquid impact erosion data with brine (low velocity)

#	Material	Impact vel. (ft/s)	rpm	Time (hr)	Start weight (g)	End weight (g)	Loss (g)
11-A	1018	87.1	1782	72	14.965355	13.206865	1.75849
11-A	1018	87.1	1782	72	14.68792	12.714295	1.973625
11-A	1018	87.1	1782	72	14.02146	12.249635	1.771825
11-A	1018	87.1	1782	72	14.149435	12.464185	1.68525
12	316	87.1	1782	144	14.767355	14.767305	5E-05
12	625	87.1	1782	144	12.954375	12.9543	7.5E-05
12	2205	87.1	1782	144	16.01646	16.016295	0.000165
12	Sm25-Cr	87.1	1782	144	14.294345	14.293985	0.00036
13	Sm825	87.1	1782	144	13.91797	13.917785	0.000185
13	9Cr-1M	87.1	1782	144	16.163815	14.526175	1.63764
13	13Cr-A	87.1	1782	144	13.236215	13.208375	0.02784
13	13Cr-H	87.1	1782	144	13.184425	13.032385	0.15204

Table C.4 Liquid impact erosion data with brine (30 deg impact)

#	Material	Impact vel. (ft/s)	rpm	Time (hr)	Start weight (g)	End weight (g)	Loss (g)
14	1018	173.8	3510	16	18.995785	18.44623	0.549555
14	1018	173.8	3510	16	18.92052	18.451505	0.469015
14	1018	173.8	3510	16	18.92364	18.436435	0.487205
14	1018	173.8	3510	16	18.775125	18.303725	0.4714
15	316	173.8	3510	72	15.14194	15.141425	0.000515
15	13Cr-H	173.8	3510	72	13.28482	13.17635	0.10847
15	13Cr-A	173.8	3510	72	13.249035	13.228865	0.02017
15	9Cr-1M	173.8	3510	72	14.903955	14.177575	0.72638
16	Sm25-Cr	173.8	3510	72	17.752385	17.751825	0.00056
16	Sm825	173.8	3510	72	14.37954	14.376535	0.003005
16	625	173.8	3510	72	15.994115	15.990775	0.00334
16	2205	173.8	3510	72	17.93925	17.937895	0.001355